



## 저작자표시-비영리-변경금지 2.0 대한민국

이용자는 아래의 조건을 따르는 경우에 한하여 자유롭게

- 이 저작물을 복제, 배포, 전송, 전시, 공연 및 방송할 수 있습니다.

다음과 같은 조건을 따라야 합니다:



저작자표시. 귀하는 원저작자를 표시하여야 합니다.



비영리. 귀하는 이 저작물을 영리 목적으로 이용할 수 없습니다.



변경금지. 귀하는 이 저작물을 개작, 변형 또는 가공할 수 없습니다.

- 귀하는, 이 저작물의 재이용이나 배포의 경우, 이 저작물에 적용된 이용허락조건을 명확하게 나타내어야 합니다.
- 저작권자로부터 별도의 허가를 받으면 이러한 조건들은 적용되지 않습니다.

저작권법에 따른 이용자의 권리는 위의 내용에 의하여 영향을 받지 않습니다.

이것은 [이용허락규약\(Legal Code\)](#)을 이해하기 쉽게 요약한 것입니다.

[Disclaimer](#)

---

물리학박사 학위 논문

**GROWTH, VALLEYS MANIPULATION OF  $\text{MX}_2$  (M=MO; W, X=S;  
SE) AND THEIR HETEROSTRUCTURE**

울산대학교 대학원  
물리학과  
**FARMAN ULLAH**

---

# **GROWTH, VALLEYS MANIPULATION OF $\text{MX}_2$ (M=MO; W, X=S; SE) AND THEIR HETEROSTRUCTURE**

A thesis submitted in partial fulfillment of the requirement for the Degree of  
Doctor of Philosophy to the Department of Physics,  
University of Ulsan, Korea

By  
**FARMAN ULLAH**

**JUNE 2018**

---

**GROWTH, VALLEYS MANIPULATION OF  $\text{MX}_2$  (M=MO; W, X=S;  
SE) AND THEIR HETEROSTRUCTURE**

지도교수 **김용수**

이논문을 물리학박사 학위 논문으로 제출함

2018년 06 월

울산대학교 대학원

---

물리학과

**GROWTH, VALLEYS MANIPULATION OF  $\text{MX}_2$  (M=MO; W, X=S;  
SE) AND THEIR HETEROSTRUCTURE**

**This certifies that the dissertation of  
FARMAN ULLAH is approved by**

---

**Committee Chairman: Prof. YONG SOO KIM**

---

**Committee Member: Prof. JOON IK JANG**

---

**Committee Member: Prof. SUNG HYON RHIM**

---

**Committee Member: Prof. SUNG-LAE CHO**

---

**Committee Member: Prof. MAENG-JE SEONG**

---

**Department of Physics  
University of Ulsan, Korea**

**JUNE 2018**

---

---

## Contents

<b>List of abbreviations</b> .....	7
<b>List of Figures</b> .....	8
<b>Abstract</b> .....	13
<b>Chapter 1 Introduction to TMDCs (<math>\text{MX}_2</math>)</b> .....	16
1.1 Overview: .....	16
1.2 Crystal structure and composition: .....	17
1.3 Dimensionality dependence:.....	19
1.4 Excitons: Coulomb bound electron-hole pair in $\text{MX}_2$ .....	22
1.4.1 Neutral Exciton.....	22
1.4.2 Charge excitons .....	25
1.4.3 Valley excitons .....	25
1.5 Synthetic approaches for $\text{MX}_2$ .....	28
1.5.1 Chemical vapor deposition (CVD) growth:.....	29
1.5.2 Pulse laser deposition (PLD) assisted method:.....	29
1.6 $\text{MX}_2$ heterostructure (HS) system:.....	31
1.6.1 Vertical and lateral HS fabrication: .....	32
1.6.2 Valleys alignments in HS: .....	34
1.7 References .....	36
<b>Chapter 2 Continuous large area few layers <math>\text{MoS}_2</math> films by pulse laser deposition and effect of annealing in sulfur environment</b> .....	40
2.1 Introduction: .....	40
2.2 Motivation: .....	40
2.3 Experimental procedure:.....	41
2.3.1 $\text{MoS}_2$ film by pulse laser deposition.....	41
2.3.2 Annealing samples in sulfur environment: .....	42
2.3.3 Characterization of films: .....	42
2.4 Result and discussion: .....	43
2.5 Chapter summary.....	49
2.6 References .....	50
<b>Chapter 3 Pulse laser deposition assisted grown continuous monolayer <math>\text{MoSe}_2</math></b> .....	52
3.1 Introduction: .....	52
3.2 Motivation: .....	52
3.3 Experiment details: .....	53

---

3.3.1 MoO <sub>3</sub> target preparation: .....	53
3.3.2 MoO <sub>3</sub> film by pulse laser deposition: .....	54
3.3.3 Selenization of MoO <sub>3</sub> films .....	54
3.4 Result and discussion: .....	54
3.5 Chapter summary.....	65
3.6 References .....	66
<b>Chapter 4 Growth and Simultaneous Valleys Manipulation of Two-Dimensional MoSe<sub>2</sub>-WSe<sub>2</sub> Lateral Heterostructure .....</b>	<b>69</b>
4.1 Introduction: .....	69
4.2 Experimental details: .....	70
4.2.1 Synthesis.....	70
4.2.2 STEM Imaging and EDS analysis: .....	71
4.2.3 Experimental setup for polarization-sensitive PL measurements:.....	72
4.3 Result and discussion: .....	73
4.4 Chapter summary:.....	84
4.5 References .....	85
<b>Chapter 5 Initial results: Exciton Transport in monolayer WS<sub>2</sub> stripes .....</b>	<b>87</b>
5.1 Introduction: .....	87
5.2 Experimental details: .....	88
5.2.1 Monolayer WS <sub>2</sub> growth: .....	88
5.2.2 Characterization.....	89
5.3 Result and discussion.....	89
5.4 Chapter summary:.....	93
5.5 References .....	94
<b>Conclusion .....</b>	<b>95</b>
<b>Publications .....</b>	<b>97</b>

---

---

## List of abbreviations

2D . . . . .	Two-dimensional
3D . . . . .	Three-dimensional
AFM . . . . .	Atomic force microscope
CCD . . . . .	Charge-coupled device
CVD . . . . .	Chemical vapor deposition
DFT . . . . .	Density functional theory
DI . . . . .	Deionized
EDS . . . . .	Energy dispersive x-ray spectroscopy
FET . . . . .	Field-effect transistor
FWHM . . . . .	Full width at half maximum
MBE . . . . .	Molecular beam epitaxy
ME . . . . .	Mechanical exfoliation
OM . . . . .	Optical microscope
PL . . . . .	Photoluminescence
PLD . . . . .	Pulsed-laser deposition
PMMA . . . . .	Polymethyl methacrylate
SCCM . . . . .	Standard cubic centimeters per minute
SEM . . . . .	Scanning electron microscope
SAPRS . . . . .	Spatially and polarization resolved spectroscopy
TEM . . . . .	Transmission electron microscope
TMDC . . . . .	Transition metal dichalcogenide
UV . . . . .	Ultraviolet



---

## List of Figures

Figure 1- 1 Crystal structure of top and side view of monolayer (a) 2H-MX <sub>2</sub> and (b) 1T-MX <sub>2</sub> ...	18
Figure 1- 2 (a) Schematic illustration of band gap transition from indirect at bulk to direct at monolayer regime. (b) Optical microscope image of monolayer MoSe <sub>2</sub> with extra layers and (c) Photoluminescence spectra taken on the spots in (b).....	21
Figure 1- 3 Schematic illustration of Wannier-Mott excitons in 2D systems which have large radius encompassing many atoms and move freely in the crystal. A neutral exciton can attract another electron or hole to form a charged exciton.....	26
Figure 1- 4 Valley configuration of for the lowest energy neutral exciton in monolayer MoX <sub>2</sub> . The solid and empty dots represents electron and holes respectively. The red and blue line indicates spin up and down respectively. ....	28
Figure 1- 5 (a) Schematic diagram of a two zone hot wall furnace, (b) discontinuous monolayer MoS <sub>2</sub> film and (c) continuous monolayer MoS <sub>2</sub> film. ....	30
Figure 1- 6 Schematic illustration of (a) pulse laser deposition system and (b) two zone furnace	31
Figure 1- 7 (a) Procedure for MX <sub>2</sub> vertical HS by mechanical transfer method using (b) micromanipulator system (c) OM image of MoS <sub>2</sub> /WS <sub>2</sub> vertical HS.....	33
Figure 1- 8(a) Vertical HS of MoS <sub>2</sub> /WS <sub>2</sub> in real space and (b) the corresponding Brillouin zones in k-space. The energy valleys marked by K <sub>W</sub> for WS <sub>2</sub> and K <sub>M</sub> for MoS <sub>2</sub> coincides providing the twist angle is zero and give rise to interlayer exciton. ....	35
Figure 2- 1(a) Schematic illustration of two-step growth mechanism for few layer MoS <sub>2</sub> film i.e. MoS <sub>2</sub> deposited by PLD followed by annealing in sulfur environment. Surface morphology of deposited MoS <sub>2</sub> film at different laser energy, (b) 300, (c) 250 and (d) 200 mJ/cm <sup>2</sup> , respectively.....	44
Figure 2- 2 (a) Raman and (b) PL results of MoS <sub>2</sub> films deposited with PLD method at 200 mJ/cm <sup>2</sup> . ....	44
Figure 2- 3(a) FE-SEM and (b) 3D AFM image of the annealed MoS <sub>2</sub> sample in sulfur environment, which is deposited at laser energy density, 200 mJ/cm <sup>2</sup> . ....	45
Figure 2- 4(a) CCD images of annealed MoS <sub>2</sub> films on sapphire substrate at various deposition times, (b) Raman, (c) PL spectra's of annealed MoS <sub>2</sub> films deposited at 45 s, 75 s, 100 s,	

---

---

2.5 min and 10 min respectively, (d) PL intensity of A, B excitons and frequency difference $\Delta\omega$ ( $\text{cm}^{-1}$ ) of Raman spectra with respect to deposition time.....	46
Figure 2- 5 Absorbance and PL spectra of (a) as-deposited $\text{MoS}_2$ film which is approximately three layers, (b) annealed $\text{MoS}_2$ film at $850^\circ\text{C}$ in sulfur environment, (c) comparison of Raman spectra of annealed and as-deposited $\text{MoS}_2$ film.....	47
Figure 2- 6 Comparison of (a) Mo 3d and (b) S 2s XPS before and after annealing in sulfur. ....	48
Figure 3- 1(a) Schematic illustration of the growth mechanism of monolayer $\text{MoSe}_2$ , and the XPS results for the (b) Mo3d survey and(c) Se3d survey. ....	56
Figure 3- 2 OM images of $\text{MoSe}_2$ on the $\text{SiO}_2$ substrate corresponding to the $\text{MoO}_3$ film deposited at (a) 150mJ, (b) 115mJ, (c) 100mJ and (d) 90mJ, respectively. The scale bar is 15 $\mu\text{m}$ ...58	
Figure 3- 3 FE-SEM images of monolayer $\text{MoSe}_2$ (a) isolated flakes (b) boundary between flakes and continuous film (c) continuous film with some discontinuities at top left area (d) continuous film and (e-f) AFM image sand thickness profiles of continuous film and isolated flakes. The scale bar is 2 $\mu\text{m}$ . ....	59
Figure 3- 4 2D GIXD characterization of monolayer $\text{MoSe}_2$ including (a) 2D GIXD image and (b) cross-section profiles of 2D GIXD image at $q_z=0$ .....	60
Figure 3- 5 Raman and PL characterization of monolayer $\text{MoSe}_2$ (a) Raman spectrum (b) PL spectrum (c) OM image (d) Raman mapping with respect to $A_{1g}$ peak and (e) PL Intensity mapping of the highlighted region in (c). The scale bar is 10 $\mu\text{m}$ . ....	62
Figure 3- 6 (a) Optical microscope image of continuous monolayer $\text{MoSe}_2$ (c) Raman and (d) photoluminescence spectra taken at spot 1 to 10 with step size $\sim 10 \mu\text{m}$ . ....	63
Figure 3- 7 Azimuthal symmetry of PLD-assisted grown $\text{MoSe}_2$ analyzed by RA-SHG . The solid traces are fit curves corresponding to $\cos^2[3\theta + \theta_0]$ and $\sin^2[3\theta + \theta_0]$ , where $\theta$ denotes the angle between the incident linearly polarized electric field and the mirror axis of the crystal and $\theta_0$ denotes the initial angular offset. ....	64
Figure 3- 8 Monolayer $\text{MoSe}_2$ on sapphire substrate by PLD assisted method (a) flakes (b) continuous film (c) Raman and (d) photoluminescence spectra. The scale bar is 30 $\mu\text{m}$ .65	

---

Figure 4- 1 Schematic illustration of the experimental setup for polarization-resolved PL measurements .....	73
Figure 4- 2 Schematic representation of the experimental setup of the PLD-assisted growth mechanism for monolayer MoSe <sub>2</sub> -WSe <sub>2</sub> lateral HSs. (b) OM image of a lateral HS crystal on the SiO <sub>2</sub> substrate. The slightly dark inner triangle is MoSe <sub>2</sub> surrounded by WSe <sub>2</sub> . (c) FE-SEM image. (d) AFM topographic image taken over the HS flake in (b), showing a uniform thickness of 0.96 nm and confirming the monolayer nature of the lateral HS crystal. (e) AFM phase image taken over the black dashed square in (d), revealing the sharp and clean interface. The scale bar is 5 $\mu$ m. ....	75
Figure 4- 3 OM images of in-plane MoSe <sub>2</sub> -WSe <sub>2</sub> lateral and vertical heterostructures grown by the pulsed-laser-deposition-assisted method. (a) Isolated flakes, (b) continuous film-like lateral HSs, and (c-d) irregular vertical HSs locally formed over the lateral HS flakes. ....	76
Figure 4- 4 Raman scattering and PL characterization of the lateral HS crystal. (a) OM image of the lateral HS flake used for room-temperature Raman and PL scans. (b) Raman spectra taken at four points across the HS interface in (a) display A <sub>1g</sub> characteristics of MoSe <sub>2</sub> (~241.7 cm <sup>-1</sup> ) and WSe <sub>2</sub> (~251.8 cm <sup>-1</sup> ). (c) Room-temperature PL spectra acquired from the interface (point 2 and point 3 in (a) basically show the A-excitonic transitions of pristine MoSe <sub>2</sub> (1.51 eV) and WSe <sub>2</sub> (1.57 eV) without any complication arising from alloy states or interfacial effects. (d) PL intensity map. (e) PL position map. (f) Raman intensity map. (g) Raman shift map. The maps reveal the sharp interface of the lateral HS crystal. (h) OM image of the HS crystal used for low-temperature PL scan and (i) the corresponding low-temperature PL spectra taken at the five points at the triangular edge of the HS crystal in (h), showing the two PL peaks from each compound, which further supports the absence of alloys or intralayer excitonic matter. The scale bar is 10 $\mu$ m. ....	78
Figure 4- 5 Atomic resolution images of the WSe <sub>2</sub> -MoSe <sub>2</sub> lateral HS interface. (a) EDS spectra of WSe <sub>2</sub> and MoSe <sub>2</sub> regions. (b) Zoom-in HAADF-STEM image of WSe <sub>2</sub> with schematic modeling (yellow: Se, green: W) and (c) zoom-in HAADF-STEM image of MoSe <sub>2</sub> with schematic modeling (yellow: Se, pink: Mo). The scale bar is 0.5 nm. (d) Intensity line profiles of WSe <sub>2</sub> and MoSe <sub>2</sub> along the dashed red line in panel (b) and the dashed blue line	

---

in panel (c). (e) HAADF-STEM image near the WSe <sub>2</sub> -MoSe <sub>2</sub> interface. (f) STEM image with atomic overlay. The scale bar is 2 nm. ....	79
Figure 4- 6(a) OM image (inset) and PL scan of the lateral g-HS flake. The PL peak position gradually shifts from pristine MoSe <sub>2</sub> (point 1) to WSe <sub>2</sub> (point 6), indicating the extended alloy states across the interface. (b) PL intensity mapping taken over the red box in (a). The scale bar is 15 $\mu$ m. ....	80
Figure 4- 7 Crystal structures of the monolayer MoSe <sub>2</sub> -WSe <sub>2</sub> lateral HS formed at (a) armchair and (b) zigzag directions. Schematics of their Brillion zones in k space for (c) amrchair and (d) zigzag cases, respectively. Polarization-resolved PL spectra measured at 50 K for (e) $\sigma +$ and (f) $\sigma -$ excitation, respectively. (g) Degree of polarization ( $\chi$ ) as a function of emission energy calculated from the PL spectra in (e) and (f). ....	83
Figure 4- 8 Polarization-sensitive PL measurements on pristine MoSe <sub>2</sub> , WSe <sub>2</sub> and the interface MoSe <sub>2</sub> -WSe <sub>2</sub> regions of the lateral HS at room temperature, signifying no essential valley polarization. ....	84
Figure 5- 1(a) Schematic illustration of Valley Hall effect and (b) Exciton Hall effect. ....	90
Figure 5- 2(a) Optical microscope (b) AFM topography and (c) AFM phase image of monolayer WS <sub>2</sub> . (c) Raman and (d) PL spectra of WS <sub>2</sub> . ....	91
Figure 5- 3(a) Optical microscope image of WS <sub>2</sub> stripes with various widths (b) schematic illustration of K and K' excitons transport in monolayer WS <sub>2</sub> . K and K' excitons emits $\sigma +$ and $\sigma -$ photons respectively. Spatially and polarization resolved PL spectra acquired from stripe 3 for $\sigma +$ and $\sigma -$ excitation.....	93

---

---

## Acknowledgements

First, I would like to express my sincere gratitude to my supervisor Professor Yong Soo Kim. I feel honored to be a PhD student of such an inspirational professor. His zeal for research in physical science is contagious and truly motivational for young physicists. The way he encourages his students, particularly during their tough time, is phenomenal. I greatly appreciate all of his time, discussions and valuable ideas, which helped me a lot to improve my experimental skills and concepts. He helped me understand, consciously or unconsciously, the essence of experimental physics. Moreover, I appreciate the financial support he arranged for me during my entire PhD course. My pursuit of PhD would not have been possible without the scholarship.

The collaborators of our research group also contributed a lot to improve my professional skills. The group's members were like friends as well as tour guides alongside the scientific work. I would like to acknowledge Professor Mae Se Jong and his research students Mr. Yumin Shim and Mr. Jaeho Lee for their tremendous support in optical characterizations. I sincerely appreciate Professor Joon Ik Jang and Professor Sonny Rhim for their assistance in the theoretical framework of my research area. I am very much thankful to Professor Joon Ik Jang for his time and efforts regarding the reviewing of our articles and providing his valuable comments and suggestion. His comments significantly enhanced the quality of our articles and helped me a lot to improve my writing skills. I would also like to say special thanks to Professor Sonny Rhim for introducing and teaching me some of the very tricky and yet important concepts of advance Quantum mechanics.

My gratitude also goes to all of my lab members including Mr. Le Chinh Tam, Mrs. Nhu Thuy Ho, Mr. Anh Duc Nguyen, Mr. Jong Yun Won, Mr. Sung Han Lee, Mr. Sung Do Kim and Mr. Zeeshan Tahir. I feel lucky to work in such a friendly environment and sincerely hope that this attitude will be maintained in future. I am especially thankful to my Korean lab mates who were always there to assist me in official formalities. I would like to pay my gratitude to all the professors and clerical staffs of the department of physics, the University of Ulsan for friendly attitude and cooperation.

Finally, I would extend my gratitude to my beloved parents, brothers, wife and loving sons for their immense love and support throughout my study and entire life in general.

**FARMAN ULLAH**

---

## Abstract

The current electronic industry is mainly dominated by silicon, which is an intrinsically three-dimensional (3D) semiconducting material. The technology is improving rapidly and the silicon-based microprocessor is about to achieve its ultimate limit in the near future in terms of device performance and size. In this regard, search for alternative materials had been started from the last few decades and likely to remain in the foreseeable future. In 2004, the discovery of first truly two-dimensional (2D) material, namely graphene, was regarded as a major breakthrough and was considered to be an alternative material for the development of next generation electronic devices. However, the closed band gap of graphene is a serious issue and have not yet been addressed without compromising on its other excellent properties, particularly its electronic mobility. The graphene discovery, however, opened up a new window and many different 2D materials including insulator, metal, and semiconductors are discovered in this journey so far.

Among the 2D materials, the semiconducting monolayer transition metal dichalcogenides (TMDCs) possess huge potential for next generation electronic devices owing to their direct band gap and reasonable mobility. Moreover, their non-centrosymmetric nature, strong spin-orbit coupling (SOC) together with the time reversal symmetry render them an ideal setting for studying nonlinear optics and the fascinating valley physics. Furthermore, the artificial vertical stacking of various bandgap monolayer TMDCs forms type-II band alignment rendering them for PN-junctions and energy harvesting devices. However, in order to achieve high performance devices, the growth of high quality, large area and continuous film of different band gap monolayer TMDCs materials such as MoS<sub>2</sub>, WS<sub>2</sub>, MoSe<sub>2</sub> and WSe<sub>2</sub> is still a major concern.

The superior optical and electrical properties of mono and few layers MoS<sub>2</sub>, makes it a promising candidate for next generation flexible nanoelectronics and optoelectronics devices. However, controlled growth, scalability, uniform and continuous large area with a repeatable synthesis of mono and few layers MoS<sub>2</sub> are highly desirable. In chapter 2, a two-step synthetic approach has been adopted for the preparation of few layers MoS<sub>2</sub> films. MoS<sub>2</sub> films were prepared with different deposition times (45 s, 75 s, 100 s, 2.5 min and 10 min) at the same laser power, 200 mJ/cm<sup>2</sup> by pulse laser deposition (PLD) on a sapphire substrate. The samples were further annealed at 850 °C in a sulfur-rich environment. The optical properties of the annealed samples were moderately

---

improved. Significantly, the MoS<sub>2</sub> film deposited at 45 s exhibited a superior photoluminescence response with full width half maximum (FWHM) value of ~72.24 meV, as compared to the previous report of few layers MoS<sub>2</sub> by physical vapor deposition. Moreover, Raman frequency difference ( $\Delta\omega$ ) between A<sub>1g</sub> and E<sub>2g</sub><sup>1</sup> was found to be 23.6 cm<sup>-1</sup> indicating the film is approximately three layer.

Compared to sulfur compounds, the low reactivity of selenium makes it more challenging to synthesize good quality continuous single layered selenides required for practical applications. In chapter 3, we present the synthesis of monolayer MoSe<sub>2</sub> by selenization of pulsed laser deposited MoO<sub>3</sub> film on SiO<sub>2</sub>/Si and sapphire substrates. The laser energy was carefully varied to optimize the growth of highly uniform continuous monolayer film. The morphological characterizations including optical microscope, field emission scanning electron microscope and atomic force microscope results clearly demonstrate that the synthesized film is monolayer, continuous and homogeneous. The Raman and photoluminescence maps of the continuous film exhibit uniform brightness indicating the uniform and homogeneous nature of the film. Moreover, The full width half maximum values of A<sub>1g</sub> and A exciton peaks were found to be 3.7 cm<sup>-1</sup> and 24 nm, respectively, which show the excellent optical quality of the grown film. These results imply the potential use of grown film and the synthetic approach in device fabrication.

The covalently bonded in-plane heterostructure (HS) of monolayer transition metal dichalcogenides (TMDCs) possesses huge potential for high-speed electronic devices in terms of valleytronics. In chapter 4, high-quality monolayer MoSe<sub>2</sub>-WSe<sub>2</sub> lateral HSs are grown by the PLD-assisted selenization method. The sharp interface of the lateral HS is verified by morphological and optical characterizations. Intriguingly, photoluminescence spectra acquired from the interface show rather clear signatures of pristine MoSe<sub>2</sub> and WSe<sub>2</sub> with no intermediate energy peak related to intralayer excitonic matter or formation of Mo<sub>x</sub>W<sub>(1-x)</sub>Se<sub>2</sub> alloys, thereby confirming the sharp interface. Furthermore, the discrete nature of laterally attached TMDC monolayers, each with doubly degenerated but nonequivalent energy valleys marked by ( $K_M$ ,  $K'_M$ ) for MoSe<sub>2</sub>, and ( $K_W$ ,  $K'_W$ ) for WSe<sub>2</sub> in  $k$  space, allows simultaneous control of the four valleys within the excitation area without any crosstalk effect over the interface. As an example,  $K_M$  and  $K_W$  valleys or  $K'_M$  and  $K'_W$  valleys are simultaneously polarized by controlling the helicity of circularly polarized optical pumping, where the maximum degree of polarization is achieved at their respective band edges.

---

The current work provides the growth mechanism of laterally sharp HSs and highlights their potential use in valleytronics.

Furthermore, the non-centrosymmetric nature of monolayer  $\text{MX}_2$  together with time reversal symmetry gives rise to the non-zero Berry curvature  $\Omega(k)$  which serves as an effective internal magnetic field flux. The contrasting effect of  $\Omega(k)$  on  $K$  and  $K'$  valleys (energy extremum) dictates the charge carriers of respective valleys to move in opposite transverse direction in the presence of an external electric field. This fascinating phenomenon is called valley Hall effect. Recently, the Hall effect for neutral exciton ( $e$ - $h$  pair), namely exciton Hall effect (EHE), has also been observed in mechanically exfoliated monolayer  $\text{MoS}_2$  by locally inducing a chemical potential through laser illumination. Here, it is worth mentioning that unlike electric potential, a chemical potential drives both electrons and holes in the same direction, and is, therefore, essential for the realization of Hall effect of composite particles. In chapter 5, we briefly investigate the exciton transport in monolayer  $\text{WS}_2$  by using polarization and spatially resolved photoluminescence (PL) spectroscopy. In this regard, the stripes of various widths were prepared by laser trimming of  $\text{WS}_2$  grown via CVD. The excellent quality of  $\text{WS}_2$  was verified by optical and morphological characterizations. Interestingly, the excitons at  $K$  and  $K'$  valleys were found to move in the contrasting transverse direction due to the intrinsic Berry curvature showing the signal of EHE. Moreover, we observed that the diffusion length of valley excitons increases with the decreasing width of the stripe, implying that chemical potential could simply be altered by modifying the geometry of  $\text{MX}_2$ .



---

## Chapter 1 Introduction to TMDCs (MX<sub>2</sub>)

### 1.1 Overview:

The successful isolation of the single layer graphene from its bulk counterpart *via* mechanical cleavage (scotch tape) in 2004 by Geim group stimulated a wave of research in 2D systems [1]. Graphene is a single atom thick layer of carbon atoms connected through sp<sup>2</sup> bonding and packed in honeycomb lattice [2, 3]. Despite being a thinnest known material, graphene exhibits exceptional electronic, thermal and mechanical properties [4-7]. Besides some of the fascinating properties of graphene, it also has some major drawbacks including the dangling bonds and closed energy gap. These issues further motivated the research to explore other types of 2D systems [8]. In this journey, hundreds of 2D layered materials, each with its own unique properties have been discovered. The 2D family includes perfect insulator (hexagonal boron nitride (h-BN)), various energy gap semiconductors (phosphorene, MoS<sub>2</sub> etc) and conductors (graphene) [1, 9, 10]. The discoveries of these materials fulfill the essential requirements for the realization of a real 2D device. Interestingly, the 2D family also have PdTe<sub>2</sub>, which exhibits superconducting characteristics [11].

In a 2D family, transition metal dichalcogenides (TMDCs), whose generalized formula is MX<sub>2</sub> (where M: Mo; W and X: S; Se) exhibit semiconducting character. MX<sub>2</sub> materials have drawn tremendous attention in the recent few years incited by the discovery of their strong photoluminescence (PL) properties [12], and the demonstration of first monolayer MoS<sub>2</sub> based field effect transistor (FET) [13,14]. The MX<sub>2</sub> materials possess direct band gap in the visible spectrum with exceptionally high absorption properties [15]. Moreover, the band gap of these materials strongly depends on the number of layers (thickness) that undergoes a transition from indirect to direct when the material is thin down to single layer limit [16]. The direct energy gap renders monolayer TMDC materials for optoelectronics [13], and energy harvesting devices [17]. Structurally, monolayer MX<sub>2</sub> have no special inversion symmetry and therefore, provides a 2D platform for nonlinear optical study[18].

From the historical perspective, there were approximately 60 TMDCs materials known by late 1960 including at least 40 layered materials [19]. Their structure was initially determined in 1923 by Linus Pauling [20]. Moreover, the mechanical cleavage technique (scotch tapes) to acquire thin films was initially used for MoS<sub>2</sub> by the Robert Frindt in 1963 [21]. Surprisingly, the achievement

---

of first suspended monolayer MoS<sub>2</sub> date back to 1986 [22]. From the application standpoint, MoS<sub>2</sub> used to be applied as a solid lubricant in its bulk form in mechanical systems due to its layered structure [23].

## 1.2 Crystal structure and composition:

TMDCs predominantly form layered structure like graphite. However, some of the group VIII-X TMDCs could also form non-layered structures [24]. Among the layered materials, there are three common structural phases arising from the different coordination of metal and chalcogen atoms within the lattice. The phases are characterized in trigonal prismatic (2H), octahedral (1T), and rhombohedral (3R) coordination, respectively [25]. The 2H and 1T phases exist in monolayer, as shown in Fig. 1-1 (a) and (b), respectively. These phases can be understood in terms of the stacking order of the atomic planes forming an individual layer of the material. The order of the atomic planes can be represented in X-M-X coordination, such that, layer of metal (M) atoms is sandwiched between the two layers of chalcogen (X) atoms [26]. The metal and chalcogen within a layer (in a plane) are coupled by strong covalent bonding i.e. the M-X bond is covalent. On the other hand, two adjacent layers (out of plane) are coupled by weak van der Waals interactions [27]. The strong in plane coupling compared to the weak out of plane interactions naturally allows the isolation of single layer. The 2H phase has ABA stacking order such that the X atoms in both of its atomic planes (top and bottom) occupy exactly the same position A. Consequently, a single layer TMDC material in 2H phase maintains the mirror symmetry about the M plane within a layer. However, the 2H phase lacks the central inversion symmetry. The central inversion symmetry is restored in even number of layers. On the contrary, 1T phase follows ABC stacking order. The two X atoms in a layer occupy different positions A and C in its two atomic planes. The 1T possesses inversion symmetry with M being the inversion center. The 3R phase follows ABA stacking sequence. This phase does not exist in a single layer MX<sub>2</sub> film and is usually found in bulk MX<sub>2</sub> [26].

Thermodynamically, a 2H phase is the most stable phase while 1T can be considered a metastable state [28]. The different atomic arrangement within a layer significantly alters the electronic properties of the MX<sub>2</sub> systems. Pertinently, 1T phase exhibits metallic characteristics, while the 2H shows semiconducting behavior. Intriguingly, the transformation of the stable 2H phase into the metallic 1T phase can be achieved by intelligently applying external perturbations at the atomic

level. In this regard, Y.C.Lin *et al* used scanning transmission electron microscope (STEM) to perturb the lattice by bombarding electrons on a slight rhenium (Re) doped MoS<sub>2</sub> specimen [29]. The highly energetic electrons in the process transfer enough momentum to the top sulfur atoms. Consequently, the sulfur atoms start jiggling and transfer the momentum to the neighbor atoms. This process eventually results in the gliding of the top S plane and result in the phase transition from 2H to 1T phase. Most interestingly, the 1T phase can be controllably grown within monolayer 2H phase MoS<sub>2</sub> at the specific location. This means that the conducting properties can be spatially controlled within a single layer. In other words, a single layer can be made either metallic (1T) or semiconductor (2H) in selected areas without doping. The coexistence of both phases within a monolayer essentially paves the way to realize electronic devices like Schottky diode based on the truly single layer of MX<sub>2</sub> with involving metal contacts.

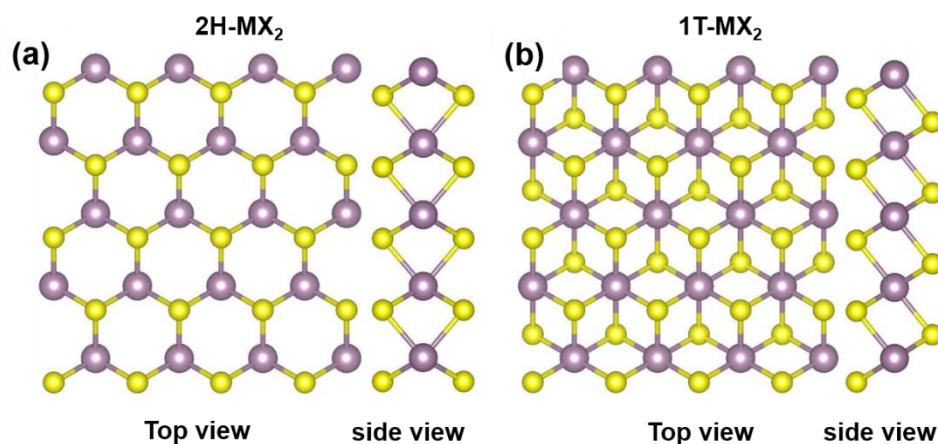


Figure 1- 1 Crystal structure of top and side view of monolayer (a) 2H-MX<sub>2</sub> and (b) 1T-MX<sub>2</sub>

Beside the positional changes of atoms within a layer to form different structural, the change in elemental composition is also an obvious consideration to alter the material properties. TMDCs have the diverse available elemental compositions each combination with its own unique properties [11]. The commonly known properties of various TMDCs based on their elemental composition are briefly summarized in Table 1. Chemically, in the X-M-X coordination, the M atom shares four electrons (+4 oxidation state) with the adjacent two X atoms (-2 oxidation state) forming covalent

---

bonds. The X atom lone-pair electrons terminate on the surface and consequently protecting the layer from reacting with the environmental species. Therefore, TMDCs materials do not make any dangling bonds making them environmentally stable. The absence of dangling gives an advantage to TMDCs materials over graphene, which usually has many dangling bonds.

**Table 1: Elemental composition based properties of different TMDCs**

Group	Metal	Chalcogen	Properties
4	Ti, Hf, Zr	S, Se, Te	Semiconductor with band gap $\sim 0.2-2$ eV
5	V, Nb, Ta	S, Se, Te	Semi metallic, superconducting, paramagnetic and antiferromagnetic.
6	Mo, W	S, Se, Te	MoS <sub>2</sub> , MoSe <sub>2</sub> , WS <sub>2</sub> , and WSe <sub>2</sub> are semiconductor while MoTe <sub>2</sub> and WTe <sub>2</sub> are semi metallic.
7	Tc, Re	S, Se, Te	Diamagnetic and low band gap semiconductor.
10	Pd, Pt	S, Se, Te	S and Se compounds are low band semiconductor while Te compounds are metallic. PdTe <sub>2</sub> show superconducting character.

### 1.3 Dimensionality dependence:

Recently, the studies on graphene and TMDCs materials clearly revealed that the dimensionality is also an important factor that plays a key role in defining the intrinsic properties of a material besides its crystal structure and chemical composition [30]. It is extremely fascinating in terms of both fundamental physics and device applications to see a material having the same structure and composition behave quite differently when its thickness is reduced. Pertinently, the electronic states of the MX<sub>2</sub> film are strongly dependent on the crystal thickness [16], that explains the transition from indirect energy gap at multilayer to the direct energy gap at monolayer limit [12]. The density function theory (DFT) calculations show that the conduction band minimum (CBM) exists in the middle of highly symmetric  $\Gamma$  and K points while the corresponding valence band minimum (VBM) remains at  $\Gamma$  point for multilayer MX<sub>2</sub>. The different positions of VBM and CBM form an indirect band gap at multilayers. However, the quantum confinement effect becomes apparent in monolayer

---

regime, and both the CBM and VBM shifts to the same  $K$  point of first Brillion, yielding a direct and slightly higher band gap compared to the bulk counterpart [31].

The evolution of  $\text{MX}_2$  band structure can further be understood in terms of orbitals contribution from the constituents, that it, M and X atoms in the unit cell [16]. The energy states that comprise both the valence and conduction band near  $K$  point in  $k$ -space are mainly associated with the hybridized d-electron orbits of M atoms. These orbitals are highly localized and insensitive to interlayer hopping due to the surrounding chalcogen atoms (X-M-X). On the other hand, the states near  $\Gamma$  point are mainly comprised of anti-bonding p-orbitals of chalcogen atoms. These states are strongly affected by interlayer coupling and hence on the crystal thickness. Therefore, with decreasing number of layers, the VBM gradually shifts toward the  $K$  point and eventually form direct band gap at monolayer regime. The transition in band structure is the function of thickness is schematically shown in the Fig.1-2(a). The direct band gap can be verified simply by monitoring the layer dependent PL properties of any semiconducting  $\text{MX}_2$  sample. Evidently, the PL intensity of  $\text{MoSe}_2$  exponentially decreases with the increasing thickness, as depicted in Fig 1-2 (b-c) . The quantum efficiency of a monolayer is few order of magnitude higher compared to the bulk [32].

Another hallmark of the reduced dimensionality of monolayer  $\text{MX}_2$  is their ultimate surface-to-volume ratio. The high surface-to-volume renders the monolayer extremely sensitive to the external perturbations. Consequently, any chemical or physical change on the surface significantly modifies their electronic properties. The high surface-to-volume make it a potential material for sensing application [33]. Moreover, the recent experimental studies have shown that the chemical functionalization of the surface with a desired functional group can effectively and yet selectively modify the optoelectronic properties[34]. The selective alteration of  $\text{MX}_2$  electronic properties by surface modifications is fascinating in terms of its potential use in biological sensing and catalysis [35].

---

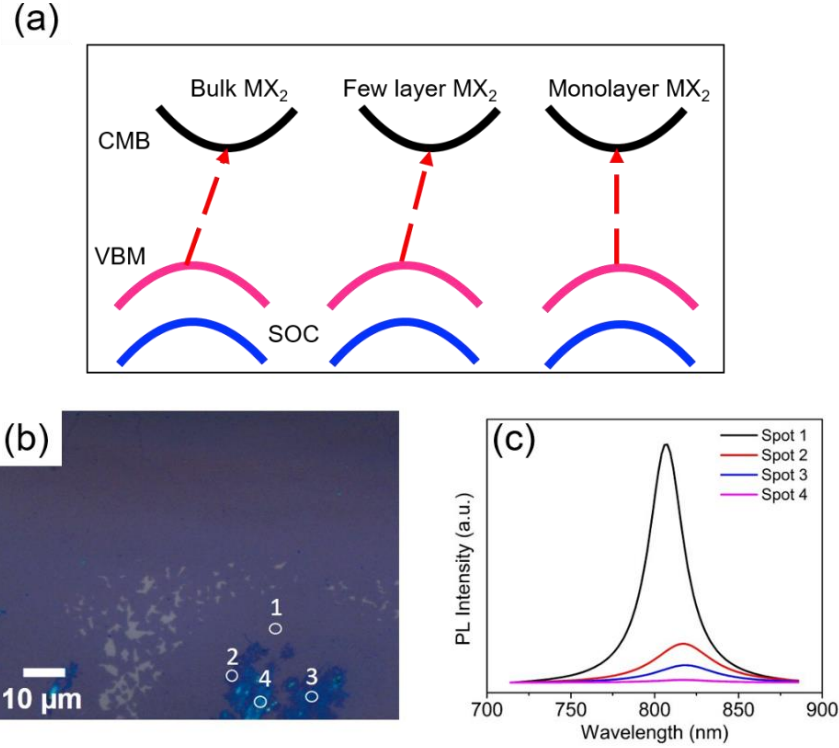


Figure 1- 2 (a) Schematic illustration of band gap transition from indirect at bulk to direct at monolayer regime. (b) Optical microscope image of monolayer MoSe<sub>2</sub> with extra layers and (c) Photoluminescence spectra taken on the spots in (b).

Additionally, when the MX<sub>2</sub> is thin down to single layer, the spin and valley (energy extremum) coupled together [36]. The coupling of spin and valley in monolayer MX<sub>2</sub> make them ideal systems for the study of intriguing valley physics. Generally, an energy valley can be described as a quantum number of an electron inside a crystal associated with its momentum [36]. Controlling valley degree of freedom allows information storage and processing in a similar fashion to electronics and spintronics exploit the charge and spin degree of freedom of electron, respectively. The monolayer MX<sub>2</sub> provides two degenerate but inequivalent K and K' valleys owing to its non-centrosymmetric nature, strong spin-orbit coupling (SOC) and time reversal symmetry. These valleys can be independently accessed simply by circularly polarized light i.e. the right ( $\sigma^+$ ) and left ( $\sigma^-$ ) hand circularly polarized light excites K and K' valleys respectively [37]. The valleys polarization has already been demonstrated by optical means, however, electrically control over these valleys would really open up the ways to realize a truly valleytronics devices. Further discussion on the exciton

---

valley configuration is provided in valley exciton section.

## **1.4 Excitons: Coulomb bound electron-hole pair in MX<sub>2</sub>**

### **1.4.1 Neutral Exciton**

Briefly, a promotion of an electron from a filled state in the valence band (VB) to an empty state in the conduction band (CB) either by optical or electrical means leaves an equivalent but opposite electronic charge behind in the corresponding VB. The charge remains in the form of an empty electronic state, treated as a particle and given the name so-called hole [38]. The two equivalent but opposite charged particles in their respective bands attract each other through Coulomb interaction and consequently, enhance the probability of forming a bound electron-hole pair (e-h) composite particle called exciton. The net charge of the exciton is zero; therefore, it also called neutral exciton. In a simplistic picture, an exciton can be conceived like hydrogen atom in which an electron revolves in a stable orbit around the hole

Moreover, a stable exciton is only form provided the Coulomb potential is sufficiently strong enough to withstand against all the odds of phonons collisions. The energy of a thermally excited phonon at temperature  $T$  is  $\sim K_B T$ , where  $K_B$  Boltzmann constant, therefore, the exciton binding energy must be higher than the Boltzmann energy (0.025 eV) [38]. The exciton forms in MX<sub>2</sub> are mainly Wannier-Mott excitons. These types of excitons usually have large radius encompassing many atoms and form in the semiconducting materials. Moreover, they are delocalized and mobile compared to the tightly bound Frankle excitons, as schematically shown in Fig. 1-3. The typical binding energies Wannier-Mott excitons forms in a usual 3D semiconductor are very small (few tens meV) compared to the binding energies of monolayer MX<sub>2</sub> systems (few hundreds meV). The origin of large exciton binding energies is briefly described below.

The exciton radii is much larger than the bond length and therefore, it can be considered a composite particle moving through a uniform dielectric material. The exciton can then be model by the Hydrogenic system to have a good estimate of binding energies and the radii. The bound states energies can be determined by finding the eigenvalues of the Schrodinger equation. The main results could also roughly be understood by applying the simplistic Bohr model. However, the dielectric constant  $\epsilon_r$  of the material and reduced mass ( $\mu$ ) must be integrated into the equation. The



---

energy  $E(n)$  of the  $n^{\text{th}}$  level and the corresponding radii is given by

$$E(n) = -\frac{\mu}{m_0 \epsilon_f^2} \frac{R_H}{n^2} = -\frac{R_X}{n^2} \text{--- -- (1)}$$

$$r_n = \frac{m_0}{m_r} \epsilon_r a_H = n^2 a_X \text{--- -- -- (2)}$$

Where  $n$  is the principal quantum number,  $R_H$  ( $R_X$ ) is Rydberg constant for hydrogen (exciton), while  $a_H$  ( $a_X$ ) is Bohr radius for hydrogen (exciton), respectively.  $m_0$  and  $m_r$  are the free electron mass and reduced mass of e-h respectively. The above equations show that the ground state ( $n=1$ ) has the maximum binding energy with minimum radii. Moreover, these equations are helpful to develop some basic understanding of exciton binding energies, however, the calculated values do not match well with the experimental values for excited states ( $n>1$ ). In addition, Bohr model does not hold for 2D systems. To develop a more robust understanding that could explain the origin of significantly large exciton binding energies of 2D TMDC systems, the dimensionality factor should be considered. The Wannier equation (Eq. (3)) on the other hand somehow addresses the dimensionality factor and provides a better understanding for 3D and 2D systems [39].

$$-\left[\frac{\hbar^2 \nabla_r^2}{2m_r} + V(r)\right] \psi(r) = E\psi(r) \text{--- -- -- (3)}$$

Here,  $\hbar$  is the reduced Plank constant,  $m_r$  is reduced mass,  $\nabla_r$  is Del operator,  $\psi(r)$  is wave function of exciton and  $E$  is the corresponding energy eigenvalue. Eq. (3) take exactly the same shape of two-particle Schrodinger equation for the relative motion of hole and electron interacting via coulomb potential  $V(r)$ . It is worth mentioning that the Wannier equation is derived under the assumption that  $V(r)$  is approximately constant over a unit cell. This assumption is valid only for large exciton Bohr radius. The calculated bound state energies from the above equation for 2D and 3D case are as follow:

$$\text{For 3D: } E(n) = -E_0 \frac{1}{n^2} \quad \text{with } n = 1, 2, \dots \text{--- -- (4)}$$

$$\text{For 2D: } E(n) = -E_0 \frac{1}{\left(n + \frac{1}{2}\right)^2} \quad \text{with } n = 0, 1, 2, \dots \text{--- (5)}$$

Where  $E_0$  is the exciton Rydberg energy. The ground state binding energy is  $E_0$  in 3D case and  $4E_0$  in 2D system respectively. The large binding energy for 2D systems can be understood in terms of a quantum well with decreasing the width of the well i.e. the energies increases with decreasing

---



width and vice versa. This somehow explains the extremely large exciton binding energies of monolayer TMDCs systems. The binding energies of the dominant A-exciton in the four widely studied TMDCs materials, including MoS<sub>2</sub>, MoSe<sub>2</sub>, WS<sub>2</sub>, and WSe<sub>2</sub> prepared by different methods are tabulated in Table 2 [40]. Each material has different binding energy and could be as large as 1/4 to 1/3 of their energy gap. Moreover, the findings also show that binding energies significantly varies with the substrate, temperature (T) and sample preparation method.

**Table 2:** Summary of binding energies of various TMDC on various substrate at a given temperature.

Specimen	Sample @ T (K)	Experimental technique	Binding energy (eV)	Bandgap (eV)	Reference
MoS <sub>2</sub>	CVD_HOPG @ 77K	PL	0.5	2.15	Zhang et al., 2014
		PLE	0.57	2.5	Klots et al., 2014
	Exf_hBN/FS @ 300K				
MoSe <sub>2</sub>	CVD_HOPG @ 79 K	PL	0.5	2.15	Zhang et al., 2014
WS <sub>2</sub>	Exf_SiO <sub>2</sub> /Si @ 5K	Reflectance	0.32	2.41	Chernikov et al., 2014
	Exf_FS @ 10K	2P-PLE	0.7	2.7	
	Exf_FS @ 300K	Reflectance	0.36	2.38	Ye et al., 2014
WSe <sub>2</sub>	Exf_SiO <sub>2</sub> /Si @ 300K	Reflectance	0.37	2.02	Rigosi et al., 2016
		PL	0.4	2.08	He et al., 2014
	CVD_HOPG @ 77 K				Chiu et al., 2015

\*\* CVD: chemical vapor deposition, FS: fused silica, HOPG: highly oriented pyrolytic graphite, PL: photoluminescence, PLE: photoluminescence excitation, Exf. Exfoliated and hBN: hexagonal boron nitride

---

### 1.4.2 Charge excitons

The attractive Coulomb interaction of a single electron with a hole results in an electrically neutral exciton. Additionally, other quasiparticles comprised of multiple electrons and holes are possible. In this regard, a quasiparticle, namely negative trion, is comprised of two electrons and one hole carry a net negative electronic charge. A positive trion consist of an electron and two holes, as schematically shown in Fig. 1-3. Moreover, unlike exciton a trion has a ground state spin ( $s=1/2$ ) and excited state spin ( $s=3/2$ ) originating from its constituents identical particles. The half spin characteristic of trion fundamentally distinguish it from excitons in many phenomena. Pertinently, the energy states of a trion splits in a strong magnetic field. Initially, trionic states were theoretically predicted followed by experimental verifications in different semiconductors including quantum dots and wells. Recently, independent groups have observed the trion states in various monolayer  $\text{MX}_2$  systems. Interestingly, the trion in the most studied  $\text{MX}_2$  material, monolayer  $\text{MoS}_2$ , have nearly one order of magnitude higher binding energy compared to the conventional 2D quasi-quantum wells. This phenomenon could be understood in terms of significantly enhanced coulomb interactions, reduced dielectric screening and relatively heavy masses associated with the transition metal d-orbitals in the gapped monolayer  $\text{MX}_2$ . The higher trion binding energies ( $\sim 20$  meV) in  $\text{MoS}_2$  are comparable the Boltzmann energy ( $\sim 25$  meV at 300K) making them accessible slightly below the room temperature. Furthermore, another member of TMDC family, namely  $\text{MoTe}_2$ , possesses binding energy of positive trion ( $X^+$ ) and negative trion( $X^-$ ) about  $\sim 24$  meV and  $\sim 27$  meV, respectively, rendering them even at room temperature. Most intriguingly, like excitons, which possesses spin and valley properties, the trions are also confine to the two specific valleys K ( $K'$ ) in semiconducting  $\text{MX}_2$ . The trions at the valleys can be optically access in a similar fashion like excitons by circularly polarized light. The dynamic control over the tightly bound trions opens up fascinating possibilities of studying the novel many-body phenomena.

---

### 1.4.3 Valley excitons

The recent intriguing aspect of excitons in monolayer  $\text{MX}_2$  systems is their valley configuration. The band structure essentially governs the energy vs crystal momentum relationship of a material. Generally, an energy extremum in either CB (minima) or VB (maxima) is known as an energy valley. Beside the fundamental charge and spin properties of an electron, it is also endowed with a

---

---

valley degree of freedom, which essentially specifies the energy valley that an electron occupies. Therefore, to understand the valley configuration of any material we need to understand its band structure.

---

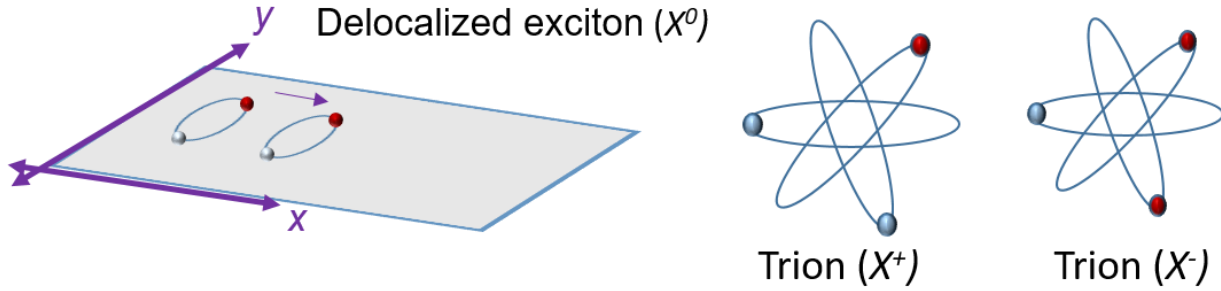


Figure 1- 3 Schematic illustration of Wannier-Mott excitons in 2D systems which have large radius encompassing many atoms and move freely in the crystal. A neutral exciton can attract another electron or hole to form a charged exciton.

---

The DFT calculations show that the band structure of monolayer  $\text{MX}_2$  possesses two degenerate but inequivalent energy valleys (extrema's) at K and K' points in the corner of hexagonal Brillion zone in k-space. Since both the VB and CB extremums are at the degenerate K and K' valleys, consequently, the lowest energy excitonic states are categorized by the spin as well as valley configuration. The K and K' are merely time reversal (motion reversal) of one another. Moreover, the CB and VB at K (K') are mainly comprised of  $d_{z^2}$  and  $d_{x^2-y^2} \pm id_{xy}$  orbitals having magnetic quantum number  $m=0$  and  $m=\pm 2$ , respectively [41]. Therefore, the VB edge at K (K') splits due to the strong SOC owing to the magnetic quantum number of  $d_{x^2-y^2} \pm id_{xy}$  orbitals. The VB splitting gives rise to the two so-called interband A- and B-excitonic transitions and can be easily monitored in the PL or absorption spectrum [12]. Moreover, the VB splitting in TMDC varies from  $\sim 150$  meV to  $\sim 500$  meV depending upon the elemental composition of  $\text{MX}_2$ . Surprisingly, the giant splitting of VBM in  $\text{MX}_2$  systems is essentially equal to the Zeeman splitting for electrons in magnetic field strength of  $10^2$  and  $10^3$  Tesla [16]. On the other hand, the dominant  $d_{z^2}$  component of CB do not contribute to the SOC and hence induce no splitting. However, other minor contributors such as  $d_{xy}$ ,

---

$d_{yz}$  of metal atom, and  $p_x$ ,  $p_y$  of chalcogen atom are responsible for the finite splitting of the CBM at K (K') valleys. The magnitude of splitting at CBM is much smaller than the splitting at VBM [41].

The time reversal symmetry together with broken inversion symmetry of monolayer  $MX_2$  dictates that the spin splitting must be in contrast at K and K' valleys. The spin and valleys are coupled together such that the holes in VB edge at K and K' valleys can only possess spin-up and spin-down states, respectively. The valley excitons can be understood in terms of the two fundamental physics principle namely momentum and spin conservation. The possible excitonic states are given as follows: (i). The recombination of electron and hole in different valleys is not allowed i.e. the hole in VB at K valley cannot be directly recombined with the electron in CB at K' valley because the conservation of momentum is not satisfied and therefore, this exciton is referred to as a dark exciton. (ii). The electron and hole at the same valley, either K or K' with opposite spin satisfy both spin and momentum conservation and therefore their direct recombination is allowed. The corresponding exciton is known as bright exciton. (iii) However, if both electron and hole constituents at the same valley possess same spin, their direct recombination is not allowed because conservation of spin is not satisfied. This valley configuration also give rise to dark state. (iv) Finally, if the constituents are in different valleys with same spin, their direct recombination is obviously not allowed owing to the fact that both momentum and spin conservation are not satisfied. The lowest energy excitonic states, namely A-excitons are depicted in Fig. 1-4. The optical interband transitions always have to conserve the spin and valley index; therefore, only bright exciton can emit a photon as indicated by its name itself. Experimentally, the bright exciton are observable in the PL, absorption and reflection spectrum of  $MX_2$  [Fig. ()]. The spectrum also show the so-called B-excitonic transition. The separation between A- and B-excitons show the VB splitting [41].

---

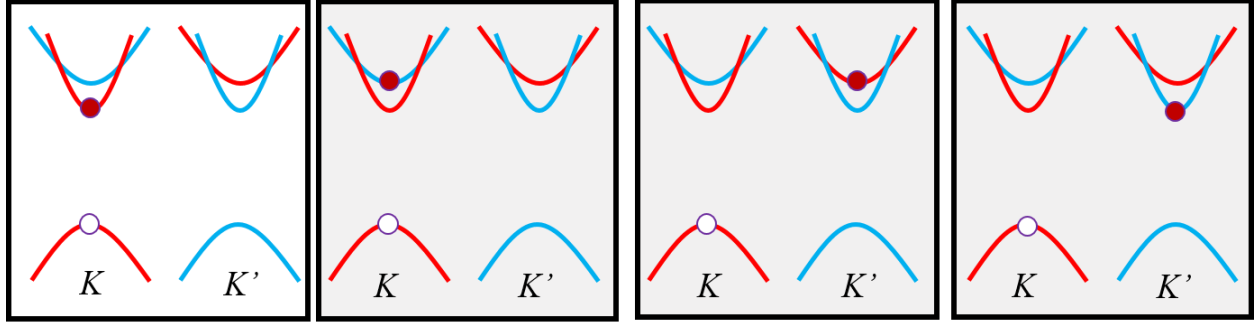


Figure 1- 4 Valley configuration of for the lowest energy neutral exciton in monolayer  $\text{MoX}_2$ . The solid and empty dots represents electron and holes respectively. The red and blue line indicates spin up and down respectively.

### 1.5 Synthetic approaches for $\text{MX}_2$

Most of the TMDC materials do not occur in nature in layered form except the commonly known  $\text{MoS}_2$  and  $\text{WS}_2$ . In this regard, various synthetic approaches have been employed to realize thin films comprised of mono and multilayers of different TMDC. These approaches are broadly classified into two top-down and bottom-up approaches. The top-down approach involves thinning down of bulk crystal by using various techniques, such as mechanical exfoliation [42], laser thinning [43], insertion of lithium (Li) with n-butyllithium by a chemical route [44], and liquid exfoliation by using ultra sonication [45]. These methods are general in a way that high quality flakes of various TMDC materials with a typical size of few tens of micron can be produced. However, their scope is limited to the fundamental research. The top-down approaches involving physical vapor deposition (PVD) techniques [46], such as, magnetron sputtering [47], atomic layer deposition (ALD) [48], molecular beam epitaxy (MBE)[49], and PLD can produce a thin film of a large area. However, it is extremely difficult to acquire monolayer film by using only PVD techniques. In addition, PVD films usually show poor crystallinity. Bottom-up approach involves mainly the reduction of metal precursors like molybdenum trioxide ( $\text{MoO}_3$ ) and thiomolybdate  $(\text{NH}_4)_2 \text{MoS}_4$  etc. in chalcogen environment. Potentially, this approach including chemical vapor deposition (CVD), metal organic chemical vapor deposition (MOCVD), and PLD assisted sulfurization/ salinization methods can produce a good quality film with scalable size possesses excellent electronic and optical properties required for device application. Herein, we adopted CVD and PLD assisted sulfurization/ salinization methods to produce monolayer and heterostructures of

---

different TMDCs on diverse substrates.

### **1.5.1 Chemical vapor deposition (CVD) growth:**

Probably, CVD method is the widely adopted for the growth of various TMDCs monolayers having comparatively large size and reasonable quality. The CVD method powder of metal oxide ( $\text{MO}_3$ ) and chalcogen (X) as typical precursors. Our CVD system is comprised of a two-zone furnace. The  $\text{MO}_3$  and X powder are placed in zone-1 (high temperature) and zone-2 (low temperature), respectively, as schematically shown in Fig. 1-5. The reaction chamber is initially flashed repeatedly with inert gasses to remove the environmental species. The tube furnace is then evacuated to the base pressure (few mtorr) by using a vacuum pump. Inert gasses like Ar and/or  $\text{N}_2$  are usually employed to the reaction chamber as carrier gasses and a working pressure is developed. The temperatures of each zone are simultaneously raised to the specified values (different for different materials). The carrier gases transport the X vapors generated at zone-2 to the zone-1 to make the reaction happen. The  $\text{MX}_2$  film is grown in zone-1 on the substrate placed upside down on the top of  $\text{MO}_3$  powder. A typical  $\text{MoS}_2$  sample grown by CVD on  $\text{SiO}_2/\text{Si}$  substrate is shown in Fig. 1-5 (b-c).

### **1.5.2 Pulse laser deposition (PLD) assisted method:**

Although PVD techniques essentially offer wafer scale continuous films of various materials, however, it is indeed daunting to realize crystalline films of materials having a layered structure, particularly monolayer TMDC by using solely PVD. An alternative approach, either bottom-up or top-down, could be the combination of both PVD and CVD techniques for the realization of crystalline mono or few-layer continuous films. Among PVD methods, PLD is one of the sophisticated method offering a precise control over the amount of depositing material simply by controlling the energy of laser shot and frequency (number of laser shots per unit time). In this regards, we developed PLD assisted method for the realization of good quality monolayer  $\text{MX}_2$  films. Interestingly, the approach can be further applied to synthesize vertical and laterally sharp HSs of  $\text{MX}_2$ . The working process of PLD assisted method is straight forward, as schematically shown in Fig. 1-6. Briefly, initially, a thin layer of precursor ( $\text{MO}_3$ ) is deposited on the substrate by PLD [Fig. 1-6 (a)]. The film is then placed in X (sulfur/selenium) rich environment at elevated temperature to grow  $\text{MX}_2$  films. It is worth mentioning that the amount of precursor is extremely

important and can significantly affect the film quality. We were able to produce excellent quality films by precisely controlling the amount of precursors. The film quality was even better than commercially available specimens. Moreover, this approach was found to be more effective for growing selenium monolayer compounds owing to its lower reactivity compared to sulfur. The sulfurization/selenization process is done in the two-zone hot wall furnace [Fig. 1-6(b)]. Inert gases like Ar and N<sub>2</sub> are used as carrier gasses to transport the chalcogen vapors. The details of growth procedure of various MX<sub>2</sub> and their HSs can be found in later chapters.

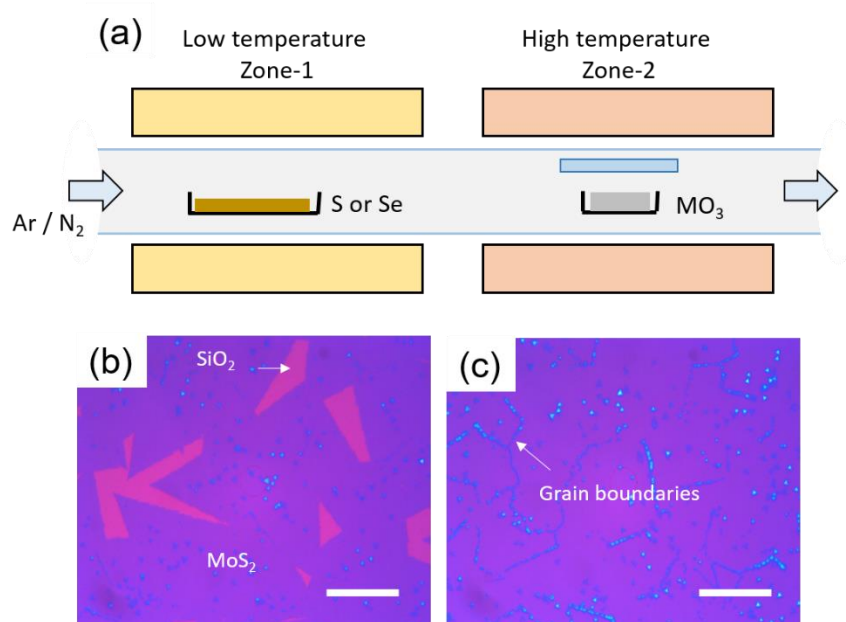


Figure 1- 5 (a) Schematic diagram of a two zone hot wall furnace, (b) discontinuous monolayer MoS<sub>2</sub> film and (c) continuous monolayer MoS<sub>2</sub> film.

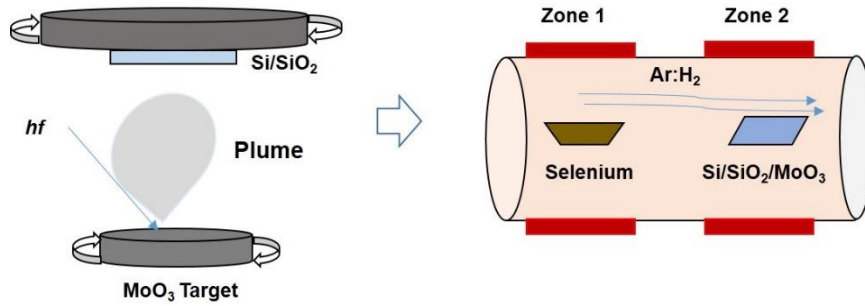


Figure 1- 6 Schematic illustration of (a) pulse laser deposition system and (b) two zone furnace

### 1.6 MX<sub>2</sub> heterostructure (HS) system:

The HSs systems among various energy gaps materials essentially provides a route to control over the flow of charge carriers by inducing energy barriers in its path. The interface between two different band gap materials inevitably create an energy barrier that serves as a gate at atomic level. The flow of charge carriers at the interface at a given input can somehow be controlled by simply varying the size of the barrier by joining materials of desired energy gaps. The precise control over carrier flow at the atomic level are turned into sophisticated electronic devices. However, it is very difficult to create a sharp junction. For 3D materials, excellent experimental skills and highly sophisticated and costly machinery are needed to make sharp HS owing to the complicated crystal structure. On the other hand, the van der Waal equivalents comprised 2D lattices can offers atomically sharp HS at pretty low owing to the absence of out of plane bonding[50]. The van der Waal HS of 2D lattices can be understood in terms of ligo building blocks with each color block representing a different material [51]. These different color blocks can just simply be transferred on each other to make HSs. Moreover, 2D materials also offers covalently bonded monolayer in plane (lateral) HSs. On contrary, in plane HS systems cannot be acquired by mechanical stacking and can only be achieved by direct growth methods. Recently, in plane HS systems among various 2D materials have been realized. These 2D HSs are shown to be a potential alternative for next generation flexible electronic devices [52]. Here we will discuss the methods which can be used for realizing the HS systems.



---

### 1.6.1 Vertical and lateral HS fabrication:

From the synthetic standpoint, HS systems could be created mainly by using two types of approaches, that is, mechanical transfer and direct growth methods. The mechanical transfer method is used to create vertical HS by artificially stacking of various 2D materials using a micromanipulator system. The procedure of manually creating vertical HS by is shown in Fig. 1-7 (a). This method is general and can be used to stack flakes of any arbitrary material irrespective of their structure and chemical composition. Moreover, this method has three degrees of freedom including translation ( $x$  and  $y$ -direction) and orientation (the angle between the two flakes). In other words, the position and orientation of the top flake can be manually controlled. The working procedure of this method is as follows: Initially, a thin layer of PMMA is coated on a Si/SiO<sub>2</sub> substrate having the flake of the desired material. The underlying oxide layer is then etched by slightly dipping in a diluted HF or NaOH. A thick transparent PDMS is then attached to it as a supporting layer. The flake is then stacked on the desired flake on a desired substrate. The PDMS layer is carefully removed and PMMA layer is dissolved in concentrated acetone [53].

The optical image of micromanipulator system and a MoS<sub>2</sub> flake stacked on WS<sub>2</sub> by the mechanical transfer method is depicted in Fig. 1-7 (b) and (c), respectively. Besides some of the obvious advantages of mechanical transfer, however, the flake quality usually degrades during the transfer mechanism owing to the involvement of acid in the process. Furthermore, the interface of the HS system created by the transfer method usually contains residues of the materials involved in the process. Alternatively, vertical HSs with the clean interface can be obtained by direct growth techniques. So far, mainly two types of approaches involving single step and two-step CVD growth have been established to realize vertical HS of different TMDCs materials including MoS<sub>2</sub>/WS<sub>2</sub>, MoSe<sub>2</sub>/WSe<sub>2</sub>, MoSe<sub>2</sub>/WS<sub>2</sub> and MoS<sub>2</sub>/WSe<sub>2</sub> [54-56]. Briefly, the precursors of the materials, such as MoO<sub>3</sub> and MoO<sub>3</sub> are placed in a single chamber along with S or Se in the single step growth method. Since the metal precursors evaporate at a different temperature, therefore, HS can be acquired by controlling the temperature profile. Both lateral and vertical HS can be randomly produced by this method. Some reports claim that the vertical and lateral can be selectively grown simply by controlling temperature, however, we could not verify this claim. Furthermore, the single step method can be used to acquire HS of different metal having the same chalcogen as MoS<sub>2</sub>/WS<sub>2</sub>

and  $\text{MoSe}_2/\text{WSe}_2$ . Moreover, the single step CVD grown HS usually have poor interface.

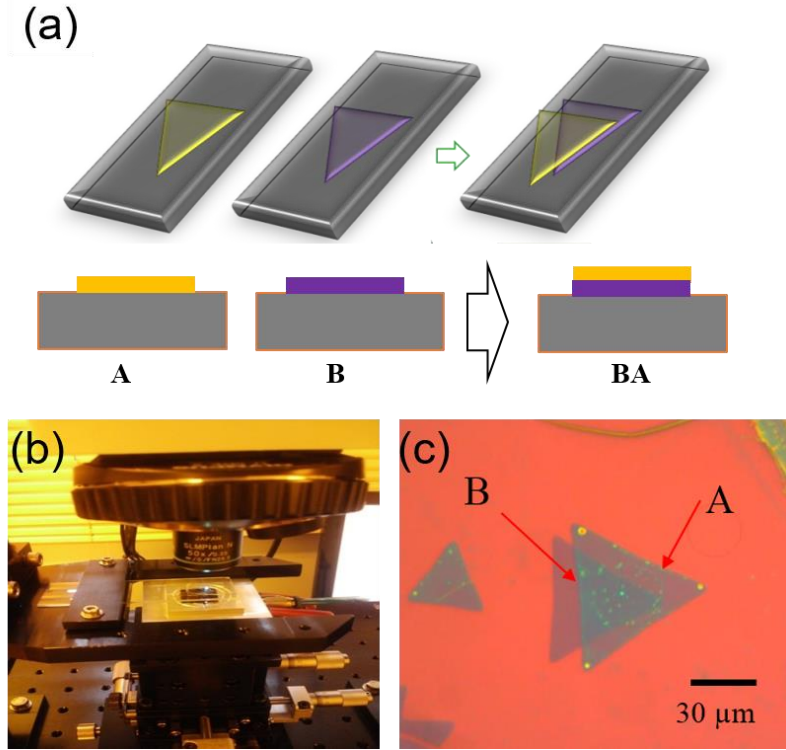


Figure 1- 7 (a) Procedure for  $\text{MX}_2$  vertical HS by mechanical transfer method using (b) micromanipulator system (c) OM image of  $\text{MoS}_2/\text{WS}_2$  vertical HS.

The HSs having different metal and different chalcogen, like  $\text{MoS}_2/\text{WSe}_2$  and  $\text{MoSe}_2/\text{WS}_2$ , can only be realized by using two-step growth mechanism [57]. Briefly, the two-step growth process involves the growth of one constituent in one CVD chamber followed by growth of another constituent in another chamber. For instance, to grow  $\text{MoS}_2\text{-WSe}_2$  (lateral) and/or  $\text{MoS}_2/\text{WSe}_2$  (vertical) HSs, initially  $\text{WO}_3$  precursor are used to grow monolayer flakes of  $\text{WSe}_2$  by conventional CVD method in Se rich hot wall tube furnace. The sample is then transferred to the S rich tube furnace in the presence of  $\text{MoO}_3$  to grow  $\text{MoSe}_2$  over the existing  $\text{WSe}_2$  flakes. This process can randomly produce atomically sharp lateral  $\text{MoS}_2\text{-WSe}_2$  HS or in some areas vertical  $\text{MoS}_2/\text{WSe}_2$  HS with a clean interface.

Moreover, we also the created HS systems by PLD assisted selenization/sulfurization method, which is a modified CVD method. Initially, we deposit the  $\text{MoO}_3$  and  $\text{WO}_3$  precursors at the edges

---

of the substrate while keeping the middle region void. The sample is then selenized/sulfurized in a selenium/sulfur-rich environment to obtain  $\text{MoSe}_2\text{-WSe}_2$  and  $\text{MoS}_2\text{-WS}_2$ , respectively. The selenization/sulfurization process is carried out in a two-zone furnace. The mechanism usually produces lateral HS with a reasonably sharp interface (See chapter 4).

### **1.6.2 Valleys alignments in HS:**

The artificially engineered van der Waals HS systems comprised of various monolayer 2D materials possess distinct properties useful for a variety of applications and fundamental studies [58-60]. Interestingly, the HS systems of different band gap  $\text{MX}_2$  materials, assembled with type-II band alignment [61], naturally accumulate the electron and holes in different layers, which render them for atomically thin PN-junctions [62, 63], and energy harvesting devices [64]. Moreover, the  $\text{MX}_2$  HSs are distinct from conventional quantum wells in many aspects and provides an alternative platform to study the emerging field of valleytronics. Some of the clear distinctions are as follows: the band structure of an HS system comprised of two different monolayer  $\text{MX}_2$  materials has two-degenerated energy valleys at the corner of the hexagonal Brillouin zone such that the interlayer excitonic transition, namely  $X_1$ , carries an internal degree of freedom specified by the valley indices. Second, the orientation (twist) angle between the constituent layers is extremely important. The energy valleys of both materials coincide ( $\Delta K=0$ ) in  $k$ -space for a perfectly aligned HS system ( $\Theta=0$ ) giving rise to a bright interlayer excitonic transition ( $X_1$ ). On the other hand, a large twist angle inevitably separates the energy valleys of the respective materials in  $k$ -space rendering the interlayer exciton dark owing to the large momentum difference. The energy valley alignments for  $\text{WS}_2$  and  $\text{MoS}_2$  forming a vertical HS (Fig. 1-8 (a)) are schematically shown in Fig. 1-8 (b). Third, similar to monolayer  $\text{MX}_2$ , their HS systems also exhibit valley contrasting physical properties such as optical selection rules, spin valley locking and Berry curvature. Consequently, the interlayer exciton can be optically accessed by controlling the helicity of the input light. Intriguingly, the lifetime (40 ns) of interlayer exciton was found to be much larger compared to the so-called A-exciton of individual material [65].

---

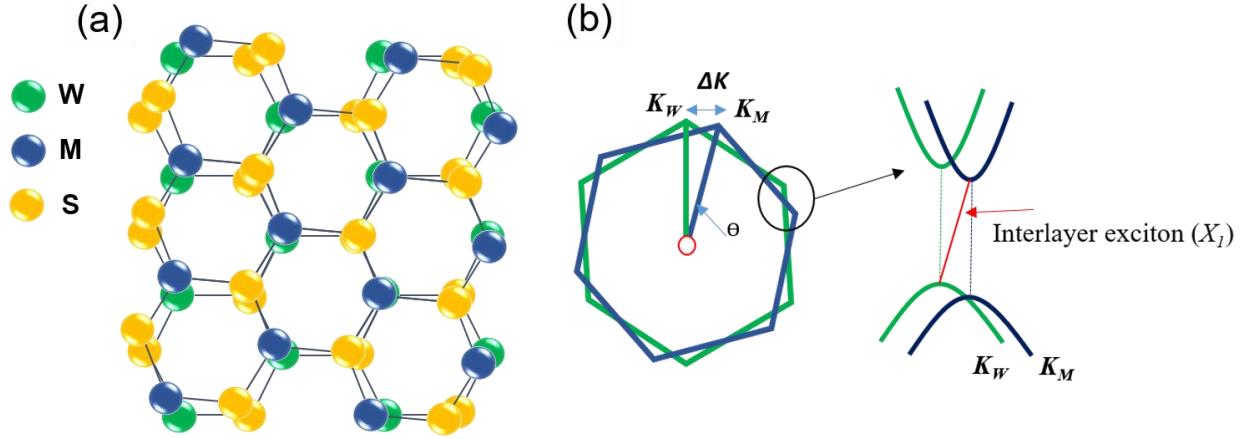


Figure 1- 8(a) Vertical HS of MoS<sub>2</sub>/WS<sub>2</sub> in real space and the corresponding (b) Brillouin zones in k-space. The energy valleys marked by K<sub>W</sub> for WS<sub>2</sub> and K<sub>M</sub> for MoS<sub>2</sub> coincides providing the twist angle is zero.

Compared to the van der Waal HS, in which any arbitrary 2D materials can be manually stacked at any arbitrary orientation with respect to one another, the covalently bonded lateral HS, however, can only be formed among specific materials. Recently, lateral HS of insulating hBN and semi metallic graphene and among different band gap MX<sub>2</sub> materials have been realized owing to their similar crystal structure and lattice parameters. On contrary, lateral HS of hBN or graphene with any material of TMDC family seems highly unlikely due to their distinct crystal structure. The lateral systems of monolayer TMDC are also of significant importance in terms of valleytronics. Unlike the vertical HS, in which the valleys of two constituents interacts over large area, the valleys of the constituents in an ideal lateral HS are well isolated in k-space except at the very interface. Interestingly, since each constituent possess two degenerate valleys, therefore, lateral HS system allows simultaneous manipulation the four energy valleys across the interface. The simultaneous valleys manipulation for MoSe<sub>2</sub>-WSe<sub>2</sub> lateral HS is discussed in detail in chapter 4.

---

## 1.7 References

- [1]. Novoselov, K. S.; Geim, A. K.; Morozov, S. V.; Jiang, D.; Zhang, Y.; Dubonos, S. V.; Grigorieva, I. V.; Firsov, A. A. *Science* **2004**, 306, 666-669.
- [2]. Meyer, J. C.; Geim, A. K.; Katsnelson, M. I.; Novoselov, K. S.; Booth, T. J.; Roth, S., *Nature* **2007**, 446, 60.
- [3]. Ma, J.; Alfè, D.; Michaelides, A.; Wang, E. *Physical Review B* **2009**, 80, 033407.
- [4]. Balandin, A. A., *Nature materials* **2011**, 10, 569.
- [5]. Novoselov, K.; Morozov, S.; Mohinddin, T.; Ponomarenko, L.; Elias, D.; Yang, R.; Barbolina, I.; Blake, P.; Booth, T.; Jiang, D. *physica status solidi (b)* **2007**, 244, 4106-4111.
- [6]. Pop, E.; Varshney, V.; Roy, A. K. *MRS bulletin* **2012**, 37, 1273-1281.
- [7]. Zhao, X.; Zhang, Q.; Chen, D.; Lu, P. *Macromolecules* **2010**, 43, 2357-2363.
- [8]. Koskinen, P.; Malola, S.; Häkkinen, H. *Physical review letters* **2008**, 101, 115502.
- [9]. Watanabe, K.; Taniguchi, T.; Kanda, H. *Nature materials* **2004**, 3, 404.
- [10]. Liu, H.; Du, Y.; Deng, Y.; Peide, D. Y. *Chemical Society Reviews* **2015**, 44, 2732-2743.
- [11]. Chhowalla, M.; Shin, H. S.; Eda, G.; Li, L.-J.; Loh, K. P.; Zhang, H. *Nature chemistry* **2013**, 5, 263.
- [12]. Splendiani, A.; Sun, L.; Zhang, Y.; Li, T.; Kim, J.; Chim, C.-Y.; Galli, G.; Wang, F. *Nano letters* **2010**, 10, 1271-1275.
- [13]. Yin, Z.; Li, H.; Li, H.; Jiang, L.; Shi, Y.; Sun, Y.; Lu, G.; Zhang, Q.; Chen, X.; Zhang, H. *ACS nano* **2011**, 6, 74-80.
- [14]. Radisavljevic, B.; Radenovic, A.; Brivio, J.; Giacometti, V.; Kis, A. *Nature Nanotechnology* **2011**, 147.
- [15]. Bernardi, M.; Palummo, M.; Grossman, J. C. *Nano letters* **2013**, 13, 3664-3670.
- [16]. Zeng, H.; Cui, X. *Chemical Society Reviews* **2015**, 44, 2629-2642.
- [17]. Tsai, M.-L.; Su, S.-H.; Chang, J.-K.; Tsai, D.-S.; Chen, C.-H.; Wu, C.-I.; Li, L.-J.; Chen, L.-J.; He, J.-H. *ACS nano* **2014**, 8, 8317-8322.
- [18]. Li, Y.; Rao, Y.; Mak, K. F.; You, Y.; Wang, S.; Dean, C. R.; Heinz, T. F. *Nano letters* **2013**, 13, 3329-3333.
- [19]. Wilson, J. A.; Yoffe, A. *Advances in Physics* **1969**, 18, 193-335.

- 
- [20]. Dickinson, R. G.; Pauling, L. *Journal of the American Chemical Society* **1923**, 45, 1466-1471.
- [21]. Frindt, R.; Yoffe, A. *Proc. R. Soc. Lond. A* **1963**, 273, 69-83.
- [22]. Joensen, P.; Frindt, R.; Morrison, S. R. *Materials research bulletin* **1986**, 21, 457-461.
- [23]. Roberts, E. *Tribology International* **1990**, 23, 95-104.
- [24]. Kwon, K. C.; Kim, C.; Le, Q. V.; Gim, S.; Jeon, J.-M.; Ham, J. Y.; Lee, J.-L.; Jang, H. W.; Kim, S. Y. *ACS Nano* **2015**, 9, 4146-4155.
- [25]. Butler, S. Z.; Hollen, S. M.; Cao, L.; Cui, Y.; Gupta, J. A.; Gutiérrez, H. R.; Heinz, T. F.; Hong, S. S.; Huang, J.; Ismach, A. F. *ACS Nano* **2013**, 7, 2898-2926.
- [26]. Manzeli, S.; Ovchinnikov, D.; Pasquier, D.; Yazyev, O. V.; Kis, A. *Nature Reviews Materials* **2017**, 2, 17033.
- [27]. Verble, J.; Wietling, T.; Reed, P. *Solid State Communications* **1972**, 11, 941-944.
- [28]. Ambrosi, A.; Sofer, Z.; Pumera, M. *Chemical Communications* **2015**, 51, 8450-8453.
- [29]. Lin, Y.-C.; Dumcenco, D. O.; Huang, Y.-S.; Suenaga, K. *Nature nanotechnology* **2014**, 9, 391.
- [30]. Li, T.; Galli, G. *The Journal of Physical Chemistry C* **2007**, 111, 16192-16196.
- [31]. Lebegue, S.; Eriksson, O. *Physical Review B* **2009**, 79, 115409.
- [32]. Salehzadeh, O.; Tran, N.; Liu, X.; Shih, I.; Mi, Z. *Nano letters* **2014**, 14, 4125-4130.
- [33]. Perkins, F. K.; Friedman, A. L.; Cobas, E.; Campbell, P.; Jernigan, G.; Jonker, B. T. *Nano letters* **2013**, 13, 668-673.
- [34]. Ataca, C.; Ciraci, S. *The Journal of Physical Chemistry C* **2011**, 115, 13303-13311.
- [35]. Lukowski, M. A.; Daniel, A. S.; Meng, F.; Forticaux, A.; Li, L.; Jin, S. *Journal of the American Chemical Society* **2013**, 135, 10274-10277.
- [36]. Xiao, D.; Liu, G.-B.; Feng, W.; Xu, X.; Yao, W. *Physical Review Letters* **2012**, 108, 196802.
- [37]. Zeng, H.; Dai, J.; Yao, W.; Xiao, D.; Cui, X. *Nature nanotechnology* **2012**, 7, 490.
- [38]. Fox, M., *Optical properties of solids*. Oxford university press: 2010; Vol. 3.
- [39]. Haug, H.; Koch, S. W.; Keldysh, L. V. *Physics Today* **1994**, 47, 106.
- [40]. Wang, G.; Chernikov, A.; Glazov, M. M.; Heinz, T. F.; Marie, X.; Amand, T.; Urbaszek, B. *arXiv preprint arXiv:1707.05863* **2017**.
-

- 
- [41]. Yu, H.; Cui, X.; Xu, X.; Yao, W. *National Science Review* **2015**, 2, 57-70.
- [42]. Li, H.; Wu, J.; Yin, Z.; Zhang, H. *Accounts of chemical research* **2014**, 47, 1067-1075.
- [43]. Castellanos-Gomez, A.; Barkelid, M.; Goossens, A.; Calado, V. E.; van der Zant, H. S.; Steele, G. A. *Nano letters* **2012**, 12, 3187-3192.
- [44]. Huang, G.; Chen, T.; Chen, W.; Wang, Z.; Chang, K.; Ma, L.; Huang, F.; Chen, D.; Lee, J. Y. *Small* **2013**, 9, 3693-3703.
- [45]. Nicolosi, V.; Chhowalla, M.; Kanatzidis, M. G.; Strano, M. S.; Coleman, J. N. *Science* **2013**, 340, 1226419.
- [46]. Muratore, C.; Hu, J.; Wang, B.; Haque, M. A.; Bultman, J. E.; Jespersen, M. L.; Shamberger, P.; McConney, M.; Naguy, R.; Voevodin, A. *Applied Physics Letters* **2014**, 104, 261604.
- [47]. Teer, D.; Hampshire, J.; Fox, V.; Bellido-Gonzalez, V. *Surface and Coatings Technology* **1997**, 94, 572-577.
- [48]. Tan, L. K.; Liu, B.; Teng, J. H.; Guo, S.; Low, H. Y.; Loh, K. P. *Nanoscale* **2014**, 6, 10584-10588.
- [49]. Ludwig, C.; Strohmaier, R.; Petersen, J.; Gompf, B.; Eisenmenger, W. *Journal of Vacuum Science & Technology B: Microelectronics and Nanometer Structures Processing, Measurement, and Phenomena* **1994**, 12, 1963-1966.
- [50]. Kang, J.; Li, J.; Li, S.-S.; Xia, J.-B.; Wang, L.-W. *Nano letters* **2013**, 13, (11), 5485-5490.
- [51]. Geim, A. K.; Grigorieva, I. V. *Nature* **2013**, 499, 419.
- [52]. Lee, G.-H.; Yu, Y.-J.; Cui, X.; Petrone, N.; Lee, C.-H.; Choi, M. S.; Lee, D.-Y.; Lee, C.; Yoo, W. J.; Watanabe, K. *ACS nano* **2013**, 7, 7931-7936.
- [53]. Salvatore, G. A.; Münzenrieder, N.; Barraud, C.; Petti, L.; Zysset, C.; Büthe, L.; Ensslin, K.; Tröster, G. *ACS nano* **2013**, 7, 8809-8815.
- [54]. Yu, Y.; Hu, S.; Su, L.; Huang, L.; Liu, Y.; Jin, Z.; Purezky, A. A.; Geohegan, D. B.; Kim, K. W.; Zhang, Y. *Nano letters* **2014**, 15, 486-491.
- [55]. Tongay, S.; Fan, W.; Kang, J.; Park, J.; Koldemir, U.; Suh, J.; Narang, D. S.; Liu, K.; Ji, J.; Li, J. *Nano letters* **2014**, 14, 3185-3190.
- [56]. Xue, Y.; Zhang, Y.; Liu, Y.; Liu, H.; Song, J.; Sophia, J.; Liu, J.; Xu, Z.; Xu, Q.; Wang, Z. *Acs Nano* **2015**, 10, 573-580.
-

- 
- [57]. Li, M.-Y.; Shi, Y.; Cheng, C.-C.; Lu, L.-S.; Lin, Y.-C.; Tang, H.-L.; Tsai, M.-L.; Chu, C.-W.; Wei, K.-H.; He, J.-H. *Science* **2015**, 349, 524-528.
- [58]. Lim, H.; Yoon, S. I.; Kim, G.; Jang, A.-R.; Shin, H. S. *Chemistry of Materials* **2014**, 26, 4891-4903.
- [59]. Yu, J. H.; Lee, H. R.; Hong, S. S.; Kong, D.; Lee, H.-W.; Wang, H.; Xiong, F.; Wang, S.; Cui, Y. *Nano letters* **2015**, 15, 1031-1035.
- [60]. Cho, S.-Y.; Kim, S. J.; Lee, Y.; Kim, J.-S.; Jung, W.-B.; Yoo, H.-W.; Kim, J.; Jung, H.-T. *ACS nano* **2015**, 9, 9314-9321.
- [61]. Ceballos, F.; Bellus, M. Z.; Chiu, H.-Y.; Zhao, H. *ACS nano* **2014**, 8, 12717-12724.
- [62]. Ross, J. S.; Rivera, P.; Schaibley, J.; Lee-Wong, E.; Yu, H.; Taniguchi, T.; Watanabe, K.; Yan, J.; Mandrus, D.; Cobden, D. *Nano letters* **2017**, 17, 638-643.
- [63]. Roy, T.; Tosun, M.; Cao, X.; Fang, H.; Lien, D.-H.; Zhao, P.; Chen, Y.-Z.; Chueh, Y.-L.; Guo, J.; Javey, A. *Acs Nano* **2015**, 9, 2071-2079.
- [64]. Nourbakhsh, A.; Zubair, A.; Dresselhaus, M. S.; Palacios, T. s. *Nano letters* **2016**, 16, 1359-1366.
- [65]. Rivera, P.; Seyler, K. L.; Yu, H.; Schaibley, J. R.; Yan, J.; Mandrus, D. G.; Yao, W.; Xu, X. *Science* **2016**, 351, 688-691.



---

## Chapter 2 Continuous Large Area Few Layers MoS<sub>2</sub> Films by Pulse Laser Deposition and Effect of Annealing in Sulfur Environment

### 2.1 Introduction:

The electronics properties of TMDCs vary from semiconducting to metallic, depending upon the crystal structure and chemical composition. For instance, 2H-MoS<sub>2</sub>, WS<sub>2</sub>, MoSe<sub>2</sub>, WSe<sub>2</sub> and MoTe<sub>2</sub> are semiconductors, while 1T-MoS<sub>2</sub>, NbS<sub>2</sub>, NbSe<sub>2</sub> and NbTe<sub>2</sub> shows metallic behavior [1, 2]. The semiconducting TMDCs materials possesses diverse band gaps ranging from ~1 eV to ~2.1 eV, suitable for optoelectronics and energy harvesting devices. In TMDCs family, MoS<sub>2</sub> is one of the widely studied material. MoS<sub>2</sub> has hexagonal structure like graphene and h-BN, in which one Mo atom is sandwiched between two S atoms. The optical band gap of MoS<sub>2</sub> lies in the visible spectrum (1.2 eV for bulk and ~1.85 for monolayer) [3, 4]. In this chapter, we will mainly discuss the growth mechanisms used for mono and multilayers MoS<sub>2</sub>.

### 2.2 Motivation:

MoS<sub>2</sub> has wide range of applications in diverse fields, such as, catalysis [5], chemical sensor [6-8], memory devices [9, 10], solar cell [11], electronics [12] and optoelectronics [13, 14]. A top gate field effect transistor (FET) based on mechanically exfoliated single layer MoS<sub>2</sub> with hafnium oxide (HfO<sub>2</sub>) as gate dielectric has shown excellent mobility (200 cm<sup>2</sup>/V·s) and exceptionally high ON/OFF ratio, ~10<sup>8</sup> [15]. Furthermore, MoS<sub>2</sub> based photodetectors have exhibited higher photo responsivity compared to graphene [16, 17].

So far, a great deal of attention has been paid to explore and utilize the properties of single layer MoS<sub>2</sub>. However, controlled synthesis of large area single layer MoS<sub>2</sub>, difficulties in device fabrication process, and the novel properties of multilayers MoS<sub>2</sub> suggest that, multilayers MoS<sub>2</sub> could also be attractive for some applications as compared to the single layer counterpart. FET based on multilayer MoS<sub>2</sub> film has shown high mobility (> 100 cm<sup>2</sup>/V·s) and nearly ideal subthreshold swing (~70 mV/decade) [18]. Moreover, multilayer MoS<sub>2</sub> has three times higher density of states (DOS) than single layer MoS<sub>2</sub>, and the capacity to draw a higher current compared to monolayer within the ballistic limit [19].

Moreover, the above studies have been carried out on either micromechanically exfoliated or CVD

---

grown MoS<sub>2</sub> micro flakes. Although some reports are available on continuous large area film by CVD but generally both methods produce highly crystalline few micrometer size flakes, which cannot be used beyond basic research study [20]. Different synthetic approaches are used to produce large area good quality MoS<sub>2</sub> films. Recently, Y. C. Lin et al., reported the synthesis of polycrystalline multilayer MoS<sub>2</sub> films by the reduction of pre-deposited molybdenum trioxide (MoO<sub>3</sub>) to MoS<sub>2</sub> by sulfurization [21]. Similarly, few nanometer thin film of molybdenum (Mo), deposited by e-beam evaporator were converted to MoS<sub>2</sub> film by annealing in the presence of hydrogen sulfide (H<sub>2</sub>S) [22]. The synthesis of MoS<sub>2</sub> from other precursor like thiomolybdate ((NH<sub>4</sub>)<sub>2</sub>MoS<sub>4</sub>) has also been demonstrated [23].

In this work, we demonstrate synthesis of large area continuous few layers MoS<sub>2</sub> film by two-step process. In the first step, we use PLD system to deposit MoS<sub>2</sub> film on sapphire substrate. PLD is a PVD technique suitable for good quality thin film deposition. PVD technique could produce large area continuous film required for practical applications. Recently, magnetron sputtering has been demonstrated for the synthesis of multi layers (~5 nm MoS<sub>2</sub> film). The obtained film by magnetron sputtering is continuous over 4 cm<sup>2</sup> area, however, the grown film shows broad PL spectrum with negligible intensity indicating the amorphous nature [24]. We observed similar behavior in our PLD deposited MoS<sub>2</sub> film. To improve the crystal structure, we anneal the deposited samples in the presence of sulfur. Spectroscopic results show that the film quality is greatly improved by annealing process.

### **2.3 Experimental procedure:**

The experimental details of each step involving in PLD assisted growth process is given below.

#### **2.3.1 MoS<sub>2</sub> film by pulse laser deposition**

The MoS<sub>2</sub> target material placed in the vacuum chamber is initially exposed to high power laser beam, as schematically shown in Fig. 1-6 (a) in chapter 1. The laser beam provides enough energy to the target material and the target species are taken out from the hitting spot of the target. These species are then condensate on the substrate to form the film. The growth procedure of MoS<sub>2</sub> film by PLD method is as follows: highly pure MoS<sub>2</sub> target of approximately 2 cm diameter was placed in rotating target holder. The target was exposed to laser beam for few minutes to remove the

---

contaminants aggregated on the surface. Approximately  $2 \times 2 \text{ cm}^2$  sapphire substrate was placed in a rotating substrate holder. The distance between substrate and target was set to 25 cm. The chamber pressure was set to 25 mTorr with 10 sccm of highly pure argon gas (Ar). A krypton fluoride (KrF) excimer laser ( $\lambda=248 \text{ nm}$ , CompexPro 102F) with 20 ns pulse width was used. MoS<sub>2</sub> thin films were deposited at various laser powers with repetition rate of 3Hz (# of laser shots on the target per second). The substrate temperature was maintained at 700°C.

### **2.3.2 Annealing samples in sulfur environment:**

To improve the crystalline structure, the grown MoS<sub>2</sub> films were annealed in two zones hot-wall CVD system with sulfur-rich environment. The schematic diagram of CVD system is shown in chapter 1 in Fig. 1-6 (b). Approximately 0.30 gram of pure sulfur powder (99.99 %, Alfa) was placed in graphite crucible. The PLD deposited MoS<sub>2</sub> samples were kept on silicon wafer and were placed 15 cm away from the sulfur powder in the quartz tube. The tube pressure was reduced to the base value of 60 mTorr. Initially, pure N<sub>2</sub> gas was flashed into the quartz tube repeatedly to clean the contaminants. The temperatures of zone-I and zone-II were set to 325 °C and 850 °C respectively. The tube pressure was maintained to 500 Torr during the annealing process. The samples were annealed for 30 minutes.

### **2.3.3 Characterization of films:**

Morphological, optical and electrical characterization were carried out to examine the grown and annealed MoS<sub>2</sub> films. The surface morphology of the films was checked by atomic force microscopy (AFM; tapping mode with cantilever of  $k \sim 1.8 \text{ N/m}$ , 0.5 Hz scan speed) and field emission second electron microscopy (FE-SEM; JEOL, JSM 6500F). PL and Raman spectra's were taken at room temperature using argon Ar+ laser (Melles Griot, 35-LAP-431-220) with 514.5 nm excitation light source. The spot size of laser was about  $\sim 10 \text{ }\mu\text{m}$ . A single grating spectrometer (Princeton Instruments, SP-2500i) with a focal length of  $\sim 50 \text{ cm}$  was used to analyze the scattered light from the sample and was detected with a cooled liquid nitrogen CCD detector (Princeton Instruments, Spec-10). The recorded wavelength and Raman shift of the scattered light were calibrated by using the standard Neon calibration lamp (Newport, 6032). The absorbance spectra were measured by UV-Vis-NIR spectrometer (Carry 5000, Varian) at room temperature. The chemical composition analysis was done by X-ray photoelectron spectroscopy (XPS; Theta Probe

---

AR-XPS System, ThermoFisher Scientific). During the analysis, the need for sample charging was done away by calibrating the energy spectra against C 1s peak. Hall mobility was measured at room temperature using HMS-5000 Hall effect measurement system.

## 2.4 Result and discussion:

The two-step growth mechanism for MoS<sub>2</sub> synthesis as depicted in Fig. 2-1(a). Firstly, the uniform MoS<sub>2</sub> films were optimized on a sapphire substrate by PLD system. Fig. 2-1(b-d) shows the FE-SEM images of deposited films with different laser powers of 300, 250 and 200 mJ/cm<sup>2</sup>, respectively. The MoS<sub>2</sub> film deposited at the laser power of 200 mJ/cm<sup>2</sup> shows smooth and uniform surface morphology, whereas higher laser powers leads to the formation of dense nanoparticles like structures. However, there was no film formation below the laser power of 200 mJ/cm<sup>2</sup>. It is clearly evident that the laser power plays a crucial role in the formation of the uniform MoS<sub>2</sub> film. Hence, the optimized uniform MoS<sub>2</sub> film deposited at a laser power of 200 mJ/cm<sup>2</sup> was used for the further characterizations. Fig. 2-2 (a) and (b) shows the Raman and PL results of the MoS<sub>2</sub> deposited film at a laser power of 200 mJ/cm<sup>2</sup>. There were no well-resolved peaks in both results, which confirmed the prepared film was in poor crystalline or amorphous in nature. In order to improve the crystalline structure and optical properties of MoS<sub>2</sub> film, the annealing process was executed in sulfur rich environmental condition by CVD system. Fig. 2-3 (a) and (b) shows the FE-SEM and AFM images of the annealed MoS<sub>2</sub> sample respectively. From both results, it can be clearly seen that no individual islands, particles or flakes were formed on the surface. This observation indicates that the prepared film is in layered structure. In addition, the surface roughness (RMS; root mean square) of the film was found to be ~0.9 nm. Further, to investigate the layer control in detail, we had deposited the MoS<sub>2</sub> films with different deposition times such as 45 s, 75 s, 100 s, 2.5 min and 10 min with the same laser of 200 mJ/cm<sup>2</sup>, and followed by the annealing process. The images of the samples are shown in Fig. 2-4(a). These samples were further investigated by Raman and PL measurements. Raman scattering is an indirect way to estimate the number of layers of two dimensional (2D) layered materials. It is an experimentally observed fact that the position of two prominent Raman active modes i.e. A<sub>1g</sub> (out of plane) and E<sup>1</sup><sub>2g</sub> (in plane) of MoS<sub>2</sub> is the function of the film thickness. This striking characteristic, i.e. the frequency difference between the two vibrational modes can be exploited to estimate the film thickness [25]. The A<sub>1g</sub> vibrational mode

shifts towards shorter wavelengths (blue shift) while  $E_{2g}^1$  shifts towards longer wavelengths (red shift) with increasing number of layers and vice versa [26,27]. Similar trend can be observed in the Raman spectra's of our samples. The frequency difference increases with increasing thickness as shown in Fig. 2-4(b).

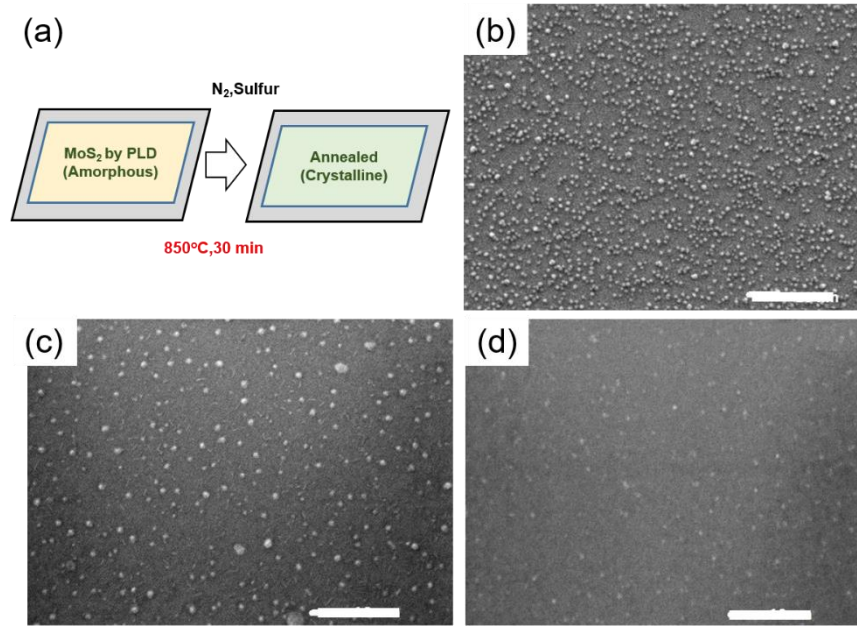


Figure 2- 1(a) Schematic illustration of two-step growth mechanism for few layer MoS<sub>2</sub> film i.e. MoS<sub>2</sub> deposited by PLD followed by annealing in sulfur environment. Surface morphology of deposited MoS<sub>2</sub> film at different laser energy, (b) 300, (c) 250 and (d) 200 mJ/cm<sup>2</sup>, respectively.

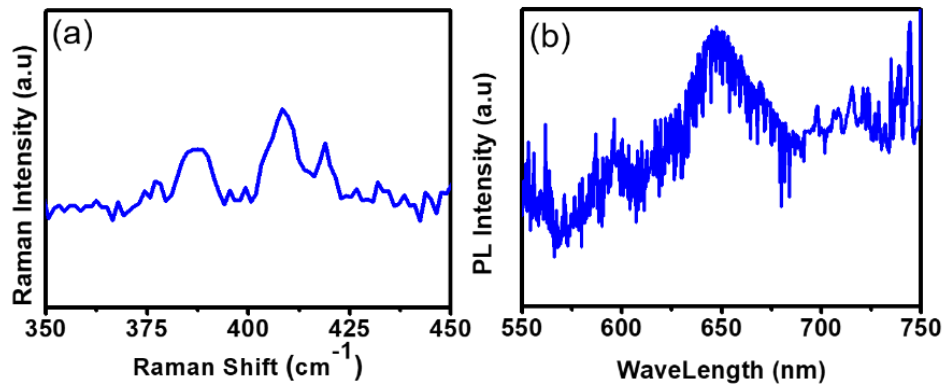


Figure 2- 2 (a) Raman and (b) PL results of MoS<sub>2</sub> films deposited with PLD method at 200 mJ/cm<sup>2</sup>.

---

The two prominent vibrational modes ( $A_{1g}$  and  $E_{2g}^1$ ) can be found in all sample while the other two vibrational modes  $E_{1g}$  and  $E_{2g}^2$  of  $MoS_2$  cannot be detected. The reason of the two undetected modes might be the rejection of limited Rayleigh scattered radiation [28]. The peak positions of  $A_{1g}$  and  $E_{2g}^1$  for 45 s deposited sample was found to be at  $409.15\text{ cm}^{-1}$  and  $385.55\text{ cm}^{-1}$  respectively. Based on previous reports, this frequency difference ( $\Delta\omega$ ),  $23.6\text{ cm}^{-1}$  corresponds to approximately three layers of  $MoS_2$  [25, 26]. The full width half maximum (FWHM) value of  $E_{2g}^1$  peak is  $\sim 5.3\text{ cm}^{-1}$ , which is slightly higher than CVD grown  $MoS_2$  [29,30].

---

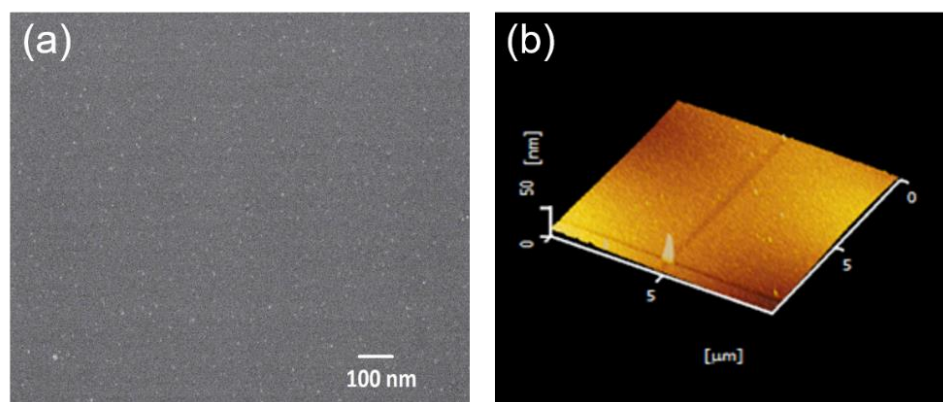


Figure 2- 3(a) FE-SEM and (b) 3D AFM image of the annealed  $MoS_2$  sample in sulfur environment, which is deposited at laser energy density,  $200\text{ mJ/cm}^2$ .

---

Another signature of good quality mono and few layers  $MoS_2$  films is its PL response. All  $MoS_2$  samples show A- ( $\sim 675\text{ nm}$ ) / B- ( $\sim 625\text{ nm}$ ) excitons transitions including the thicker samples [Fig. 2-4(c)]. The PL response of  $MoS_2$  also depends on number of layers. The energy band structure of  $MoS_2$  transforms from indirect to direct when its thickness reduce to single layer. This band structure transformation dictates its PL properties, that is, PL intensity decreases exponentially with increasing thickness. This kind of trend could also be observed in our samples, as depicted in [Fig. 2-4(c)]. It can be seen clearly that with the increasing thickness the frequency difference ( $\Delta\omega$ ) of Raman spectra increases, while the PL intensity of A and B excitons decreases rapidly [Fig. 2-4(d)]. Since the PL intensity of B excition is much lower than that of A, therefore the intensity of B exciton

---

is multiplied by a factor of six to make the effect visible in Fig. 2-4(d). Moreover, the FWHM value of 45 s deposited MoS<sub>2</sub> film for direct transition of A excitation was found to be ~72.24 meV, this is much narrower than the previously reported few layers MoS<sub>2</sub> film by PVD method [24] and comparable to the exfoliated MoS<sub>2</sub> on SiO<sub>2</sub> substrate [30].

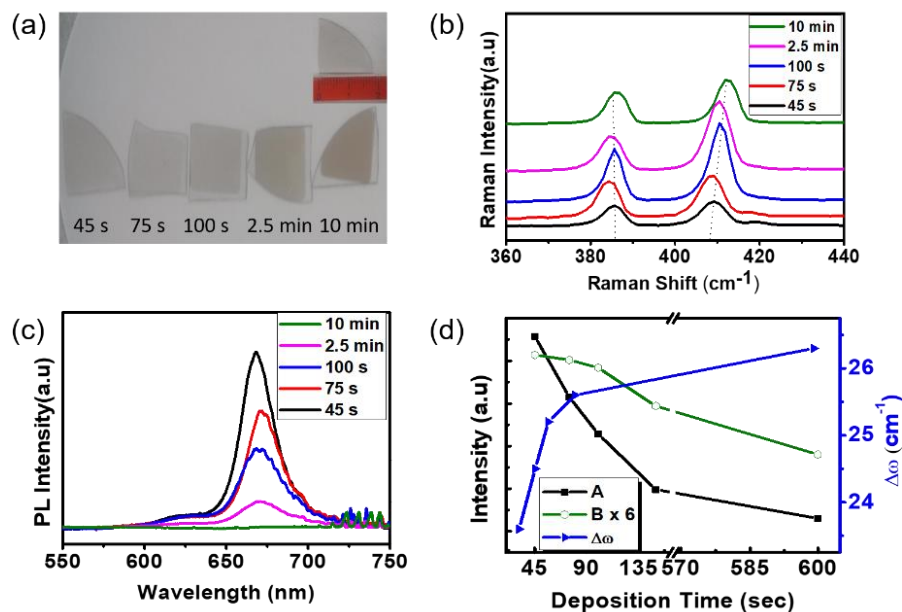


Figure 2- 4(a) CCD images of annealed MoS<sub>2</sub> films on sapphire substrate at various deposition times, (b) Raman, (c) PL spectra's of annealed MoS<sub>2</sub> films deposited at 45 s, 75 s, 100 s, 2.5 min and 10 min respectively, (d) PL intensity of A, B excitons and frequency difference  $\Delta\omega$  (cm<sup>-1</sup>) of Raman spectra with respect to deposition time.

A comparative study was done to study the impact of annealing in sulfur environment. A 45 s deposited sample was cut into two pieces and half of the sample was annealed in sulfur environment. Both samples were characterized by UV-Vis spectrophotometry, PL, Raman, XPS and Hall measurement to examine the effects of annealing process in sulfur-rich environment. In Fig. 2-5(a), the UV-Vis and PL spectra's of as-deposited MoS<sub>2</sub> film are jointly plotted. The deposited sample show extremely weak PL response. Two broad and distorted peaks around ~598 nm and 649 nm can be observed in both absorbance and PL spectra's, respectively. Compared to the absorbance and PL spectra of as-deposited MoS<sub>2</sub> film, the peak positions of A and B excitons



of few layers MoS<sub>2</sub> crystalline are blue shifted. The deviation of A- and B-excitons from original positions i.e. ~675 nm and ~625 nm for A and B respectively [4], might be due to some defects and/or impurities in the MoS<sub>2</sub> film. The impurity was later found to be MoO<sub>3</sub> in the XPS result. On the other hand, the sample annealed in sulfur environment show good absorbance spectra and excellent PL response with a strong A- and weak B- excitons at ~668 nm and ~621 nm respectively, which are close to the A and B values for mechanical exfoliated pristine MoS<sub>2</sub>, as depicted in Fig. 2-5(b). Moreover, the FWHM value of PL spectra of MoS<sub>2</sub> film is correlated to the crystallinity. For annealed sample, the FWHM value of A excition is ~72.4 meV while the un-annealed sample does not show any clear peak. The Raman spectra's of both annealed and un-annealed samples are plotted in Fig. 2-5(c). Although the frequency difference ( $\Delta\omega$ ) of both samples are approximately same (~23.6 cm<sup>-1</sup>), however, the FWHM value of E<sub>2g</sub> peak of annealed sample is ~5.38 cm<sup>-1</sup>, which much narrower than the un-annealed sample (13.28 cm<sup>-1</sup>). It can be concluded from Raman and PL results that annealing in sulfur-rich environment greatly improve the crystalline structure of few layers MoS<sub>2</sub> film.

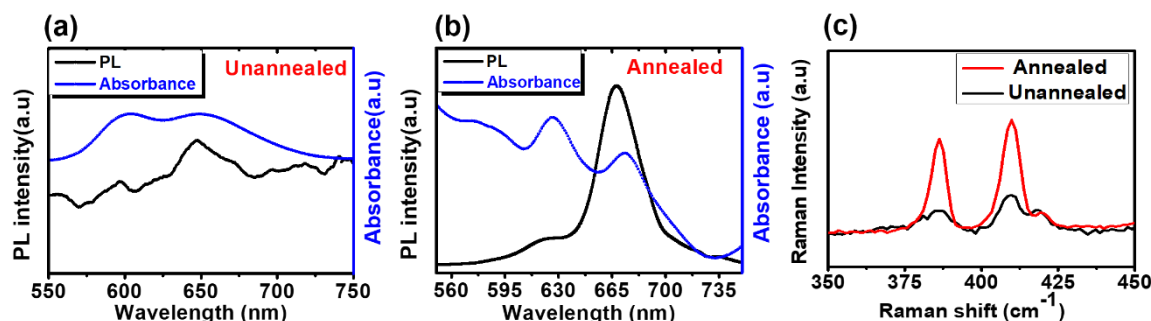


Figure 2- 5 Absorbance and PL spectra of (a) as-deposited MoS<sub>2</sub> film which is approximately three layers, (b) annealed MoS<sub>2</sub> film at 850°C in sulfur environment, (c) comparison of Raman spectra of annealed and as-deposited MoS<sub>2</sub> film.

To further investigate the chemical composition and the presence of residues, XPS spectra were conducted. For comparison, Mo 3d XPS spectra's of both (annealed/un-annealed) samples are depicted in Fig. 2-6(a). Two prominent peaks 229.1 eV and 232.2 eV can be observed in both samples. These peaks corresponds to Mo 3d<sup>5/2</sup> and Mo 3d<sup>3/2</sup> from MoS<sub>2</sub>. However, beside these two



peaks there is another strong peak at 235.65 eV in the XPS spectra of un-annealed sample. This peak corresponds to Mo 3d<sup>3/2</sup> from MoO<sub>3</sub>. Although we used MoS<sub>2</sub> as the target, but during the deposition process the sulfur species could have evaporated for the oxygen to fill the vacancies. The MoO<sub>3</sub> contents were also found in three layer MoS<sub>2</sub> film deposited by magnetron sputtering using pure MoS<sub>2</sub> target [24]. However, the peak at 235.65 eV from MoO<sub>3</sub> suppressed in the annealed sample. Furthermore, the intensity of S 2s (226.3 eV) peak increases, which indicates that the maximum oxygen impurity atoms had been replaced by sulfur atoms. Fig. 2-6(b) depicts the S 2p spectrum, which shows two peaks at 161.8 and 163.04 eV, corresponding to S 2p<sup>3/2</sup> and S 2p<sup>1/2</sup> respectively. The removal of MoO<sub>3</sub> contents from MoS<sub>2</sub> lattice is important because MoO<sub>3</sub> species can behave like trap sites within the lattice, which can trap charges when passed through it.

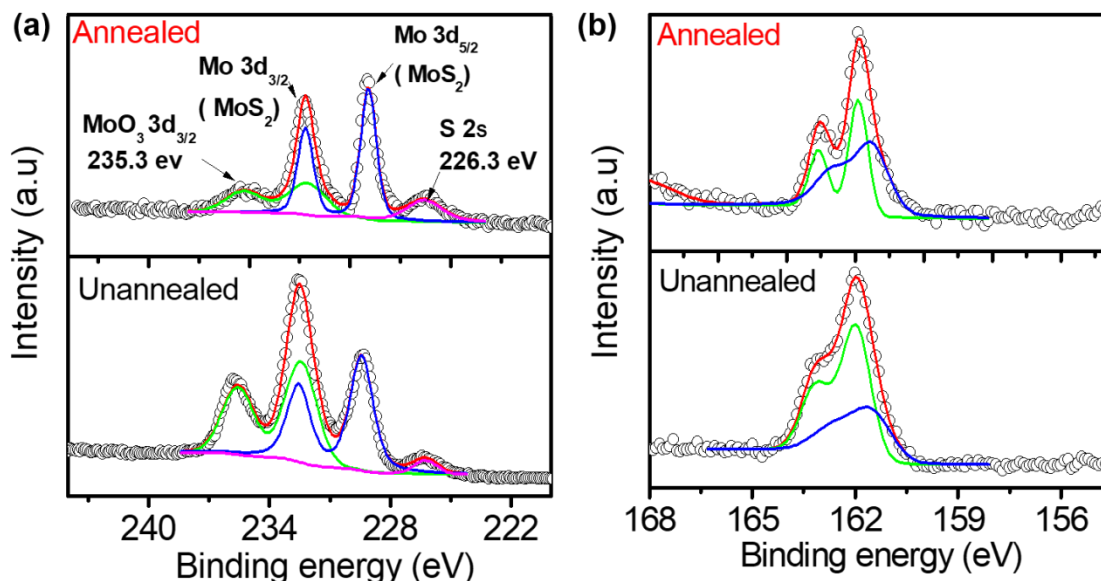


Figure 2- 6 Comparison of (a) Mo 3d and (b) S 2s XPS before and after annealing in sulfur.

Finally, the electrical characterization of the few layers MoS<sub>2</sub> (annealed/un-annealed) film was evaluated. Four silver (Ag) contacts were made at the corners of the approximately 1 cm<sup>2</sup> sample in Van der Pauw geometry. We used HMS-5000 Hall effect measurement system to evaluate carrier type, concentration, and Hall mobility at room temperature. Both annealed and un-annealed few layers MoS<sub>2</sub> films showed n-type semiconducting behavior. The carrier concentration (n),

resistivity ( $\rho$ ) and Hall mobility are shown in Table 2.1. It can be seen from the table that the annealed sample show lower carrier concentration compared with un-annealed. The lower carrier concentration in annealed sample might be due to the filling of sulfur vacancies in MoS<sub>2</sub> lattice after annealing process. On the other hand annealed sample show high mobility (5.47 cm<sup>2</sup>/V.s) compared with un-annealed (1.42 cm<sup>2</sup>/V.s), indicating that the crystal quality has been improved. Furthermore, the Hall mobility of our few layer MoS<sub>2</sub> film is higher compared with that of CVD grown MoS<sub>2</sub> monolayer.

**Table 2.1:** Carrier concentration, resistivity and mobility of few layer annealed and un-annealed MoS<sub>2</sub> specimens

Specimen	Carrier Concentration $n$ (cm <sup>-3</sup> )	Resistivity $\rho$ ( $\Omega$ .cm)	Mobility $\mu$ (cm <sup>2</sup> /V.s)
Un-annealed	$4.05 \times 10^{18}$	1.08	1.42
Annealed	$2.11 \times 10^{17}$	5.41	5.47

## 2.5 Chapter summary

We have demonstrated a two-step synthetic approach for the synthesis of good quality large area ( $\sim 4$  cm<sup>2</sup>) few layers MoS<sub>2</sub> films. Few layers MoS<sub>2</sub> films have been successfully deposited by PLD system followed by annealing in sulphur environment. A comparative was done to study the effect of annealing process. Raman, PL, UV-Vis and XPS study shows the superior quality of the sulfurized sample. The minimum frequency difference ( $\Delta\omega$ ) in Raman spectra of 45 s deposited/annealed sample was found to be 23.6 cm<sup>-1</sup>, corresponds to approximately three monolayers. Moreover, our few layers MoS<sub>2</sub> sample show superior PL as compare to previously reports of few layer MoS<sub>2</sub> by PVD methods. The Hall mobility of our few layers MoS<sub>2</sub> film was found to be 5.47 cm<sup>2</sup>/V.s at room temperature, which is comparable mechanical exfoliated MoS<sub>2</sub> monolayer. Our synthetic approach can extend to other transition metal di-chalcogenide (TMDCs) materials like WS<sub>2</sub>, MoSe<sub>2</sub>, so on, which will be presented in future work.

---

## 2.6 References

- [1]. Chhowalla, M.; Shin, H. S.; Eda, G.; Li, L.-J.; Loh, K. P.; Zhang, H. *Nature chemistry* **2013**, 5, 263.
- [2]. Wang, Q. H.; Kalantar-Zadeh, K.; Kis, A.; Coleman, J. N.; Strano, M. S. *Nature nanotechnology* **2012**, 7, 699-712.
- [3]. Splendiani, A.; Sun, L.; Zhang, Y.; Li, T.; Kim, J.; Chim, C.-Y.; Galli, G.; Wang, F. *Nano letters* **2010**, 10, 1271-1275.
- [4]. Eda, G.; Yamaguchi, H.; Voiry, D.; Fujita, T.; Chen, M.; Chhowalla, M. *Nano Lett.* **2011**, 11, 5111-5116.
- [5]. Lukowski, M. A.; Daniel, A. S.; Meng, F.; Forticaux, A.; Li, L.; Jin, S. *Journal of the American Chemical Society* **2013**, 135, 10274-10277.
- [6]. Perkins, F. K.; Friedman, A. L.; Cobas, E.; Campbell, P.; Jernigan, G.; Jonker, B. T. *Nano letters* **2013**, 13, 668-673.
- [7]. He, Q.; Zeng, Z.; Yin, Z.; Li, H.; Wu, S.; Huang, X.; Zhang, H. *Small* **2012**, 8, 2994-2999.
- [8]. Liu, B.; Chen, L.; Liu, G.; Abbas, A. N.; Fathi, M.; Zhou, C. *ACS Nano* **2014**, 8, 5304-5314.
- [9]. Yin, Z.; Zeng, Z.; Liu, J.; He, Q.; Chen, P.; Zhang, H. *Small* **2013**, 9, 727-731.
- [10]. Wang, J.; Zou, X.; Xiao, X.; Xu, L.; Wang, C.; Jiang, C.; Ho, J. C.; Wang, T.; Li, J.; Liao, L. *Small* **2015**, 11, 208-213.
- [11]. Hao, L.; Gao, W.; Liu, Y.; Han, Z.; Xue, Q.; Guo, W.; Zhu, J.; Li, Y. *Nanoscale* **2015**, 7, 8304-8308.
- [12]. Radisavljevic, B.; Whitwick, M. B.; Kis, A. *ACS Nano* **2011**, 5, 9934-9938.
- [13]. Choi, W.; Cho, M. Y.; Konar, A.; Lee, J. H.; Cha, G. B.; Hong, S. C.; Kim, S.; Kim, J.; Jena, D.; Joo, J. *Adv. Mater.* **2012**, 24, 5832-5836.
- [14]. Jariwala, D.; Sangwan, V. K.; Wu, C.-C.; Prabhumirashi, P. L.; Geier, M. L.; Marks, T. J.; Lauhon, L. J.; Hersam, M. C. *Proceedings of the National Academy of Sciences* **2013**, 110, 18076-18080.
- [15]. Radisavljevic, B.; Radenovic, A.; Brivio, J.; Giacometti, V.; Kis, A. *Nature nanotechnology* **2011**, 6, 147-150.

- 
- [16]. Yin, Z.; Li, H.; Li, H.; Jiang, L.; Shi, Y.; Sun, Y.; Lu, G.; Zhang, Q.; Chen, X.; Zhang, H. *ACS Nano* **2011**, 6, 74-80.
- [17]. Zhang, W.; Huang, J. K.; Chen, C. H.; Chang, Y. H.; Cheng, Y. J.; Li, L. J. *Adv. Mater.* **2013**, 25, 3456-3461.
- [18]. Kim, S.; Konar, A.; Hwang, W.-S.; Lee, J. H.; Lee, J.; Yang, J.; Jung, C.; Kim, H.; Yoo, J.-B.; Choi, J.-Y. *Nature communications* **2012**, 3, 1011.
- [19]. Natori, K. *J. Appl. Phys.* **1994**, 76, 4879-4890.
- [20]. Huang, X.; Zeng, Z.; Zhang, H. *Chem. Soc. Rev.* **2013**, 42, 1934-1946.
- [21]. Lin, Y.-C.; Zhang, W.; Huang, J.-K.; Liu, K.-K.; Lee, Y.-H.; Liang, C.-T.; Chu, C.-W.; Li, L.-J. *Nanoscale* **2012**, 4, 6637-6641.
- [22]. HeeáRyu, G.; HoáCho, J. *Nanoscale* **2014**, 6, 2821-2826.
- [23]. Liu, K.-K.; Zhang, W.; Lee, Y.-H.; Lin, Y.-C.; Chang, M.-T.; Su, C.-Y.; Chang, C.-S.; Li, H.; Shi, Y.; Zhang, H. *Nano letters* **2012**, 12, 1538-1544.
- [24]. Muratore, C.; Hu, J.; Wang, B.; Haque, M.; Bultman, J.; Jespersen, M.; Shamberger, P.; McConney, M.; Naguy, R.; Voevodin, A. *Applied Physics Letters* **2014**, 104, 261604.
- [25]. Li, S.-L.; Miyazaki, H.; Song, H.; Kuramochi, H.; Nakaharai, S.; Tsukagoshi, K. *ACS nano* **2012**, 6, 7381-7388.
- [26]. Zeng, H.; Dai, J.; Yao, W.; Xiao, D.; Cui, X. *Nature nanotechnology* **2012**, 7, 490-493.
- [27]. Lee, C.; Yan, H.; Brus, L. E.; Heinz, T. F.; Hone, J.; Ryu, S. *ACS nano* **2010**, 4, 2695-2700.
- [28]. Verble, J.; Wietling, T.; Reed, P. *Solid State Communications* **1972**, 11, 941-944.
- [29]. Lee, Y. H.; Zhang, X. Q.; Zhang, W.; Chang, M. T.; Lin, C. T.; Chang, K. D.; Yu, Y. C.; Wang, J. T. W.; Chang, C. S.; Li, L. J. *Adv. Mater.* **2012**, 24, 2320-2325.
- [30]. Mak, K. F.; Lee, C.; Hone, J.; Shan, J.; Heinz, T. F. *Phys. Rev. Lett.* **2010**, 105, 136805.
-

---

## Chapter 3 Pulse Laser Deposition Assisted Grown Continuous Monolayer MoSe<sub>2</sub>

### 3.1 Introduction:

Each member of TMDCs family is receiving tremendous attention from the last few years and are likely to stay the focus of future research by virtue of their rich physics and technologically important properties [1-6]. Structurally, they are crystal analogue of graphene. Moreover, their excellent properties of flexibility, carrier mobility, and sunlight absorption make them prospective candidates for applications in flexible light weight electronics, optoelectronics, and energy conversion devices [7-11]. The properties of semiconducting MX<sub>2</sub> materials can be varied by changing the atomic arrangement, dimensionality (thickness), and chemical composition. Among MX<sub>2</sub>, monolayer MoS<sub>2</sub> has been extensively studied for various applications, such as, diodes [12, 13], photodetector [14], gas sensors [15], and solar cells [16]. The chalcogen compounds including MoSe<sub>2</sub> and WSe<sub>2</sub> are also of great importance of both fundamental studies and devices.

### 3.2 Motivation:

Recently, another member of TMDCs family, monolayer MoSe<sub>2</sub>, gained attention by virtue of its remarkable properties similar or in some instances better than those of MoS<sub>2</sub> [17-19]. It has been experimentally shown that monolayer MoSe<sub>2</sub> based phototransistor exhibits a much faster response time than MoS<sub>2</sub> at room temperature in ambient conditions [20]. However, the low reactivity of selenium (Se) makes it more difficult to synthesize a good quality, uniform, continuous monolayer MoSe<sub>2</sub> [21].

From synthesis standpoint, a few synthetic approaches are reported for monolayer MoSe<sub>2</sub> film. Coloman et al reported top down approach to synthesize mono and bilayer of various TMDCs nanosheets, including MoSe<sub>2</sub>, from their bulk counterpart [22]. They found that bulk TMDCs, can be dispersed in solvents with surface tension close to 40mJ/m<sup>2</sup>. Although this method is generalized, it is constrained in producing continuous film required for practical devices. In bottom up approaches, similar to MoS<sub>2</sub>, CVD has been widely adopted for monolayer MoSe<sub>2</sub> synthesis [23-24]. However, in case of Se, it is extremely difficult to

---

produce uniform continuous monolayer film by conventional CVD method with repeatability owing to the long reaction time that is usually required for MoSe<sub>2</sub> synthesis due to the low reactivity of Se. Moreover, MoSe<sub>2</sub> growth on SiO<sub>2</sub> or sapphire is not self-limiting like graphene on copper foil [25], the long growth time could inevitably result in growth of extra layers. To avoid the growth of extra layers, we believe that precise control of MoO<sub>3</sub> precursor is required. Currently, it is still challenging to develop an approach for synthesis of good quality MoSe<sub>2</sub> on technologically important substrates, such as, SiO<sub>2</sub> or sapphire, that have no self-limiting properties. To solve the above challenge, PLD can be a useful technique to precisely control the MoO<sub>3</sub> amount, by controlling laser energy and deposition time. To the best of our knowledge, there is no study on synthesizing continuous monolayer TMDCs, particularly MoSe<sub>2</sub> related to PLD. We have found a report on direct deposition of MoS<sub>2</sub> multi-layers with no exact information of film thickness [26].

In this chapter, we present the synthesis of good quality, uniform and continuous monolayer MoSe<sub>2</sub> using PLD as the assisted process for growing MoO<sub>3</sub> thin film, and then using a selenization process to obtain monolayer MoSe<sub>2</sub> film. We also investigate the effect of laser energy on the resultant MoSe<sub>2</sub> film. The X-ray photoelectron spectroscopy (XPS) was used to confirm the formation of MoSe<sub>2</sub>. A two-dimensional grazing incidence X-ray diffraction (2D-GIXD) measurement was employed to study the crystallization of as-synthesized monolayer MoSe<sub>2</sub>. The morphological, Raman, and photoluminescence spectroscopy were used to examine the uniformity, continuity and optical properties of as-synthesized monolayer MoSe<sub>2</sub>.

### **3.3 Experiment details:**

The experimental details of each step is give below

#### **3.3.1 MoO<sub>3</sub> target preparation:**

Approximately 13 g of pure MoO<sub>3</sub> (99.99 %, Alfa) were initially placed at 100°C to remove the moisture. The powder were ball milled in ethanol for more than 24 hours. The milled powder were dried to remove the ethanol. The powder were molded to form circular target with approximately 2 cm diameter at pressure of 5 tons. The target was annealed at 700°C for 12 hours.

---

### 3.3.2 MoO<sub>3</sub> film by pulse laser deposition:

The schematic illustration for continuous monolayer MoSe<sub>2</sub> by selenization of PLD deposited MoO<sub>3</sub> film is given in the Fig. 1-5. The growth procedure for monolayer MoSe<sub>2</sub> by PLD assisted selenization method is as follows: the chamber pressure was initially reduced to the base value  $5 \times 10^{-7}$  Torr. Highly pure MoO<sub>3</sub> target was placed in rotating target holder. The possible surface contaminants aggregated on the target were removed by exposing the target to high energy laser beam for few minutes. The substrate was placed in a rotating substrate holder. The distance between substrate and target was set to 10 cm. A krypton fluoride (KrF) excimer laser ( $\lambda=248$  nm, CompexPro 102F) with 20 ns pulse width was used. MoO<sub>3</sub> thin films were deposited at various laser energies (given in main text) with repetition rate of 3Hz (# of laser shots on the target per second) and deposition time of 20 s. The substrate temperature was maintained at 200°C.

### 3.3.3 Selenization of MoO<sub>3</sub> films

To convert the MoO<sub>3</sub> films to MoSe<sub>2</sub>, the deposited MoO<sub>3</sub> films were selenized in a two zones hot-wall furnace system [Fig. 1-5 (b)]. Approximately 0.30 gram of pure selenium powder (99.99 %, Alfa) was placed in graphite crucible. The PLD deposited MoO<sub>3</sub> sample was placed 15 cm away from the selenium powder in the quartz tube. The tube pressure was reduced to the base value of 60 mtorr. Initially, pure Ar gas was flashed into the quartz tube repeatedly to clean the oxygen contaminants. The temperatures of zone-1 and zone-2 were set to 450 °C and 900 °C respectively. The tube pressure was maintained to 550 torr during the selenization process. A total 25 min reaction time was given.

## 3.4 Result and discussion:

Fig. 3-1(a) schematically show the growth process for monolayer MoSe<sub>2</sub> by PLD assisted selenization method. Initially, a krypton fluoride (KRF) excimer laser ( $\lambda=248$  nm, pulse width=20 ns) was used to deposit thin films of MoO<sub>3</sub> on SiO<sub>2</sub>/Si substrate. The as-deposited MoO<sub>3</sub> films were converted to MoSe<sub>2</sub> by the selenization process in a two zone hot-wall furnace. Two-zone furnace was chosen so that the specified temperatures of Se and MoO<sub>3</sub> can be achieved simultaneously and independently. Se powder was placed at temperature zone-1(450°C) and PLD deposited MoO<sub>3</sub> film was placed at temperature zone-2(900°C),

---

respectively. The mixture of Ar and H<sub>2</sub> gas were employed as the carrier gases to drive the Se vapours from zone-1 to the MoO<sub>3</sub> film at zone-2. H<sub>2</sub> gas also acts as an assisted gas in reducing MoO<sub>3</sub> during the selenization process. At 900 °C, the selenization reaction occurs to convert MoO<sub>3</sub> into crystallized MoSe<sub>2</sub>. A reaction time of 25 min was set to ensure the complete conversion of MoO<sub>3</sub> into MoSe<sub>2</sub>. One of the possible reactions inside the chamber could be as follows:



The bond interaction of the as-synthesized MoSe<sub>2</sub> on SiO<sub>2</sub>/Si substrate was studied through X-ray photoelectron spectroscopy (XPS) as shown in Fig. 3-1(b) for Mo 3d survey and in Fig. 3-1(c) for Se 3d survey. The Mo 3d survey shows that the Mo 3d<sub>5/2</sub> and 3d<sub>3/2</sub> peaks, which typically perform the appearance of MoSe<sub>2</sub> are located at 228.68 eV and 231.83 eV, respectively. The Mo 3d peak from MoO<sub>3</sub> at about 236 eV, which indicate the presence of MoO<sub>3</sub> [17], is absent in Mo 3d scan. This result confirms that the MoO<sub>3</sub> film has been completely selenized (no residues of MoO<sub>3</sub>). Moreover, the 3d scan of Se shows two prominent peaks around 54.19 eV and 55.05 eV, which correspond to Se 3d<sub>5/2</sub> and 3d<sub>3/2</sub>, respectively. These results agree with previous report on XPS analysis of MoSe<sub>2</sub> [10].

---



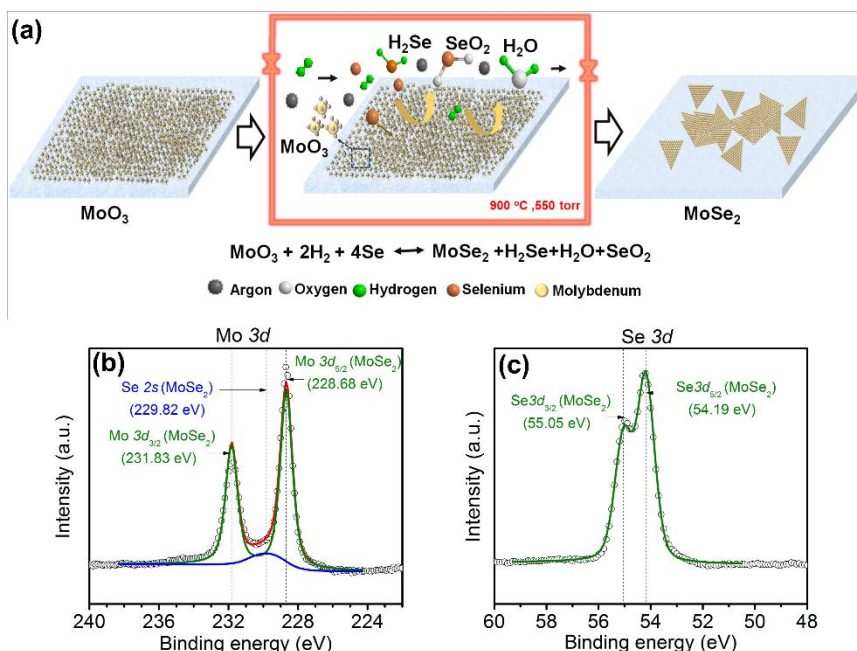


Figure 3- 1(a) Schematic illustration of the growth mechanism of monolayer MoSe<sub>2</sub>, and the XPS results for the (b) Mo3d survey and(c) Se3d survey.

The effect of laser energy, in PLD process, on the resultant MoSe<sub>2</sub> film was checked by depositing MoO<sub>3</sub> films with different laser energies. Fig. 3-2 shows the optical microscope (OM) images of the resultant MoSe<sub>2</sub> films after selenization. The 150 mJ of laser energy results in several grains of MoSe<sub>2</sub> particles (approximately 1 μm in size) on the film. It is likely that high laser energy (150 mJ) results in deposition of several grains MoO<sub>3</sub> particles, which are then converted into MoSe<sub>2</sub> particles after selenization. The size and density of the grain particles were found to decrease with decreasing laser energy, as shown in Fig. 3-3(a) and (b). A highly uniform continuous monolayer without grain particles was obtained, when the laser energy was reduced to 100 mJ [Fig. 3-2(c)]. However, when the laser energy was further reduced to 90 mJ, the resultant MoSe<sub>2</sub> film was discontinuous, and comprised of extremely tiny irregular flakes [Fig. 3-2(d)]. These results suggest that growth of MoO<sub>3</sub> precursor at 100 mJ laser energy is not too high to form extra-layers and is not too low to obtain the discontinuous grains. The MoSe<sub>2</sub> film with 100 mJ was chosen for further characterization because its monolayer surface is uniform and continuous without any grain particles.

---

The surface morphology of the as-grown monolayer MoSe<sub>2</sub> film by PLD assisted method with 100 mJ of laser energy was investigated, as shown in Fig. 3-3. Field emission scanning electron microscopy (FE-SEM) images were taken at different spots on the sample. The grown film was found to be dominantly continuous monolayer. Domains of small isolated dense triangular flakes were also found at the margins of continuous monolayer MoSe<sub>2</sub>. The size of triangular flakes was found to be 2 to 4  $\mu\text{m}$ , as depicted in Fig. 3-3(a). Similar to the growth of monolayer MoSe<sub>2</sub>, by conventional CVD [10], these triangles were merged together and a continuous film was formed. The boundary region of the isolated flakes and continuous monolayer MoSe<sub>2</sub> film is shown in Fig. 3-4(b), the continuous film with some small discontinuities is shown in Fig. 3-3(c), and the highly uniform film with no discontinuities is given in Fig. 3-3(d). Moreover, the grain boundaries cannot be identified in the FE-SEM images of continuous film, indicating good lateral alignment of the triangular grains. The surficial morphology of the sample was almost found to be either monolayer flakes or continuous film. However, regions with bilayer, tri layer and bulk were also observed. The growth of second layer domains may indicate the presence of defects in the first layer. These defects may act as nucleation sites for the growth of second layer [10]. Furthermore, the topographic images with thickness profile, obtained using atomic force microscopy (AFM), were used to check the thickness of continuous monolayer MoSe<sub>2</sub> [Fig. 3-3(e)] and flake MoSe<sub>2</sub> [Fig. 3-3(f)] which were found to be about 1.0 and 1.2 nm, respectively. These results confirm that the as-grown flakes and continuous film of MoSe<sub>2</sub> is indeed single layer. The crystalized structure of as-synthesized MoSe<sub>2</sub> was investigated using a grazing incidence X-ray diffraction is shown in Fig. 3-4. At  $q_z=0$ , the diffraction peaks which are observed in the in-plane direction ( $q_{xy}$ ) perform the crystallize structure of monolayer MoSe<sub>2</sub>. A peak at  $q_{xy}= 2.2 \text{ \AA}^{-1}$  and a peak at  $q_{xy}= 3.8 \text{ \AA}^{-1}$  in the in-plane direction which respectively correspond to (10) and (11) identify the hexagonal structure of monolayer MoSe<sub>2</sub>.

---

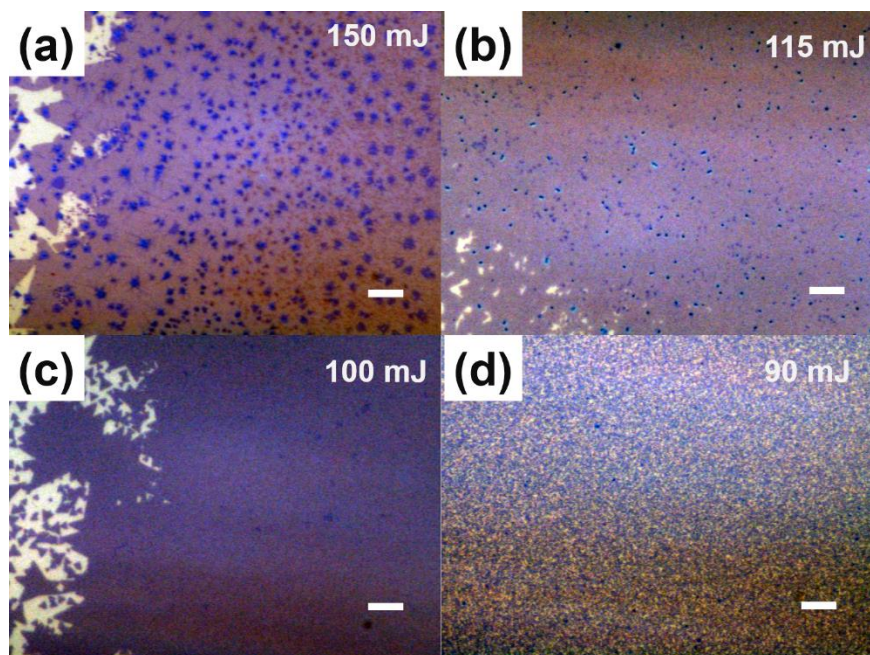


Figure 3- 2 OM images of MoSe<sub>2</sub> on the SiO<sub>2</sub> substrate corresponding to the MoO<sub>3</sub> film deposited at (a) 150mJ, (b) 115mJ, (c) 100mJ and (d) 90mJ, respectively. The scale bar is 15μm.

---

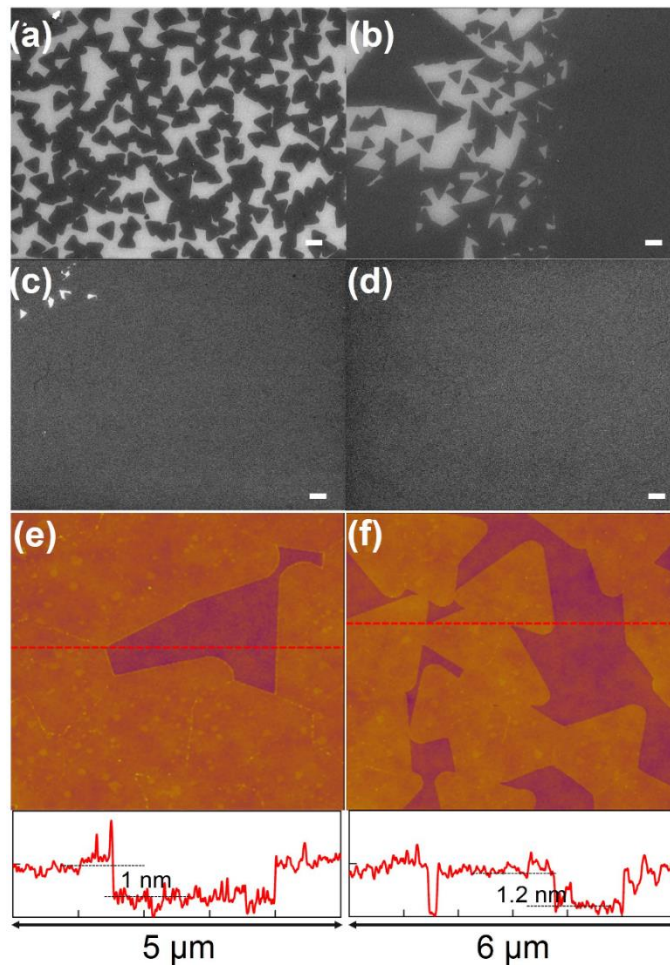


Figure 3- 3 FE-SEM images of monolayer MoSe<sub>2</sub> (a) isolated flakes (b) boundary between flakes and continuous film (c) continuous film with some discontinuities at top left area (d) continuous film and (e-f) AFM image and thickness profiles of continuous film and isolated flakes. The scale bar is 2  $\mu\text{m}$ .

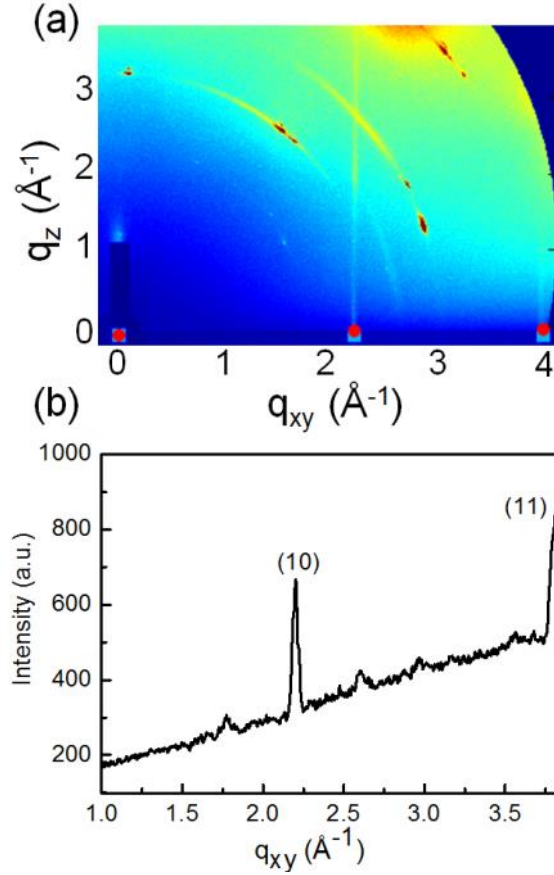


Figure 3- 4 2D GIXD characterization of monolayer MoSe<sub>2</sub> including (a) 2D GIXD image and (b) cross-section profiles of 2D GIXD image at  $q_z=0$ .

Raman scattering has been used as an effective indirect tool for characterization of crystal quality of 2D materials. The sharp Raman peaks with low full width half maximum (FWHM) values indicate the good crystalline nature of the film [28]. Raman scattering is also strongly dependent on the number of layers and therefore, has been exploited for estimating the film thickness [29]. PL spectroscopy can effectively determine the band gap of semiconducting materials [30]. The Raman and PL spectra's of PLD assisted grown continuous monolayer MoSe<sub>2</sub> film was characterized using a 532.5 nm excitation wavelength at room temperature. The Raman spectrum from monolayer continuous MoSe<sub>2</sub> is given in Fig. 3-5(a). Two main peaks associated with the A<sub>1g</sub> (out of plane) and E<sub>2g</sub><sup>1</sup> (in-plane) vibrational modes were observed at 241.7 cm<sup>-1</sup> and 287.9 cm<sup>-1</sup>, respectively. The FWHM of A<sub>1g</sub> peak is found to be 3.7 cm<sup>-1</sup>, which is less than that of mechanically exfoliated commercial monolayer MoSe<sub>2</sub>. This indicates that the grown MoSe<sub>2</sub> is highly crystalline. In

---

addition, the peak associated with interlayer interaction around  $353\text{ cm}^{-1}$  cannot be observed,<sup>111</sup> which suggests that our grown MoSe<sub>2</sub> film is indeed single layer. The PL spectrum of continuous monolayer MoSe<sub>2</sub> is depicted in Fig. 3-5(b). It is well known that bulk MoSe<sub>2</sub> has an indirect band gap of 1.1 eV, and negligible PL intensity. The PL spectrum of as-synthesized monolayer MoSe<sub>2</sub> shows a prominent emission peak at about 805 nm, corresponding to a band gap of 1.54 eV, attributed to direct band gap transition from the so called A excitons, located at the K point of the Brillouin zone [19]. The PL result further confirms that the grown MoSe<sub>2</sub> film is single layer. The FWHM of PL was found to be 24 nm, comparable with mechanically exfoliated monolayer MoSe<sub>2</sub> [32]. Moreover, the band gap of PLD assisted grown monolayer MoSe<sub>2</sub> is in good agreement with previously reported band gap of CVD grown monolayer MoSe<sub>2</sub> [33].

To check the uniformity and homogeneity of continuous monolayer MoSe<sub>2</sub>, Raman (A<sub>1g</sub> mode) and PL intensity mapping were done at the highlighted region in Fig. 3-5(c), and depicted in Fig. 3-5(d) and Fig. 3-5(e), respectively. Both the Raman and PL maps show almost uniform brightness indicating the uniform and homogeneous nature of MoSe<sub>2</sub> film. To study the uniformity over large area, Raman and PL spectra were taken at different spots on a continuous film [Fig. 3-6 (a)]. The Raman spectra show almost identical behaviour, indicating uniformity over large area, as depicted in Fig. 3-6 (b). The band gap of monolayer MoSe<sub>2</sub> was found between 1.53 eV to 1.56 eV over the entire region [Fig. 3-6(c-d)]. Furthermore, the film quality has also been confirmed by the rotational angle second harmonic generation (RA-SHG) technique in our previous publication [34]. The SHG results showed six-petal pattern, indicating good crystalline nature of the grown film (Fig. 3-7). Finally, the same growth conditions were also applied on a sapphire substrate and similar results were obtained. The OM images, Raman and PL spectra of monolayer MoSe<sub>2</sub> film grown on sapphire substrate are given in Fig. 3-8.



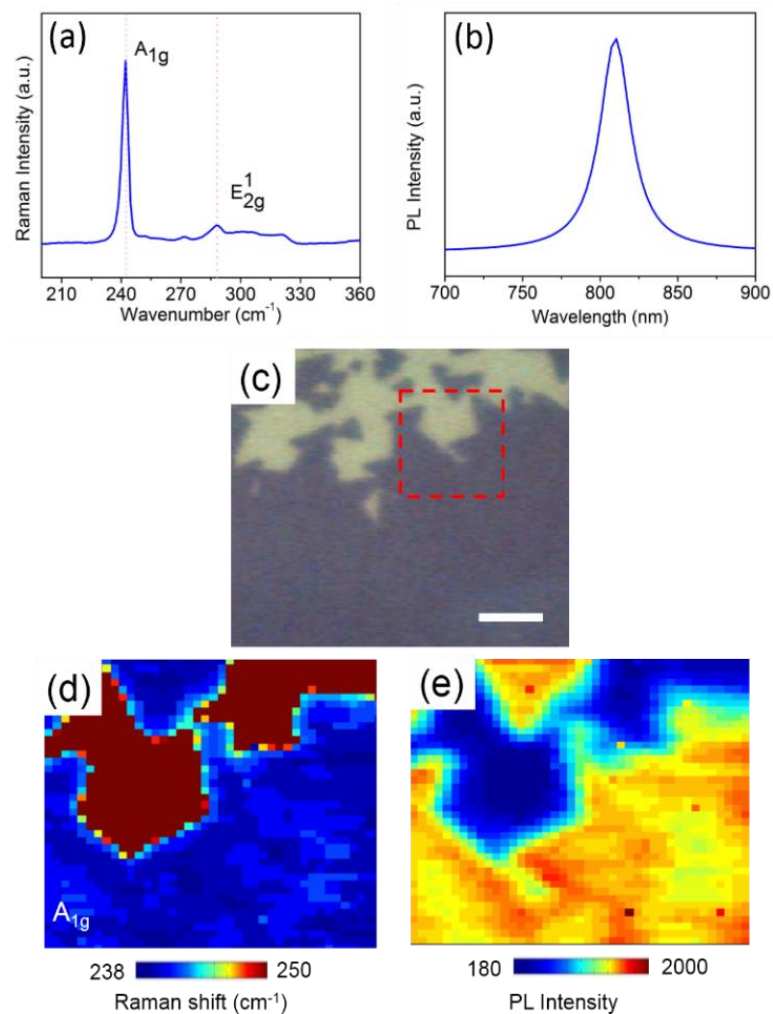


Figure 3- 5 Raman and PL characterization of monolayer MoSe<sub>2</sub> (a) Raman spectrum (b) PL spectrum (c) OM image (d) Raman mapping with respect to A<sub>1g</sub> peak and (e) PL Intensity mapping of the highlighted region in (c). The scale bar is 10  $\mu$ m.

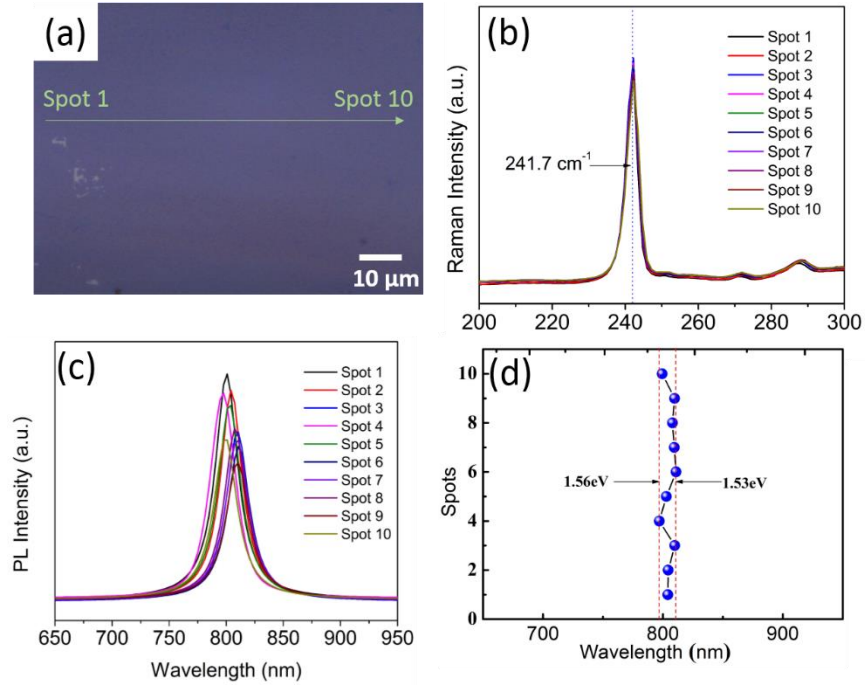


Figure 3- 6 (a) Optical microscope image of continuous monolayer MoSe<sub>2</sub> (c) Raman and (d) photoluminescence spectra taken at spot 1 to 10 with step size ~10 μm.



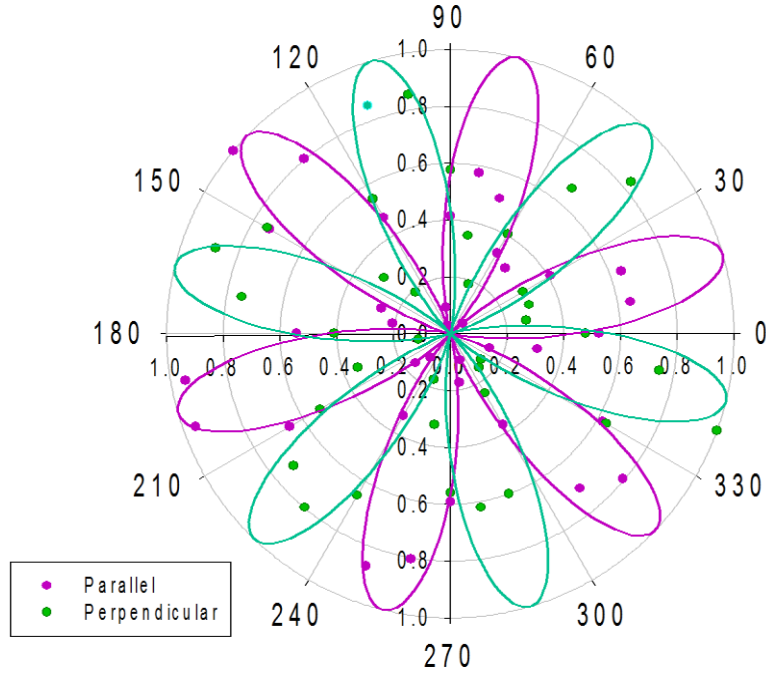


Figure 3- 7 Azimuthal symmetry of PLD-assisted grown MoSe2 analyzed by RA-SHG . The solid traces are fit curves corresponding to  $\cos^2[3(\theta + \theta_0)]$  and  $\sin^2[3(\theta + \theta_0)]$ , where  $\theta$  denotes the angle between the incident linearly polarized electric field and the mirror axis of the crystal and  $\theta_0$  denotes the initial angular offset.

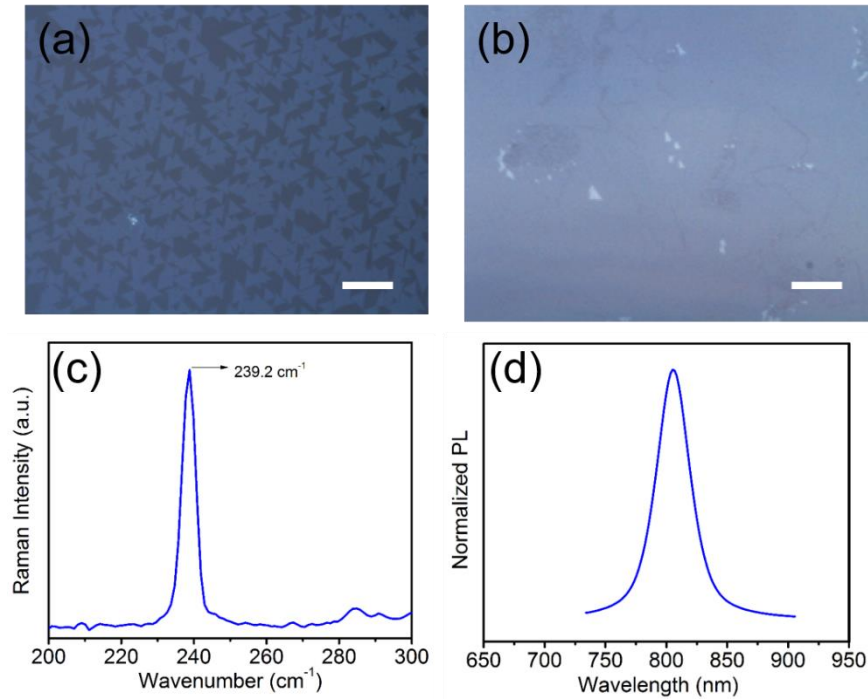


Figure 3- 8 3-1 Monolayer MoSe<sub>2</sub> on sapphire substrate by PLD assisted method (a) flakes (b) continuous film (c) Raman and (d) photoluminescence spectra. The scale bar is 30  $\mu\text{m}$

### 3.5 Chapter summary

We have successfully grown monolayer MoSe<sub>2</sub> by using a PLD assisted selenization process. The key factor to obtain uniform monolayer film was found to be the precise amount of MoO<sub>3</sub> precursor, which can be precisely control by the laser energy and deposition time. From optical spectroscopy results, the grown MoSe<sub>2</sub> film show strong PL emission at 805 nm, with FWHM of 24 nm, at room temperature reveal the excellent optical quality of the film. Raman fingerprint corresponds to monolayer were observed. The morphological characterizations clearly display that the grown MoSe<sub>2</sub> film is continuous monolayer with homogeneous thickness. These results imply that PLD assisted selenization process is a reliable method for preparing good quality film, which can be used for a variety of applications including field effect transistors (FETs), light emitting diodes (LEDs), hydrogen evolution, gas sensors and photo sensors etc. Moreover, this approach is not

---

limited to MoSe<sub>2</sub> only and can be applied to synthesize various other TMDCs materials, such as, MoS<sub>2</sub>, WS<sub>2</sub> and WSe<sub>2</sub>.

### 3.6 References

- [1] Rivera, P.; Seyler, K. L.; Yu, H.; Schaibley, J. R.; Yan, J.; Mandrus, D. G.; Yao, W.; Xu, X. *Science* **2016**, 351, 688-691.
- [2] Conley, H. J.; Wang, B.; Ziegler, J. I.; Haglund Jr, R. F.; Pantelides, S. T.; Bolotin, K. I. *Nano lett.* **2013**, 13, 3626-3630.
- [3] Aivazian, G.; Gong, Z.; Jones, A. M.; Chu, R.-L.; Yan, J.; Mandrus, D. G.; Zhang, C.; Cobden, D.; Yao, W.; Xu, X. *Nat. Phys.* **2015**.
- [4] Radisavljevic, B.; Radenovic, A.; Brivio, J.; Giacometti, V.; Kis, A. *Nat. nanotechnol.* **2011**, 6, 147-150.
- [5] Zhao, W.; Ribeiro, R. M.; Toh, M.; Carvalho, A.; Kloc, C.; Castro Neto, A.; Eda, G. *Nano lett.* **2013**, 13, 5627-5634.
- [6] Chhowalla, M.; Shin, H. S.; Eda, G.; Li, L.-J.; Loh, K. P.; Zhang, H. *Nat. chem.* **2013**, 5, 263-275.
- [7] Splendiani, A.; Sun, L.; Zhang, Y.; Li, T.; Kim, J.; Chim, C.-Y.; Galli, G.; Wang, F. *Nano lett.* **2010**, 10, 1271-1275.
- [8] Zhao, W.; Ghorannevis, Z.; Chu, L.; Toh, M.; Kloc, C.; Tan, P.-H.; Eda, G. *ACS Nano* **2012**, 7, 791-797.
- [9] He, Q.; Zeng, Z.; Yin, Z.; Li, H.; Wu, S.; Huang, X.; Zhang, H. *Small* **2012**, 8, 2994-2999.
- [10] Wang, X.; Gong, Y.; Shi, G.; Chow, W. L.; Keyshar, K.; Ye, G.; Vajtai, R.; Lou, J.; Liu, Z.; Ringe, E. *ACS Nano* **2014**, 8, 5125-5131.
- [11] Bernardi, M.; Palummo, M.; Grossman, J. C. *Nano lett.* **2013**, 13, 3664-3670.
- [12] Deng, Y.; Luo, Z.; Conrad, N. J.; Liu, H.; Gong, Y.; Najmaei, S.; Ajayan, P. M.; Lou, J.; Xu, X.; Ye, P. D. *ACS Nano* **2014**, 8, 8292-8299.
- [13] Cheng, R.; Li, D.; Zhou, H.; Wang, C.; Yin, A.; Jiang, S.; Liu, Y.; Chen, Y.; Huang, Y.; Duan, X. *Nano lett.* **2014**, 14, 5590-5597.
- [14] Lopez-Sanchez, O.; Lembke, D.; Kayci, M.; Radenovic, A.; Kis, A. *Nat. nanotechnol.* **2013**, 8, 497-501.

- 
- [15] Li, H.;Yin, Z.;He, Q.;Li, H.;Huang, X.;Lu, G.;Fam, D. W. H.;Tok, A. I. Y.;Zhang, Q.; Zhang, H. *small* **2012**, 8, 63-67.
- [16] Tsai, M.-L.;Su, S.-H.;Chang, J.-K.;Tsai, D.-S.;Chen, C.-H.;Wu, C.-I.;Li, L.-J.;Chen, L.-J.; He, J.-H. *ACS Nano* **2014**, 8, 8317-8322.
- [17] Tongay, S.;Zhou, J.;Ataca, C.;Lo, K.;Matthews, T. S.;Li, J.;Grossman, J. C.; Wu, J. *Nano lett.* **2012**, 12, 5576-5580.
- [18] Lee, C.;Yan, H.;Brus, L. E.;Heinz, T. F.;Hone, J.; Ryu, S. *ACS Nano* **2010**, 4, 2695-2700.
- [19] Ross, J. S.;Wu, S.;Yu, H.;Ghimire, N. J.;Jones, A. M.;Aivazian, G.;Yan, J.;Mandrus, D. G.;Xiao, D.; Yao, W. *Nat. commun.* **2013**, 4, 1474.
- [20] Chang, Y.-H.;Zhang, W.;Zhu, Y.;Han, Y.;Pu, J.;Chang, J.-K.;Hsu, W.-T.;Huang, J.-K.;Hsu, C.-L.; Chiu, M.-H. *ACS Nano* **2014**, 8, 8582-8590.
- [21] Tsirlina, T.;Feldman, Y.;Homyonfer, M.;Sloan, J.;Hutchison, J.; Tenne, R. *Fullerene. sci. technol.* **1998**, 6, 157-165.
- [22] Coleman, J. N.;Lotya, M.;O'Neill, A.;Bergin, S. D.;King, P. J.;Khan, U.;Young, K.;Gaucher, A.;De, S.; Smith, R. J. *Science* **2011**, 331, 568-571.
- [23] Shim, G. W.;Yoo, K.;Seo, S.-B.;Shin, J.;Jung, D. Y.;Kang, I.-S.;Ahn, C. W.;Cho, B. J.; Choi, S.-Y. *ACS Nano* **2014**, 8, 6655-6662.
- [24] Lu, X.;Utama, M. I. B.;Lin, J.;Gong, X.;Zhang, J.;Zhao, Y.;Pantelides, S. T.;Wang, J.;Dong, Z.; Liu, Z. *Nano lett.* **2014**, 14, 2419-2425.
- [25] Li, X.;Cai, W.;An, J.;Kim, S.;Nah, J.;Yang, D.;Piner, R.;Velamakanni, A.;Jung, I.; Tutuc, E. *Science* **2009**, 324, 1312-1314.
- [26] Late, D. J.;Shaikh, P. A.;Khare, R.;Kashid, R. V.;Chaudhary, M.;More, M. A.; Ogale, S. B. *ACS appl. mater. interfaces* **2014**, 6, 15881-15888.
- [27] Muratore, C.;Hu, J.;Wang, B.;Haque, M.;Bultman, J.;Jespersen, M.;Shamberger, P.;McConney, M.;Naguy, R.; Voevodin, A. *Appl.Phys.Lett.* **2014**, 104, 261604.
- [28] Ramakrishna Matte, H.;Gomathi, A.;Manna, A. K.;Late, D. J.;Datta, R.;Pati, S. K.; Rao, C. *Angew.Chem.Int.Ed.* **2010**, 122, 4153-4156.
- [29] Li, H.;Zhang, Q.;Yap, C. C. R.;Tay, B. K.;Edwin, T. H. T.;Olivier, A.; Baillargeat, D. *Adv. Funct. Mater.* **2012**, 22, 1385-1390.
-

- 
- [30] Eda, G.; Yamaguchi, H.; Voiry, D.; Fujita, T.; Chen, M.; Chhowalla, M. *Nano lett.* **2011**, 11, 5111-5116.
- [31] Tonndorf, P.; Schmidt, R.; Böttger, P.; Zhang, X.; Börner, J.; Liebig, A.; Albrecht, M.; Kloc, C.; Gordan, O.; Zahn, D. R. *Opt. Express* **2013**, 21, 4908-4916.
- [32] Island, J. O.; Kuc, A.; Diependaal, E. H.; Bratschitsch, R.; van der Zant, H. S.; Heine, T.; Castellanos-Gomez, A. *Nanoscale* **2016**, 8, 2589-2593.
- [33] Shaw, J. C.; Zhou, H.; Chen, Y.; Weiss, N. O.; Liu, Y.; Huang, Y.; Duan, X. *Nano Res.* **2014**, 7, 511-517.
- [34] Le, C. T.; Clark, D. J.; Ullah, F.; Senthilkumar, V.; Jang, J. I.; Sim, Y.; Seong, M. J.; Chung, K. H.; Park, H.; Kim, Y. S. *Ann. Phys.(Berlin)* **2016**, in press DOI :10.1002/andp.201600006.

---

## Chapter 4 Growth and Simultaneous Valleys Manipulation of Two-Dimensional MoSe<sub>2</sub>-WSe<sub>2</sub> Lateral Heterostructure

### 4.1 Introduction:

Heterostructures (HSs) of three-dimensional (3D) materials with different energy gaps are the essential components of semiconductor technology [1-5]. The van der Waals equivalents, comprising of two-dimensional (2D) lattices like graphene, hexagonal boron nitride (h-BN) and transition metal dichalcogenides (TMDCs; MX<sub>2</sub>, where M = Mo, W and X = S, Se, Te), have emerged and showed great potential towards next-generation electronic devices [6-8]. The vertical HSs based on semiconducting MX<sub>2</sub> are of particular interest due to the ultrafast electron-hole separation between the two layers [9] of type-II band alignment [10], which renders them for many applications such as the solar cell [11] and p-n junction [12]. It also provides a platform for studying the emerging field of valleytronics [13]. The idea of valleytronics is to exploit the “valley degree of freedom”, which is a consequence of broken inversion symmetry together with non-vanishing spin-orbit coupling, while time-reversal symmetry is preserved so that the K and K' are no more equivalent [14]. These valleys (local band extrema) can be used for information storage and processing by selectively populating one of them [15].

In HS systems, a beautiful example of valleytronics is the vertical MoSe<sub>2</sub>-WSe<sub>2</sub> HS with a small twist angle, in which the two degenerate valleys at the K (K') point of each material nearly coincide in k space and give rise to an interlayer exciton having a long valley lifetime (40 ns) [13]. The covalently bonded monolayer MX<sub>2</sub> lateral HS systems are recently realized and could be explored for many interesting phenomena in fundamental physics and devices like in-plane p-n junctions [16]. Compared to the vertical case, in which the two layers can be stacked at any arbitrary orientation with respect to one another, the lateral HS among hexagonal lattices can either be formed at the zigzag or armchair direction. The valleys of each material marked by (K<sub>M</sub>, K'<sub>M</sub>) for MoSe<sub>2</sub> and (K<sub>W</sub>, K'<sub>W</sub>) for WSe<sub>2</sub>, respectively, in an ideal lateral HS case interact differently at the interface depending upon the in-plane orientation of the HS, as further discussed later. However, the interaction among the valleys is only limited to the very interface (ideally line), and the two constituents preserve their intrinsic properties at a few lattice constants away from the interface. A lateral HS sample with a very sharp interface therefore allows the exciting possibility of

---

simultaneous control of the four valleys across the interface provided the formation of intralayer HS excitons is insignificant.

From the perspective of synthesis, the vertical HS could be created by manual stacking of different materials using mechanical transfer [17], and also by a direct growth method [18, 19]. On the other hand, the lateral HS can only be created by direct growth. Recently, the lateral HSs between semi-metallic graphene and insulating h-BN as well as among different semiconducting monolayer TMDCs have been realized via a thermal chemical-vapor-deposition (CVD) method [19-21,16]. To achieve high-quality lateral TMDC HSs with a sharp interface, however, precise control over the amount of precursors is very important as further discussed later.

In this work, we present the growth of three-atom-thick lateral HS consisting of MoSe<sub>2</sub> and WSe<sub>2</sub> with a sharp interface by the pulsed-laser-deposition-assisted (PLD-assisted) selenization method [22]. Morphological characterizations including the optical microscope (OM), field emission scanning electron microscopy (FE-SEM), and atomic force microscopy (AFM) were initially carried out to examine the surface features and the thickness. The optical characteristics were studied by micro-Raman ( $\mu$ -Raman) and micro-photoluminescence ( $\mu$ -PL) spectroscopy. Interestingly, the PL acquired from the interface showed no sign of intermediate peaks arising from the intralayer HS excitons and/or formation of Mo<sub>x</sub>W<sub>(1-x)</sub>Se<sub>2</sub> alloys. This strongly implies the presence of a sharp interface, as also verified by scanning transmission electron microscopy (STEM). Furthermore, we performed the polarization-resolved PL characterization at low temperature (50 K) to study their relative valley polarization. The spatially separated four energy valleys (only intact at the interface) in k space were simultaneously manipulated by optical pumping. The parallel control of the four distinct valleys associated with two different materials (each one with a degenerate pair) by one input indicates the potential use of laterally sharp HSs in valley-based devices.

## **4.2 Experimental details:**

### **4.2.1 Synthesis**

The growth procedure for in-plane MoSe<sub>2</sub>-WSe<sub>2</sub> HS is schematically depicted in results and discussion section [Fig. 4-2 (a)]. Prior to the sample growth, thin films of MoO<sub>3</sub> and WO<sub>3</sub> were

---

precisely and selectively deposited by PLD at the specific locations on the SiO<sub>2</sub>/Si substrate using a shadow mask. Highly pure MoO<sub>3</sub> (WO<sub>3</sub>) targets were placed in a rotating target holder. The targets were initially exposed to high-energy (250 mJ) laser pulses from a KrF excimer laser (wavelength: 248 nm and pulse width: 20 ns) for a few minutes to remove the surface contaminants. The substrate was fixed, 10 cm above the target at 200°C. MoO<sub>3</sub> and WO<sub>3</sub> were deposited at laser energies 100 mJ and 120 mJ, respectively. The repetition rate and deposition time were 3 Hz and 60 s, respectively. The deposition was done at the base pressure ( $5 \times 10^{-7}$  Torr). No carrier gas was employed. The middle region of the sample was deliberately kept void for the HS growth.

To convert MoO<sub>3</sub> (WO<sub>3</sub>) into crystallized MoSe<sub>2</sub> (WSe<sub>2</sub>), the sample was then placed at the high-temperature zone (zone 2) of the two-zone hot wall furnace for the selenization process. Se powder was placed at the low-temperature zone (zone 1; 420 °C). The temperature of zone 2 was varied in three steps. In the first step, temperature was raised to 420 °C (30 °C min<sup>-1</sup>, 5 min) to create selenium vapors. In the second step, temperature was increased to 800°C (25 °C min<sup>-1</sup>) and was kept for sufficiently long time (25 min) to ensure the complete conversion of MoO<sub>3</sub> into crystallized MoSe<sub>2</sub>. Finally, as the evaporation temperature of WO<sub>3</sub> is higher, temperature was further increased to 950 °C (25 °C min<sup>-1</sup>) and was maintained for 10 min. WSe<sub>2</sub> grew at the edges of MoSe<sub>2</sub>, leading to the formation of in-plane MoSe<sub>2</sub>-WSe<sub>2</sub> HS. Maintaining chamber temperature at 800 °C for a long time greatly minimizes the tendency of tungsten (W) diffusion into MoSe<sub>2</sub> and molybdenum (Mo) diffusion into WSe<sub>2</sub>, thereby yielding laterally sharp HSs. Ar (10 sccm) and H<sub>2</sub> (3 sccm) were used as carrier gasses in the process. H<sub>2</sub> gas also assists in reducing MoO<sub>3</sub> (WO<sub>3</sub>) during the selenization process. The growth pressure was 450 mTorr. Monolayer lateral HS regions, where no vertical HSs were locally formed, were chosen for our experiments and analyses.

#### **4.2.2 STEM Imaging and EDS analysis:**

STEM samples were prepared by a method without using any polymer backing layer. Quantifoil holey carbon TEM grids were placed onto flakes on SiO<sub>2</sub>/Si substrate and a drop of isopropyl alcohol was dropped and dried. The SiO<sub>2</sub> layer was etched by 30% KOH solution for 4 hours and the TEM grids were detached from the substrate. Then TEM grids were rinsed several times in DI water and dried under the ambient condition. STEM imaging and EDS were performed by a Titan<sup>3</sup> G2 60-300 equipped with image and probe aberration correctors operated at 80 kV. The



---

convergence semi-angle was set to be  $\sim 25$  mrad. HAADF-STEM images were acquired from 80~200 mrad range.

#### **4.2.3 Experimental setup for polarization-sensitive PL measurements:**

The 633nm line from a He-Ne laser was used as an excitation source for the polarization-resolved photoluminescence (PL) measurements. The right (left) circularly polarized light, marked as  $\sigma^+$  ( $\sigma^-$ ) was focused onto the sample, using a  $\times 50$  objective lens, located in a cryostat, held at temperatures below 50K. The laser beam area on the sample was  $\sim 1\mu\text{m}^2$ . Either  $\sigma^+$  or  $\sigma^-$  polarized PL was selected and measured using a single-grating spectrometer with a focal length of 50 cm coupled to a liquid-nitrogen-cooled charge-couple device (CCD) detector. The linearly polarized incident light was reflected by a beam splitter and then passed through a quarter-wave plate, resulting in the circularly polarized light  $\sigma^+$  ( $\sigma^-$ ), as shown in Fig. 4-1. The PL signal went through the same quarter-wave plate. Either  $\sigma^+$  or  $\sigma^-$  polarized PL was selected by setting the linear polarizer #2 to either vertical or horizontal direction, respectively. In order to make sure that the linearly polarized light entering the spectrometer is the same polarization direction for both  $\sigma^+$  and  $\sigma^-$  polarized PL, we changed the half-wave plate setting appropriately; this is required because the efficiency of the detection system itself has some polarization dependence.

---

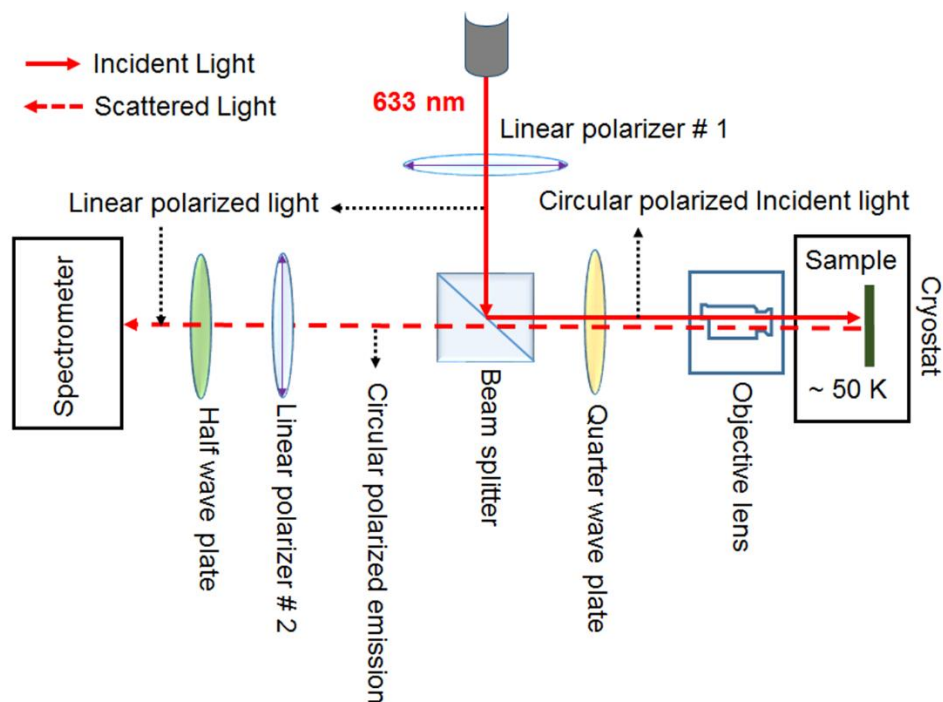


Figure 4- 1 Schematic illustration of the experimental setup for polarization-resolved PL measurements

### 4.3 Result and discussion:

The size of HS flakes formed over the substrate varied from  $\sim 15 \mu\text{m}$  to  $\sim 40 \mu\text{m}$ . The slightly different color contrast of  $\text{MoSe}_2$  and  $\text{WSe}_2$  on the substrate can be used for initial identification of the lateral HS flakes. The morphological inspection of an in-plane HS using OM and FE-SEM are shown in Fig. 4-1(b) and 1(c), respectively. The slightly dark inner triangle is  $\text{MoSe}_2$  surrounded by  $\text{WSe}_2$ . The inner and outer regions mostly exhibit uniform color contrast, indicating the HS flake is a monolayer, which was later directly confirmed by AFM. Localized irregular small grains over the flake in the OM image indicate the growth of the second  $\text{WSe}_2$  layer. We speculate that the growth kinetics essentially favours the monolayer; however, some defects in the first layer may act as nucleation sites for the growth of the second layer. The monolayer HS thickness was characterized by AFM. Fig. 4-2(d) shows the topographic image taken over the HS area shown in Fig. 4-2(b). The image revealed some grain boundaries (white color) within the outer  $\text{WSe}_2$  flake. However, the HS area (black dashed square in Fig. 4-2(d)) shows a uniform and flat surface with no significant variation in the thickness profile (blue line in Fig. 4-2(d)) except for noticeable

---

increase where the vertical HS locally formed. This essentially confirms the lateral growth of WSe<sub>2</sub> on the edges of MoSe<sub>2</sub>, resulting in the in-plane MoSe<sub>2</sub>-WSe<sub>2</sub> HS. The close matching between the lattice constants of MoSe<sub>2</sub> (0.3288 nm) and WSe<sub>2</sub> (0.3280 nm) is one of the reasons that favor the lateral growth [21]. The height of the MoSe<sub>2</sub>-WSe<sub>2</sub> HS was found to ~0.96 nm, confirming that the flake is indeed a monolayer. The interface cannot be observed in the topographic image due to the nearly identical thicknesses of MoSe<sub>2</sub> and WSe<sub>2</sub>. However, the AFM phase image in Fig. 4.2(e) taken from the highlighted region (black dashed square in Fig. 4-2(d)) clearly revealed the sharp and clean interface between inner triangular MoSe<sub>2</sub> and outer WSe<sub>2</sub>.

Furthermore, continuous film-like HS in some regions were formed at the centre of the sample beside the isolated monolayer lateral HS flakes and as shown in Fig. 4-3(b). The lateral HS flakes were mostly monolayer; however, some small irregular vertical HSs were also locally formed over the lateral HS flakes [Fig. 4-3 (c) and (d)].

A typical HS flake was further examined by  $\mu$ -Raman and  $\mu$ -PL spectroscopy with a 473-nm excitation source at room temperature. Fig. 4-4 (a) shows the OM image of the lateral HS flake used for Raman and PL characterizations. Here we carefully carried out the spectroscopic investigation over the monolayer regime, starting from point 1 through point 4, where no vertical HSs were locally formed. The Raman spectra acquired from point 1 and point 4 in Fig. 4-4 (a) showed typical A<sub>1g</sub> characteristics of WSe<sub>2</sub> (~251.8 cm<sup>-1</sup>) and MoSe<sub>2</sub> (~241.7 cm<sup>-1</sup>), respectively. The spectra acquired from the interface (point 2 and point 3) with a beam spot (~1  $\mu$ m<sup>2</sup>) showed two superimposed but distinguishable peaks at ~251.5 cm<sup>-1</sup> and ~243.6 cm<sup>-1</sup>, reasonably close to those for pristine WSe<sub>2</sub> and MoSe<sub>2</sub>, respectively, as depicted in Fig. 4-4(b). A similar behavior was also observed in the PL spectra. The PL acquired from the outer region (point 1) showed a single strong PL peak at ~786 nm (1.57 eV), and from the inner region (point 4) at ~816 nm (1.51 eV), showing typical A-excitonic transitions of pristine monolayer WSe<sub>2</sub> and MoSe<sub>2</sub>, respectively. On the other hand, when the laser spot was focused on the interface (point 2 and point 3 in Fig. 2(a)), such that it covers both MoSe<sub>2</sub> and WSe<sub>2</sub> regions, the resultant PL showed two superimposed but distinguishable peaks at ~789 nm (~1.57 eV) and 814 nm (~1.52 eV), still fairly close to direct A-excitonic transitions from pristine WSe<sub>2</sub> and MoSe<sub>2</sub>, respectively [Fig. 4-4 (c)].

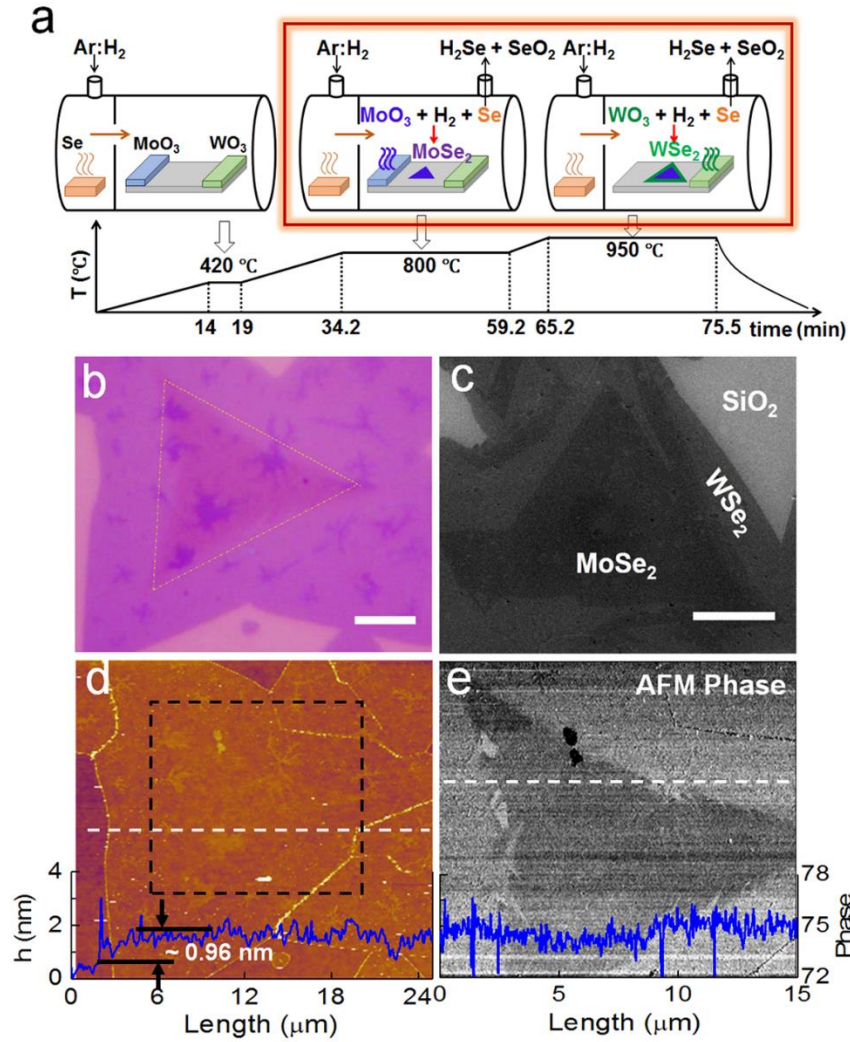


Figure 4- 2 Schematic representation of the experimental setup of the PLD-assisted growth mechanism for monolayer MoSe<sub>2</sub>-WSe<sub>2</sub> lateral HSs. (b) OM image of a lateral HS crystal on the SiO<sub>2</sub> substrate. The slightly dark inner triangle is MoSe<sub>2</sub> surrounded by WSe<sub>2</sub>. (c) FE-SEM image. (d) AFM topographic image taken over the HS flake in (b), showing a uniform thickness of 0.96 nm and confirming the monolayer nature of the lateral HS crystal. (e) AFM phase image taken over the black dashed square in (d), revealing the sharp and clean interface. The scale bar is 5  $\mu$ m.

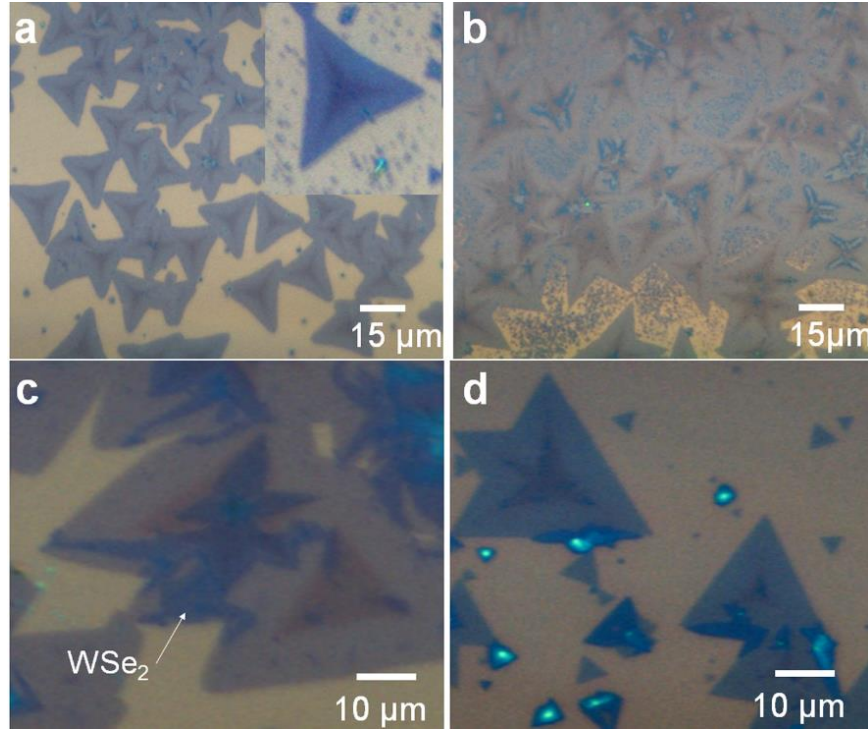


Figure 4- 3 OM images of in-plane MoSe<sub>2</sub>–WSe<sub>2</sub> lateral and vertical heterostructures grown by the pulsed-laser-deposition-assisted method. (a) Isolated flakes, (b) continuous film-like lateral HSs, and (c-d) irregular vertical HSs locally formed over the lateral HS flakes.

The observation of the two PL peaks at the interface in our PLD-assisted-grown lateral monolayer HS is distinct when compared with the PL features previously observed from single-step CVD-grown lateral HSs of MoSe<sub>2</sub>-WSe<sub>2</sub> [21] and MoS<sub>2</sub>-WS<sub>2</sub> [19]. In these cases, the PL spectra (also obtained with a beam size  $\sim 1 \mu\text{m}^2$ ) at the interface showed a single broad peak with an intermediate energy. Also, the peak position continuously shifted when the excitation beam was scanned from one region to the other across the interface. The most surprising observation was that the PL is brightest at the interface even if the beam spot covers much larger areas of the two constituting TMDC monolayers. This feature was attributed to the formation of intralayer HS excitons [19] or trapping of excitons by defects localized at the interface [21], which may be relevant to the formation of Mo<sub>x</sub>W<sub>(1-x)</sub>X<sub>2</sub> alloys. On the other hand, our PL results are in good agreement with those from a two-step CVD-grown lateral MoS<sub>2</sub>-WSe<sub>2</sub> HS having a very sharp interface [16]. Owing to the isolated growth chambers and large growth temperature difference between MoS<sub>2</sub> and WSe<sub>2</sub>, the two-step growth procedure presumably yielded the lateral HS with a much sharper

---

interface compared to the single-step growth mechanism, in which the possibility of  $\text{Mo}_x\text{W}_{(1-x)}\text{X}_2$  alloy formation near the interface region is comparatively high. The formation of alloys could also generate excitons having intermediate energies. Moreover, this exciton energy can fluctuate between the two extreme values for  $\text{MoX}_2$  and  $\text{WX}_2$ , depending upon the value of  $x$  ( $0 \leq x \leq 1$ ) [23]. In contrast, the distinct interfacial behaviors of our HS sample clearly indicates that the PLD-assisted selenization method is a useful approach for the growth of lateral HSs with sharp interfaces that significantly reduce the possibility of alloy formation and suppress the intralayer HS excitons and/or excitons bound to interfacial defects.

The lateral HS was also examined by PL and Raman mapping. The PL and Raman maps (both intensity and peak position) of the isolated HS flake are depicted in Fig. 4-4 (d-g). The maps clearly revealed the sharp interface between the inner monolayer  $\text{MoSe}_2$  and the outer monolayer  $\text{WSe}_2$ . No gradual variation of the peak position or increase in PL intensity was observed across the interface region, owing to the absence of the intermediate peak arising from alloys or intralayer excitonic transitions. The spectral feature was further confirmed by low-temperature  $\mu$ -PL spectroscopy. The PL scans at 50 K across the interface of the HS shown in Fig. 4-4(h) is depicted in Fig. 4-4(i). The PL peaks usually become sharper (decrease in full width at half maximum) and undergo blue shift in energy with decreasing temperature. The shift in the PL position with temperature can be explained by Varshni equation [24], which describes band gap ( $E_g$ ) as a function of temperature  $T$ . Again, the low-temperature  $\mu$ -PL from the interface region (point 2 and point 3) also showed two strong distinct peaks corresponding to pristine  $\text{MoSe}_2$  (1.59 eV) and  $\text{WSe}_2$  (1.69 eV) with no sign of the intermediate peak. The absence of the intermediate peak in the low-temperature PL spectra further supports the absence of intralayer HS excitonic matter and indicates the optically abrupt interface.

---



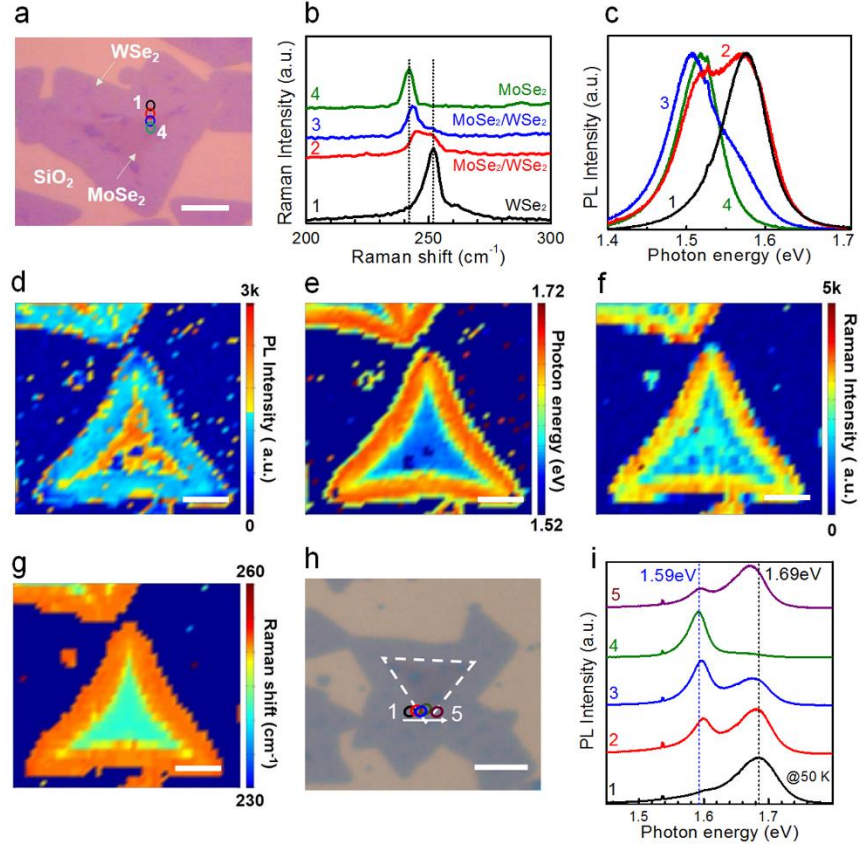


Figure 4- 4 Raman scattering and PL characterization of the lateral HS crystal. (a) OM image of the lateral HS flake used for room-temperature Raman and PL scans. (b) Raman spectra taken at four points across the HS interface in (a) display  $A_{1g}$  characteristics of MoSe<sub>2</sub> ( $\sim 241.7 \text{ cm}^{-1}$ ) and WSe<sub>2</sub> ( $\sim 251.8 \text{ cm}^{-1}$ ). (c) Room-temperature PL spectra acquired from the interface (point 2 and point 3 in (a) basically show the A-excitonic transitions of pristine MoSe<sub>2</sub> (1.51 eV) and WSe<sub>2</sub> (1.57 eV) without any complication arising from alloy states or interfacial effects. (d) PL intensity map. (e) PL position map. (f) Raman intensity map. (g) Raman shift map. The maps reveal the sharp interface of the lateral HS crystal. (h) OM image of the HS crystal used for low-temperature PL scan and (i) the corresponding low-temperature PL spectra taken at the five points at the triangular edge of the HS crystal in (h), showing the two PL peaks from each compound, which further supports the absence of alloys or intralayer excitonic matter. The scale bar is 10  $\mu\text{m}$ .

In order to observe the interface properties on a truly atomic scale, the interface of PLD-assisted-grown HS was further investigated by STEM. We employed HAADF (high angle annular dark field)-STEM imaging to probe the atomic structure of the lateral interface between WSe<sub>2</sub> and MoSe<sub>2</sub>. Using the EDS (energy dispersive X-ray spectroscopy) analysis, we first confirmed that two distinct areas are composed of WSe<sub>2</sub> and MoSe<sub>2</sub> (Fig. 4-5(a)). We note that there is the residual Au signal from the TEM grid. The zoom-in images of WSe<sub>2</sub> area show the honeycomb-like intensity patterns whereas the HAADF-STEM image of MoSe<sub>2</sub> is quite similar to the hexagonal pattern [16], as depicted in Fig. 4-5 (b) and (c), respectively. The intensity profiles along the armchair direction of two structures also show that the intensity of Mo is weaker than that of W as shown in Fig. 4-5 (d). Using the intensity difference at W and Mo locations, we can analyze the atomic distribution of W and Mo near the WSe<sub>2</sub>-MoSe<sub>2</sub> interface with atomic precision, as depicted in Fig. 4-5(e) and (f). The lateral interface exhibits that the crystal transition occurs sharply within ~2 nm. This observation is consistent with optical spectroscopic measurements.

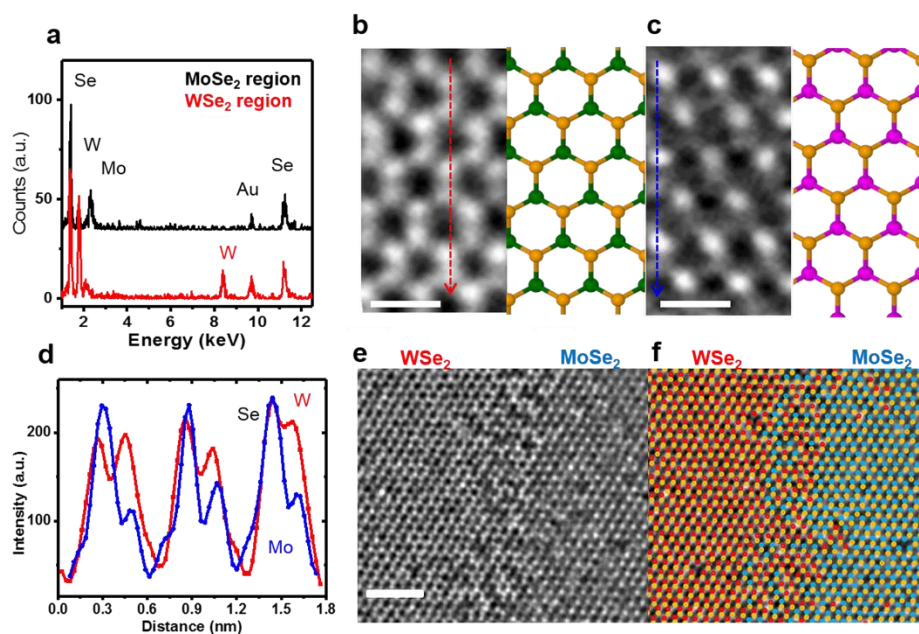


Figure 4- 5 Atomic resolution images of the WSe<sub>2</sub>-MoSe<sub>2</sub> lateral HS interface. (a) EDS spectra of WSe<sub>2</sub> and MoSe<sub>2</sub> regions. (b) Zoom-in HAADF-STEM image of WSe<sub>2</sub> with schematic modeling (yellow: Se, green: W) and (c) zoom-in HAADF-STEM image of MoSe<sub>2</sub> with schematic modeling (yellow: Se, pink: Mo). The scale bar is 0.5 nm. (d) Intensity line profiles of WSe<sub>2</sub> and MoSe<sub>2</sub> along



the dashed red line in panel (b) and the dashed blue line in panel (c). (e) HAADF-STEM image near the WSe<sub>2</sub>-MoSe<sub>2</sub> interface. (f) STEM image with atomic overlay. The scale bar is 2 nm.

Moreover, we were able to control the growth parameters to yield lateral HS flakes, showing a “gradual” interface extended over several micrometers. To grow such gradual HS (g-HS) flakes, the source materials (MoO<sub>3</sub> and WO<sub>3</sub>) were deposited with an increased laser energy (150 mJ) and a deposition time (120 s). In the selenization temperature profile, the intermediate step (800 °C for 25 min) was skipped and temperature was directly raised to 950 °C at the rate of 30 °C min<sup>-1</sup>; skipping this key step likely results in g-HS flakes having extended alloy interfaces. All other experimental conditions were same as discussed in Experimental Section. Fig. 4-6(a) shows the OM image (inset) and PL scan of the as-grown g-HS flake. The PL scan across the interface (six points in the Fig. 4-6(a) inset) of the g-HS sample clearly shows the gradual shift in the PL peak position from 1.57 eV (MoSe<sub>2</sub>) to 1.67 eV (WSe<sub>2</sub>). Fig. 4-6(b) plots the PL intensity mapping. The intermediate energy peak most likely comes from the alloy and the gradual shift in the PL peak position can be simply explained in term of  $x$  in Mo <sub>$x$</sub> W<sub>(1- $x$ )</sub>Se<sub>2</sub>, varying from 0 to 1 across the interface. The possibility of intralayer excitons, typically formed across the sharp interface after charge transfer, in the g-HS is therefore highly unlikely due to the presence of Mo <sub>$x$</sub> W<sub>(1- $x$ )</sub>Se<sub>2</sub> between pristine MoSe<sub>2</sub> and WSe<sub>2</sub>.

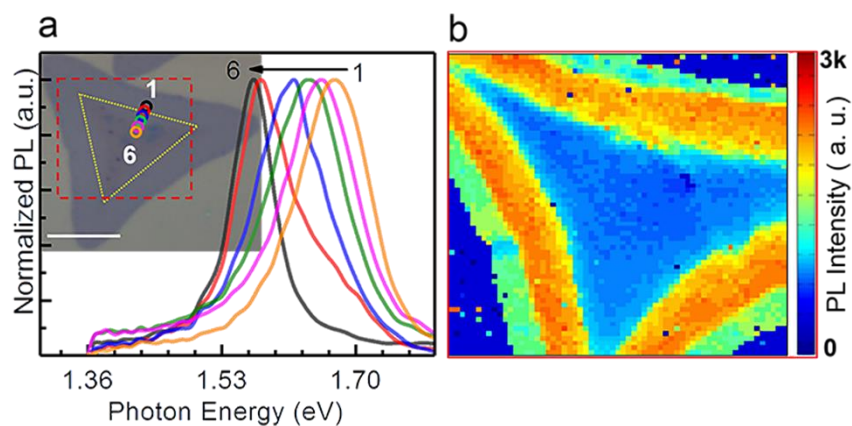


Figure 4- 6(a) OM image (inset) and PL scan of the lateral g-HS flake. The PL peak position gradually shifts from pristine MoSe<sub>2</sub> (point 1) to WSe<sub>2</sub> (point 6), indicating the extended alloy states across the interface. (b) PL intensity mapping taken over the red box in (a). The scale bar is 15  $\mu$ m.

---

Most importantly, the discrete nature of our HS flakes allows us to simultaneously control the two intact materials without any detrimental interface effect under optical excitation with a beam-spot size covering the interface. As a key example, we performed low-temperature polarization-resolved PL spectroscopy to demonstrate the potential use of our unique in-plane monolayer HS crystals in valleytronics. The semiconducting monolayer has two degenerate energy valleys at K (K') points of the first Brillouin zone [25]. The valley pseudo-spin of an exciton confined to one of these valleys can be coupled to the definite spin state of optical excitation. Therefore, circularly polarized light selectively excites one of the valleys and results in valley-polarized excitons [26]. In the vertical MoSe<sub>2</sub>-WSe<sub>2</sub> HS case stacked with a nearly 0° (or 60°) twist angle, the energy valleys of MoSe<sub>2</sub> [K<sub>M</sub> (K'<sub>M</sub>)] and WSe<sub>2</sub> [K<sub>W</sub> (K'<sub>W</sub>)] approximately coincide in momentum space and give rise to a long-lived interlayer exciton at 1.32 eV [13]. In our lateral case with no intermediate state, these valleys are isolated (only intact at the very interface) and show no significant effect on each another owing to the sharp separation of MoSe<sub>2</sub> and WSe<sub>2</sub>.

Fig. 4-7(a) and (b) schematically represent the two possible armchair and zigzag lateral HSs. The interface in these lateral HSs can be understood in terms of one dimensional (1D) lattice arising from the junction of two different 2D lattices. In the armchair case, the valleys of MoSe<sub>2</sub> at K<sub>M</sub> (K'<sub>M</sub>) and WSe<sub>2</sub> at K<sub>W</sub> (K'<sub>W</sub>) in k space will coincide at the same point on k<sub>y</sub> and could not be distinguished (grey points in Fig. 4-7(c)). However, in the zigzag case, K<sub>M</sub> coincide with K<sub>W</sub> while K'<sub>M</sub> coincide with K'<sub>W</sub> and therefore still K and K' can be distinguished (black and white points in Fig. 4-7(d)). In both cases, away from the interface line, the valleys of each constituent are well separated and can be manipulated simultaneously provided the crosstalk effects are negligible. These valleys can be selectively excited by circularly polarized optical pumping. The right (σ<sup>+</sup>) or left (σ<sup>-</sup>) handed circularly polarized light simultaneously excite (K<sub>M</sub>, K<sub>W</sub>) or (K'<sub>M</sub>, K'<sub>W</sub>) valleys, respectively [27]. The helicity of the resulting PL can be used to characterize the degree of valley polarization by selectively detecting the PL signal for both σ<sup>+</sup> and σ<sup>-</sup>. The degree of valley polarization is defined by  $\chi = [I(\sigma^+) - I(\sigma^-)]/[I(\sigma^+) + I(\sigma^-)]$ , where I(σ<sup>+</sup>) and I(σ<sup>-</sup>) are the intensities of right and left circularly polarized PL, respectively. In our measurements, the 633-nm line from a He-Ne laser was used as an excitation source. The detailed experimental setup for the polarization-resolved PL experiment at 50 K is given in Experimental section.

---

For example,  $\sigma^+$  polarization simultaneously excites the two  $K_M$  and  $K_W$  valleys separated in  $k$  space within the beam spot, resulting in the simultaneous valley polarization of both  $\text{MoSe}_2$  and  $\text{WSe}_2$ . The corresponding polarization-dependent PL spectra (Fig. 4-7(e)) exhibit clear emission peaks at  $\sim 1.6$  eV ( $\text{MoSe}_2$ ) and  $\sim 1.69$  eV ( $\text{WSe}_2$ ) without any complication arising from interfacial effects. The intensity of both peaks was simultaneously suppressed for  $\sigma^-$  polarization. This clearly shows that PL signals from both  $\text{MoSe}_2$  and  $\text{WSe}_2$  are highly  $\sigma^+$  polarized. The opposite behavior was observed for  $\sigma^-$  excitation (Fig. 4-7(f)). Fig. 4-7(g) plots the degree of polarization for both  $\sigma^+$  and  $\sigma^-$  excitation, clearly showing significant valley polarization with a slight asymmetry. The maximum polarizations for  $\text{MoSe}_2$  and  $\text{WSe}_2$  were found to be at their band edges. A significant valley polarization of  $\text{MoSe}_2$  is rather surprising because the compound is known to exhibit a poor valley efficiency even at 4 K. However, this can be understood in term of a motional narrowing effect in our high-excitation scheme, i.e. if the exciton density increases, the elastic scattering time decreases. This in turn increases the spin/valley relaxation time, which induces a large valley polarization.<sup>28</sup> The slightly higher valley polarization for  $\text{WSe}_2$  can be understood in terms of the proximity effect, that is, the corresponding PL position is closer to the excitation energy.

The room-temperature valley polarization at each position i.e.  $\text{MoSe}_2$ ,  $\text{WSe}_2$  and  $\text{MoSe}_2/\text{WSe}_2$  was found to be approximately zero (Fig. 4-8), indicating that at high temperatures phonon scattering<sup>29</sup> and long-range exchange Coulomb interaction<sup>30</sup> cause stronger valley dephasing and consequently the steady state PL polarization vanishes. This shows that temperature is an important parameter in maintaining the valleytronic efficiency.

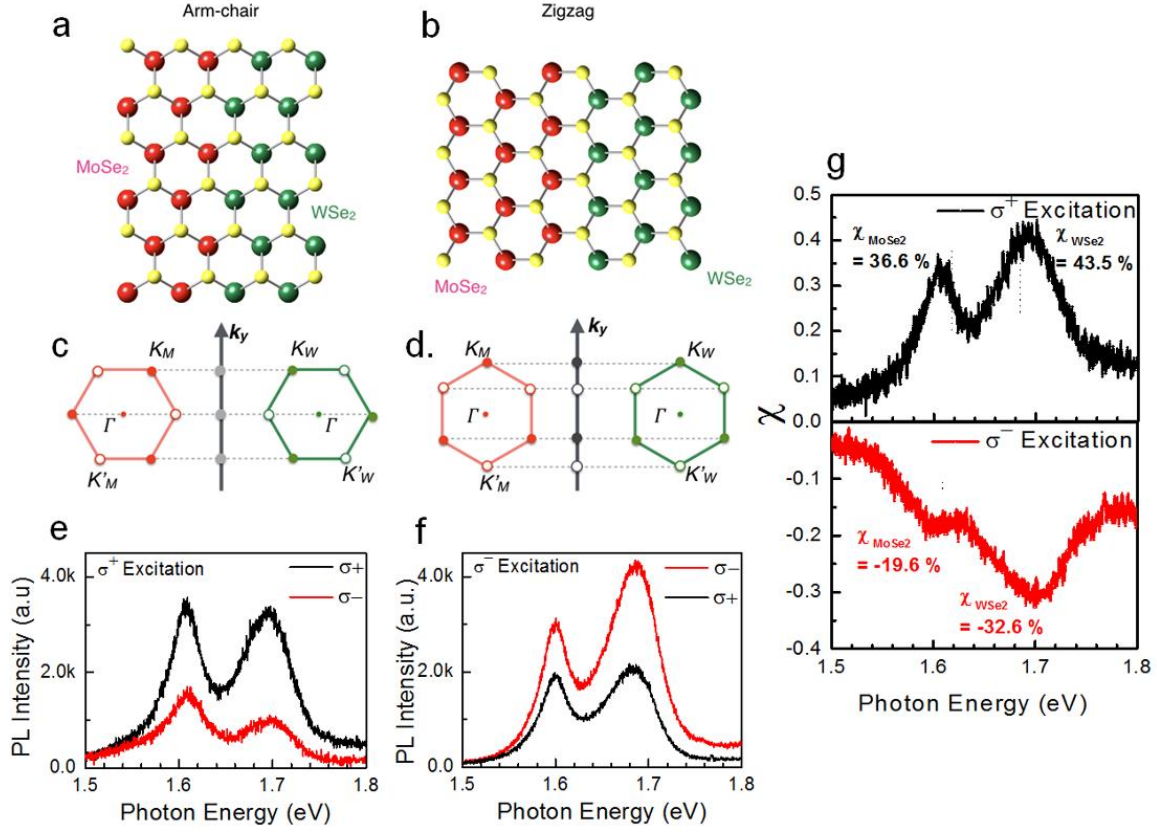


Figure 4- 7 Crystal structures of the monolayer MoSe<sub>2</sub>-WSe<sub>2</sub> lateral HS formed at (a) armchair and (b) zigzag directions. Schematics of their Brillouin zones in k space for (c) armchair and (d) zigzag cases, respectively. Polarization-resolved PL spectra measured at 50 K for (e)  $\sigma^+$  and (f)  $\sigma^-$  excitation, respectively. (g) Degree of polarization ( $\chi$ ) as a function of emission energy calculated from the PL spectra in (e) and (f).

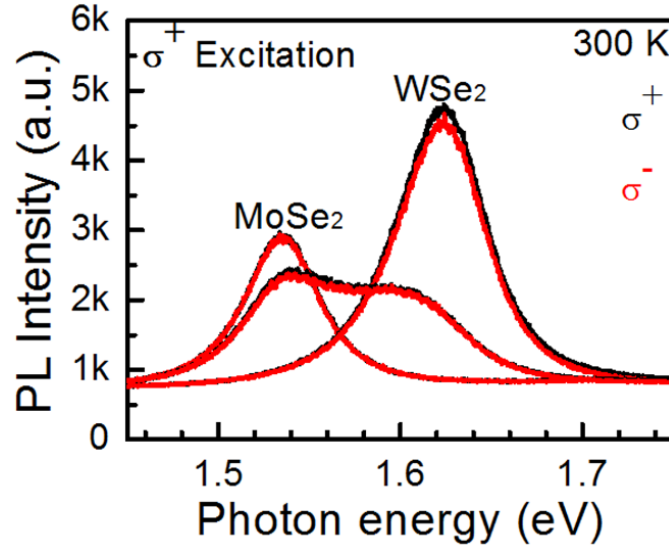


Figure 4- 8 Polarization-sensitive PL measurements on pristine MoSe<sub>2</sub>, WSe<sub>2</sub> and the interface MoSe<sub>2</sub>-WSe<sub>2</sub> regions of the lateral HS at room temperature, signifying no essential valley polarization.

#### 4.4 Chapter summary:

In summary, we have presented a simple PLD-assisted selenization method for growing high-quality monolayer MoSe<sub>2</sub>-WSe<sub>2</sub> lateral HS on the Si/SiO<sub>2</sub> substrate. Morphological and optical characterizations confirmed that the as-grown HS flakes are monolayer with excellent interface and optical properties. The absence of any intermediate peak in the PL spectra across the interface also indicates the sharp interface, also confirmed by STEM. This sharpness of the lateral HS uniquely allowed us to simultaneously manipulate the four Dirac valleys associated with the two different materials. The polarization-resolved PL results at 50 K showed that significant valley polarization of 36.6 (-19.6) % and 43.5 (-32.6) % can be simultaneously achieved with a single optical beam for MoSe<sub>2</sub> and WSe<sub>2</sub> under  $\sigma^+$  ( $\sigma^-$ ) excitation, respectively. We emphasize that this multitasking cannot be realized in any lateral HS that are influenced by significant interfacial effects, which in turn strongly disturb the profound valley physics at the symmetry-breaking boundary of the two constituting TMDCs. We believe that laterally grown TMDC HSs by our PLD-assisted method are potentially important for advancing 2D valleytronics, especially when the photon excitation energy can be actively tuned to the band edge of consisting TMDCs.

---

## 4.5 References

- [1]. Roblin, P.; Rohdin, H. High-Speed Heterostructure Devices: from Device Concepts to Circuit Modeling. Cambridge University Press: **2002**.
- [2] Zhang, X. M.; Lu, M. Y.; Zhang, Y.; Chen, L. J.; Wang, Z. L., Adv. Mater. **2009**, 21, 2767-2770.
- [3] Morkoc, H.; Mohammad, S. N. , Science **1995**, 267, 51-55.
- [4] Matsuo, S.; Shinya, A.; Kakitsuka, T.; Nozaki, K.; Segawa, T.; Sato, T.; Kawaguchi, Y.; Notomi, M., Nat. Photon. **2010**, 4, 648-654..
- [5] Xiang, J.; Lu, W.; Hu, Y.; Wu, Y.; Yan, H.; Lieber, C. M., Nature **2006**, 441, 489-493.
- [6] Roy, T.; Tosun, M.; Kang, J. S.; Sachid, A. B.; Desai, S. B.; Hettick, M.; Hu, C. C.; Javey, A., ACS Nano **2014**, 8, 6259-6264.
- [7] Bertolazzi, S.; Krasnozhon, D.; Kis, A, ACS Nano **2013**, 7, 3246-3252.
- [8] Lee, G.H.; Yu, Y.J.; Cui, X.; Petrone, N.; Lee, C.H.; Choi, M. S.; Lee, D.-Y.; Lee, C.; Yoo, W. J.; Watanabe, K., ACS Nano **2013**, 7, 7931-7936.
- [9] Hong, X.; Kim, J.; Shi, S.F.; Zhang, Y.; Jin, C.; Sun, Y.; Tongay, S.; Wu, J. Zhang, Y.; Wang, F. , Nat. Nanotechnol. **2014**, 9, 682-686.
- [10] Hill, H. M.; Rigosi, A. F.; Rim, K. T.; Flynn, G. W.; Heinz, T. F. , Nano Lett. **2016**, 16, 4831-4837.
- [11] Furchi, M. M.; Pospischil, A.; Libisch, F.; Burgdörfer, J.; Mueller, T. , Nano Lett. **2014**, 14, 4785-4791.
- [12] Lee, C.H.; Lee, G.-H.; Van Der Zande, A. M.; Chen, W.; Li, Y.; Han, M.; Cui, X.; Arefe, G.; Nuckolls, C.; Heinz, T. F. , Nat. Nanotechnol. **2014**, 9, 676-681.
- [13] Rivera, P.; Seyler, K. L.; Yu, H.; Schaibley, J. R.; Yan, J.; Mandrus, D. G.; Yao, W.; Xu, X. , Science **2016**, 351, 688-691.
- [14] Xiao, D.; Liu, G.B.; Feng, W.; Xu, X.; Yao, W. , Phys. Rev. Lett. 2012, **108**,196802-5.
- [15] Ye, Y.; Xiao, J.; Wang, H.; Ye, Z.; Zhu, H.; Zhao, M.; Wang, Y.; Zhao, J.; Yin, X.; Zhang, X. , Nat. Nanotechnol. **2016**, 11,598-602.
- [16] Li, M.-Y.; Shi, Y.; Cheng, C.C; Lu, L.S; Lin, Y.C.; Tang, H.L.; Tsai, M.L.; Chu, Wei, K.H.; He, J.H. , Science **2015**, 349, 524-528.

- 
- [17] Geim, A. K.; Grigorieva, I. V. ,Nature **2013**, 499, 419-425.
- [18] Samad, L.; Bladow, S. M.; Ding, Q.; Zhuo, J.; Jacobberger, R. M.; Arnold, M. S.; Jin, S. , ACS Nano **2016**, 10, 7039-7046.
- [19] Gong, Y.; Lin, J.; Wang, X.; Shi, G.; Lei, S.; Lin, Z.; Zou, X.; Ye, G.; Vajtai, R.; Yakobson, B. I. , Nat. Mater. **2014**, 13, 1135-1142.
- [20] Han, G. H.; Rodríguez-Manzo, J. A.; Lee, C.-W.; Kybert, N. J.; Lerner, M. B.; Qi, Z. J.; Dattoli, E. N.; Rappe, A. M.; Drndic, M. Johnson, A. C., ACS Nano **2013**, 7, 10129-10138.
- [21] Huang, C.; Wu, S.; Sanchez, A. M.; Peters, J. J.; Beanland, R.; Ross, J. S.; Rivera, P.; Yao, W.; Cobden, D. H.; Xu, X. , Nat. Mater. **2014**, 13, 1096-1101.
- [22] Ullah, F.; Nguyen, T. K.; Le, C. T.; Kim, Y. S, CrystEngComm. 2016, **18**, 6992-6996.
- [23] Zhang, W.; Li, X.; Jiang, T.; Song, J.; Lin, Y.; Zhu, L.; Xu, X. Nanoscale **2015**, 7, 13554-13560.
- [24] Varshni, Y. P. Physica **1967**, 34, 149-154.
- [25] Mak, K. F.; Lee, C.; Hone, J.; Shan, J.; Heinz, T. F. Phys. Rev. Lett. **2010**, 105, 136805-4.
- [26] Mak, K. F.; He, K.; Shan, J.; Heinz, T. F. Nat. Nanotechnol. **2012**, 7, 494-498.
- [27] Yao, W.; Xiao, D.; Niu, Q. Phys. Rev. B **2008**, 77, 235406-6.
- [28] Wang, G; Palleau, E; Amand, T; Tongay, S; Marie, X; Urbaszek, B. Appl. Phys. Lett. **2015**, 106, 112101-4.
- [29] Zeng, H; Dai, J; Yao, W; Xiao, D; Cui, X. Nat. Nanotechnol. **2012**, 7, 490-493.
- [30] Schaibley, J. R.; Yu, H.; Clark, G.; Rivera, P.; Ross, J. S.; Seyler, K. L.; Yao, W.; Xu, X. Nat. Rev. Mater. **2016**, 1, 16055.



---

## Chapter 5 Initial Results: Exciton Transport in Monolayer WS<sub>2</sub> Stripes

### 5.1 Introduction:

Charge carriers in a magnetic field, applied perpendicular to the direction of current, essentially develops a potential difference perpendicular to the direction of current and magnetic field. This phenomenon is famously known as Hall Effect (HE). The HE set the fundamentals of many practical applications and devices [1-2]. Even today, Hall effect is indeed one of the most fundamental measurement to characterize the transport properties of semiconductors and metals [3]. Recently, another interesting phenomenon, namely valley Hall effect (VHE), which originates from the geometric phase (Berry phase) in solids gained tremendous attention owing to its potential application in valleytronics devices [4-5]. The VHE is essentially driven by Berry curvature  $\Omega(k)$  of Bloch bands serving as internal magnetic field. The  $\Omega(k)$  induce a contrasting transverse component in the traverse velocity. The transverse velocity have opposite direction for positive and negative charge carriers in the presence of electric field [6]. Consequently, the opposite charge carriers accumulate on the two opposite sides of the sample. This new fascinating set the foundation for the so called valleytronics devices [5].

Primarily, the conventional HE and VHE driven by external magnetic field and Berry curvature, respectively, are observed for single charged particles [1, 5]. However, a composite particle, such as exciton, carrying quantum degree of freedom could also be exploited. Exciton is one of the simplest composite particle comprised of electron hole pair bounded by Coulomb interaction. The excitons plays a major role in defining the optical properties of semiconductors [7-8]. The Hall effect for composite particles was initially theoretically predicted, and recently observed in monolayer MoS<sub>2</sub> system [9-11]. Similar to VHE, the Berry curvature of exciton also induce transverse component in exciton traverse velocity leading to exciton Hall effect (EHE). However, unlike both VHE and HE, in which the opposite charge carriers are driven in opposite directions by applied electric field, the EHE utilize statistical forces and/or chemical potential to drive the exciton in a traverse direction. Once the excitons gain some definite traverse velocity by any mean, the Berry curvature can play its role to induce the transverse component of velocity. Moreover, the EHE cannot be realized in materials which possess only one type of excitons (no valley degree of freedom) owing to their indistinguishable and electrically neutral character.



---

The direct band gap in the visible spectrum of monolayer  $\text{MX}_2$  make them a potential setting for the observation of EHE. The  $\text{MX}_2$  possesses stable exciton having giant binding energies owing to their intrinsic 2D nature. Moreover, the broken inversion symmetry together with time reversal symmetry results in two degenerate but inequivalent energy valleys at  $K$  and  $K'$  points  $k$ -space. The spin and valleys are coupled in  $\text{MX}_2$ , and hence gives rise to the valley degree of freedom. The time reversal symmetry dictates that the Berry curvature must have contrasting effect at  $K$  and  $K'$  valleys. The contrasting Berry curvature at the two valleys act as contrasting magnetic field. Interestingly, the valley excitons in these systems also carry the valley degree of freedom. Moreover, the  $\text{MX}_2$  have high quantum efficiency in monolayer regime rendering them an ideal material for studying the exciton transport properties.

Here, we study the exciton transport in monolayer  $\text{WS}_2$  stripes of various widths. The stripes of different width were prepared to locally manipulate the chemical potential. The chemical potential is responsible for the transport of exciton in a specific direction. Initially, high quality monolayer triangular flakes were grown by CVD method. Morphological and optical characterizations including optical microscope (OM), atomic force microscopy (AFM), Raman and photoluminescence (PL) characterization were carried out to examine the flake quality and thickness. The flakes were then trimmed into stripes of various widths *via* laser. The exciton diffusion through the stripes was examined by spatially and polarization resolved spectroscopy (SAPRS) at low temperature. The SAPRS results shows that valley excitons originating from  $K$  and  $K'$  valleys tends to move in opposite transverse direction showing the signal of EHE. Moreover, the diffusion length of exciton was found to be inversely proportional to the width of the stripe.

## **5.2 Experimental details:**

The experimental details regarding the growth and basic characterization of monolayer  $\text{WS}_2$  triangular flakes is given below.

### **5.2.1 Monolayer $\text{WS}_2$ growth:**

---

The schematic diagram of CVD is shown in Fig.1.5 (See chapter 1). Initially, very small amount (~0.10 g) of tungsten oxide ( $\text{WO}_3$ ) powder was placed in high temperature zone (zone 1) in graphite crucible. Sulfur powder (~1 g) was placed in low temperature zone (zone 2) in a separate graphite crucible. Si/SiO<sub>2</sub> was placed upside down on  $\text{WO}_3$  powder. The system was evacuated to the base pressure value (1 mTorr) using a rotary pump, and then subsequently flashed with  $\text{N}_2$  gas for few times to remove the oxygen species.  $\text{N}_2$  gas with 100 sccm of flow rate was inserted into the chamber to create the initial growth pressure of 300 torr. The temperature of the system were raised to the specified value in two steps. In the first step, the temperatures of zone 1 and 2 were simultaneously raised 450 oC and 200 oC, respectively and were maintained for 5 mint. In the second step, the temperatures of the two zones were further increased to 900 oC (zone 1) and 350 oC (zone 2) respectively to grow monolayer  $\text{WS}_2$  flakes. Right before the second phase the exhaust gas valve was closed and  $\text{N}_2$  gas was set to 10 sccm to slowly increase the chamber pressure. A total 10 min of reaction time was given. After the reaction, the chamber was naturally cool down the room temperature and the sample was taken out.

### 5.2.2 Characterization

The CVD grown monolayer  $\text{WS}_2$  flakes were examined by OM,  $\mu$ -Raman and  $\mu$ -PL (Dongwoo, 473 nm excitation source) and AFM ( $k \sim 1.8$  N/m, 0.5 Hz scan speed).

## 5.3 Result and discussion

Briefly, an exciton, a bound electron hole pair is generated in the lattice upon the absorption of high energy photon compared to the band gap of the material. A stable exciton possesses higher binding energy compared to the Boltzman energy so that it can withstand against the odds of phonon. Intriguingly, the valleys excitons of monolayer  $\text{MX}_2$  are stable and possesses giant binding energies. These excellent properties of  $\text{MX}_2$  renders them ideal platform to study the exciton transport under Berry curvature.

Initially, we comparatively describes the VHE and EHE, as schematically shown in Fig. 1(a) and 1(b), respectively. The VHE involves external electric field to drive the electron and hole in the longitudinal direction. However, since electron and hole carry equivalent but opposite charges, therefore, the electric force push them in opposite longitudinal direction. The opposite electric force essentially results in the disassociation of the electron hole pair. Moreover, the opposite charges

than gain the transverse component of velocity, also called anomalous velocity, in opposite transverse direction owing to the non-zero Berry curvature arising from Berry phase in  $\text{MX}_2$  system [Fig. 5.1 (a)]. On the other hand, the electron hole pair can be driven in same direction by using statistical forces arising from temperature and/or chemical potential difference. A laser illumination at a point creates maximum excitons at the excitation point, and hence a chemical potential is locally created which serves as driving force for the exciton. For instance, if a  $\text{MX}_2$  flake with rectangular geometry with small width is illuminated at the edge than the exciton will naturally move towards the other edge (longitudinal direction). Once the exciton gain longitudinal velocity, then the excitons of  $K$  and  $K'$  valleys moves in contrasting transverse direction due to the opposite sign of Berry curvature on the two respective valleys. The separation of  $K$  and  $K'$  exciton leads to EHE. The transverse component of velocity can be understood in terms of equation of motion with Berry phase

$$v = \frac{1}{\hbar} \frac{dE_n(k)}{dk} - k \times \Omega_n(k)$$

Here,  $v$  is velocity,  $\hbar$  is plank constant,  $E_n$  energy and  $\Omega_n(k)$  is Berry curvature in  $k$ -space. For a non-zero Berry curvature, either space inversion symmetry (I) or time reversal symmetry (T) must be broken. If a system have both T and I symmetries than these, two commute with each other and the net Berry curvature is zero.

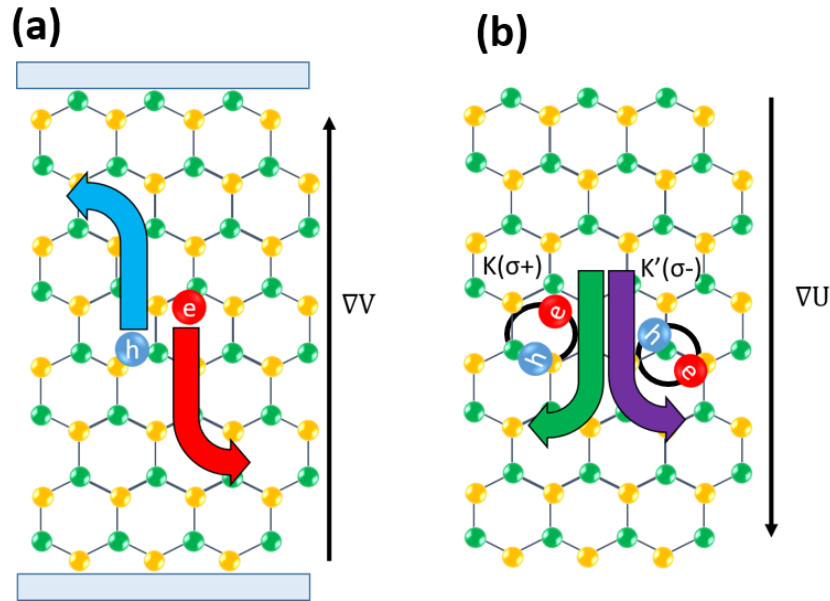


Figure 5- 1(a) Schematic illustration of Valley Hall effect and (b) Exciton Hall effect.

To study the exciton transport in WS<sub>2</sub> stripes, we grow high quality monolayer WS<sub>2</sub> triangular flakes by using thermal CVD method. The OM image of WS<sub>2</sub> is depicted in Fig. 5.2 (a). The surface features of the flake were examined by AFM. The topography image shows a clean surface with very few white spots, indicating the dust particles [Fig. 5.2 (b)]. The thickness of the flake is about ~ 1 nm, confirming the WS<sub>2</sub> in indeed monolayer. The clean surface could also be observed in the AFM phase image, as shown in Fig. 5.2 (c). The flake quality was further verified by  $\mu$ -Raman and  $\mu$ -PL spectroscopy. The Raman spectra of WS<sub>2</sub>, acquired with 473 nm excitation source and 1  $\mu$ m spot size, shows two prominent peaks at 358.41 cm<sup>-1</sup> and 417.42 cm<sup>-1</sup> corresponding to in-plane (E<sub>2g</sub><sup>1</sup>) and out of plane (A<sub>1g</sub>) vibrational modes. The peak separation ( $\Delta\omega$ ) between the two peaks strongly depends on the number of layers. In our WS<sub>2</sub>, the  $\Delta\omega$  was found to be ~59 cm<sup>-1</sup>, which is corresponding monolayer. Another hallmark of good quality is its PL properties. Our CVD grown monolayer WS<sub>2</sub> show a strong PL signal at ~635 nm (1.95 eV) corresponding to direct A-exciton arising from the K point of 1<sup>st</sup> hexagonal Brillouin zone. The morphological and optical characterizations results conclusively confirm the excellent quality of film.

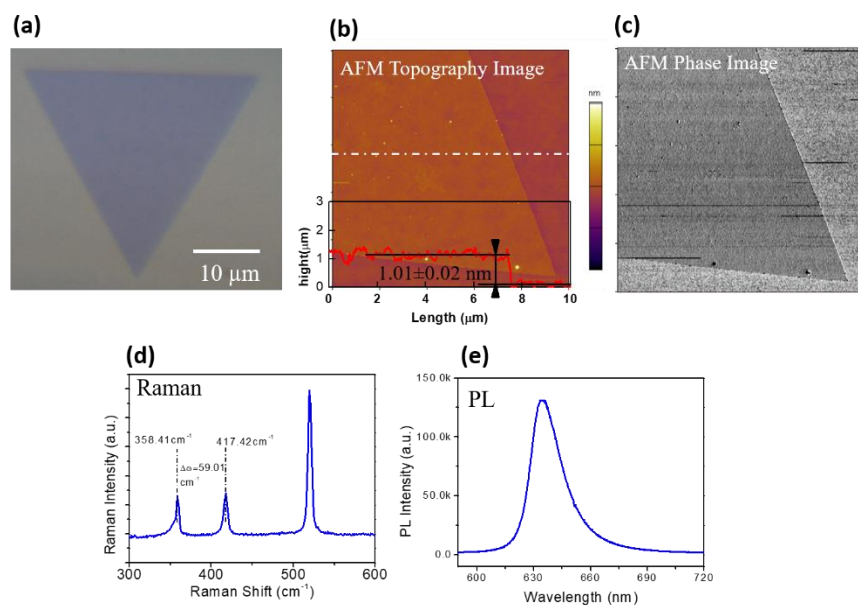


Figure 5- 2 (a) Optical microscope (b) AFM topography and (c) AFM phase image of monolayer WS<sub>2</sub>. (c) Raman and (d) PL spectra of WS<sub>2</sub>.

The monolayer flake was then trimmed into the stripes of various widths by using 473 nm laser

---

with relatively high energy ( $\sim 30$  mW), as shown in Fig. 5.3 (a). The spot size was 1 micron. The idea behind creating the stripes was to locally manipulate the chemical potential and direct the excitons transport in a specific direction. Naturally, the exciton scatters and move radially outwards in all direction from higher density to lower density region. Since we could not drive the electrically neutral exciton in a specific direction by using electric force, therefore, the design  $\text{MX}_2$  flakes of particular geometry is essential. This can be simply understood in terms of water pipes, in which water flow is directed to specific locations from a water tank.

Moreover, the diffusion length of excitons with respect to widths of the  $\text{WS}_2$  stripes was examined. The stripes were excited at the edges with 632 nm excitation source. The diffusion was monitored by acquiring PL signal away (+ve  $x$ -direction) from the excitation point by using specially resolved PL spectroscopy. Interestingly, the diffusion length of excitons was found be inversely proportional to the width of the stripe. The diffusion length in the three stripes in Fig. 5.3 (a) of widths  $\sim 1$   $\mu\text{m}$ ,  $\sim 2$   $\mu\text{m}$  and  $\sim 5$   $\mu\text{m}$  was found 0.0664, 0.0597 and 0.0521, respectively. This shows that the exciton having specific density can travel long distance in small stripes.

Furthermore, the effect of Berry curvature, which induce transverse component of velocity, was examined by acquiring PL signal along  $y$ -axis at fixed value of  $x$ -axis. Berry Curvature (effective magnetic field) acts on opposite direction on the two respective  $K$  and  $K'$  valleys and therefore, the excitons of  $K$  and  $K'$  valleys drifts in opposite direction, as shown in Fig. 5.3(b). Moreover, the excitons of  $K(K')$  emits right hand circular  $\sigma^+$  (left hand circular  $\sigma^-$ ) photon, respectively. Therefore, the drifting of  $K$  and  $K'$  exciton can be monitored by selectively acquiring  $\sigma^+$  and  $\sigma^-$  PL signal along  $y$ -axis for  $\sigma^+$  and  $\sigma^-$  excitations, respectively [Fig. 5.3(b)]. In our experiments, although the  $\sim 1$   $\mu\text{m}$  and  $\sim 2$   $\mu\text{m}$  stripes, which show relatively long diffusion, however, didn't show any separation of  $\sigma^+$  and  $\sigma^-$  PL along  $y$ -axis. On the other hand, stripe of width  $\sim 5$   $\mu\text{m}$  showed separation  $\sigma^+$  and  $\sigma^-$  PL along  $y$ -axis, as shown Fig. 5.3 (c) and (d). For  $\sigma^+$  excitation, the  $\sigma^+$  PL signal along -ve  $y$ -axis was found to be higher compared to  $\sigma^-$  PL and for  $\sigma^-$  excitation, the  $\sigma^-$  PL signal along +ve  $y$ -axis was found to be higher compared to  $\sigma^+$  PL signal. This clearly indicates the drift of  $K$  and  $K'$  excitons in opposite directions and show a signal of EHE. Moreover, this observation shows that a stripe should have reasonable width, so that the  $K$  and  $K'$  excitons could have enough space to separate within the flake. However, if the width is too long than the exciton will scatters in all direction and EHE could not be detected, as schematically shown by arrows in

Fig 5.3 (a).

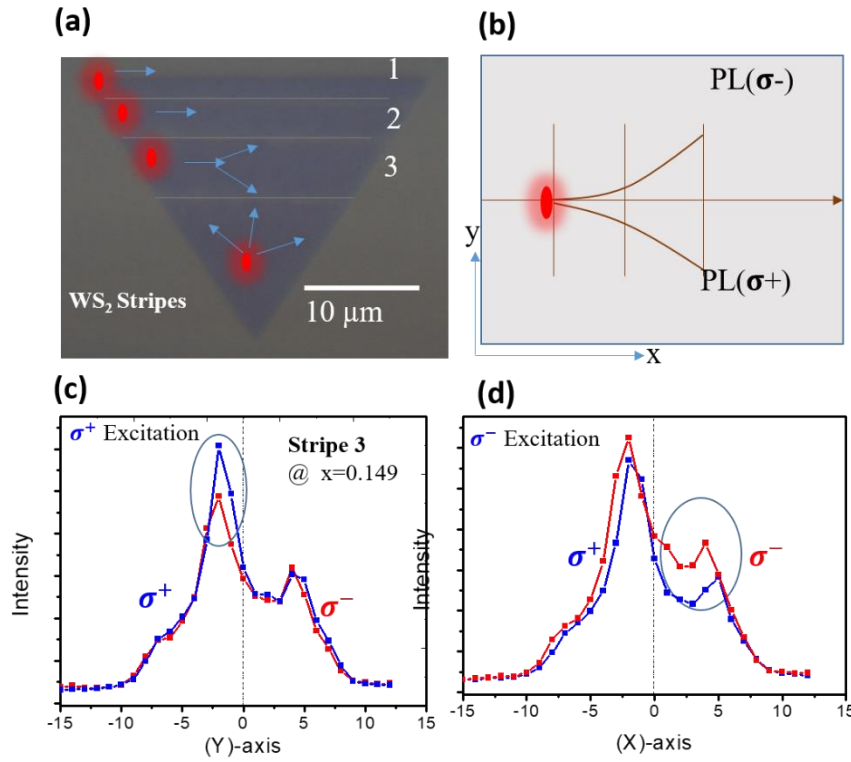


Figure 5- 3(a) Optical microscope image of WS<sub>2</sub> stripes with various widths (b) schematic illustration of K and K' excitons transport in monolayer WS<sub>2</sub>. K and K' excitons emits  $\sigma^+$  and  $\sigma^-$  photons respectively. Spatially and polarization resolved PL spectra acquired from stripe 3 for  $\sigma^+$  and  $\sigma^-$  excitation

#### 5.4 Chapter summary:

We examine the transport of electrically neutral composite particles, namely exciton, within WS<sub>2</sub> stripes. Monolayer WS<sub>2</sub> flakes were grown by conventional CVD method and the flake quality was verified by morphological and optical characterizations. Stipes of various widths were prepared by trimming the flake into rectangular flakes by using high-energy laser. The spatially resolved PL results confirms that the diffusion of exciton within a WS<sub>2</sub> flake strongly depends on the width of the stripe. The SAPRS measurements shows that *K* and *K'* excitons accumulate on the opposite edges of the sample, showing a signal of EHE. Here, we want to emphasize that the width plays an

---

important role in detecting EHE, because if the width of the stripe is too small than the  $K$  and  $K'$  exciton would not have enough space to separate within the flake, however, if it is too wide than the exciton would scatters.

## 5.5 References

1. Van der Pauw, L. *Philips research reports* **1958**, 13, 1-9.
2. Kato, Y. K.; Myers, R. C.; Gossard, A. C.; Awschalom, D. D. *science* **2004**, 306, (5703), 1910-1913.
3. Neubauer, A.; Pfleiderer, C.; Binz, B.; Rosch, A.; Ritz, R.; Niklowitz, P.; Böni, P. *Physical review letters* **2009**, 102, (18), 186602.
4. Zhang, Y.; Tan, Y.-W.; Stormer, H. L.; Kim, P. *nature* **2005**, 438, (7065), 201.
5. Mak, K. F.; McGill, K. L.; Park, J.; McEuen, P. L. *Science* **2014**, 344, (6191), 1489-1492.
6. Xu, X.; Yao, W.; Xiao, D.; Heinz, T. F. *Nature Physics* **2014**, 10, (5), 343.
7. Qiu, D. Y.; Felipe, H.; Louie, S. G. *Physical review letters* **2013**, 111, (21), 216805.
8. Shi, H.; Yan, R.; Bertolazzi, S.; Brivio, J.; Gao, B.; Kis, A.; Jena, D.; Xing, H. G.; Huang, L. *ACS nano* **2013**, 7, (2), 1072-1080.
9. Li, Y.-M.; Li, J.; Shi, L.-K.; Zhang, D.; Yang, W.; Chang, K. *Physical review letters* **2015**, 115, (16), 166804.
10. Yao, W.; Niu, Q. *Physical review letters* **2008**, 101, (10), 106401.
11. Onga, M.; Zhang, Y.; Ideue, T.; Iwasa, Y. *Nature Materials* **2017**, 16, 1193.

---

## Conclusion

The research interest on the intrinsic 2D systems, particularly TMDC, are constantly increasing owing to their fascinating properties useful in terms of both fundamental understanding and device applications. Most of the studies done on TMDC are on micrometer size monolayer flakes acquired by mechanical cleavage method from a bulk crystal. Though mechanical cleavage method using scotch tape can produce good quality flakes, however, this method cannot be used beyond fundamental studies. Currently, one of the main concern regarding TMDC is to develop a reliable growth mechanism which can produce high quality and yet large area continuous monolayer films. In this regard, CVD is a useful method which can produce monolayer flakes of reasonable quality with size ranging from few micrometer to few hundreds micrometer. CVD can sometime produce a continuous film, however, the grain boundaries in the continuous film significantly reduce the mobility of the film. On the other hand, PVD methods generally offers large area amorphous films.

In this study, we combine the PVD method with conventional CVD to achieve few and mono layers film of MoS<sub>2</sub> and MoSe<sub>2</sub> respectively. Few layers large area (2 x 2 cm<sup>2</sup>) film was achieved by depositing a very thin layer of amorphous MoS<sub>2</sub> on sapphire substrate. Though the Hall measurement revealed the continuity of the film but the Raman and PL spectroscopy results clearly showed its poor crystalline nature. To improve the crystal quality of the film, the sample was annealed in a two zone CVD chamber in sulfur rich environment. This step greatly enhanced the film quality while maintained continuity, as verified by Raman, PL and Hall measurements.

The synthesis of Se compounds are difficult compared to the S compounds owing to the lower reactivity of Se. However, we were able to acquire excellent quality monolayer MoSe<sub>2</sub> film by two step growth procedure. Unlike MoS<sub>2</sub>, in which MoS<sub>2</sub> was initially deposited, here we deposited a thin film of MoO<sub>3</sub> precursors by PLD on Si/SiO<sub>2</sub> substrate. The film thickness was precisely controlled by controlling the laser energy and laser shots. Monolayer MoSe<sub>2</sub> film was obtained by salinizing the MoO<sub>3</sub> film in CVD. The optical characterizations, including Raman, PL, XPS and second harmonic generation (SHG) revealed the excellent quality of the MoSe<sub>2</sub> film. Interestingly, the FWHM of A<sub>1g</sub> Raman characteristics peak was found to be 3.7 cm<sup>-1</sup>, which is less than that of mechanically exfoliated commercial monolayer MoSe<sub>2</sub>. This clearly indicates excellent crystal quality of MoSe<sub>2</sub> film. Moreover, the morphological characterizations including OM, FE-SEM, and



---

AFM showed the perfectly clean surface.

We further extend this approach to grow the covalently bonded sharp MoSe<sub>2</sub>-WSe<sub>2</sub> lateral HS. The MoO<sub>3</sub> and WO<sub>3</sub> were deposited on selective locations on a Si/SiO<sub>2</sub> substrate followed by the selenization process in a Se rich hot wall furnace. Monolayer MoSe<sub>2</sub>-WSe<sub>2</sub> lateral HS were formed on random locations on the substrate. Interestingly, the HS were simply identified by OM due to the different color contrast of the two constituents. The sharp interface was verified by AFM phase imaging and STEM spectroscopy. Moreover, lateral HS with gradual interface were also obtained by controlling the growth temperature profile. The gradual interface was examined by Raman and PL scanning and PL mapping.

Additionally, we were able to simultaneously polarized the four energy valleys, marked by marked by ( $K_M$ ,  $K'_M$ ) for MoSe<sub>2</sub>, and ( $K_W$ ,  $K'_W$ ) for WSe<sub>2</sub> in  $k$  space, in the sharp lateral HS system by controlling the helicity of input light. It is worth mentioning that the simultaneous valleys manipulations is not possible in lateral HS in which the cross talk effect is dominant. Lateral HS systems with well isolated energy valleys across the interface allows simultaneous valleys manipulation. This phenomenon indicates the potential use of lateral HS systems in valleytronics.

Finally, we presents initial results on the transport of exciton in WS<sub>2</sub> stripes under the effect of Berry curvature. High quality monolayer WS<sub>2</sub> flakes were grown via conventional CVD method. WS<sub>2</sub> showed excellent surface features, Raman and PL signals, thereby verifying the excellent quality of the film. Stripes of various widths were created by cutting the flake into small rectangular stripes via laser. The spatially resolved PL results showed that exciton transport within a stripe strongly depends on its width. The diffusion length was found be inversely proportional to the width of stripe. This shows that the chemical potential, which is a driving source of the electrically neutral particles, can be effectively manipulated by simply changing the geometry. Moreover, the SAPRS results confirms the accumulation of the two so called  $K$  and  $K'$  exciton on the opposite transverse side of the stripe, showing the signal of Hall Effect for exciton.

---

## Publications

- [1] Growth and Simultaneous Valleys Manipulation of Two-Dimensional MoSe<sub>2</sub>-WSe<sub>2</sub> Lateral Heterostructure, **Farman Ullah**, Yumin Sim, Chinh Tam Le, Maeng-Je Seong, Joon I. Jang,\* Sonny H. Rhim, Bien Cuong Tran Khac, Koo-Hyun Chung, Kibog Park, Yangjin Lee, Kwanpyo Kim, Hu Young Jeong and Yong Soo Kim\*, ACS Nano 11(9), 8822-8829 (2017).
- [2] Impact of Selenium Doping on Resonant Second Harmonic Generation in Monolayer MoS<sub>2</sub>, Chinh Tam Le, Daniel J. Clark, **Farman Ullah**, Velusamy Senthilkumar, Sonny. H. Rhim, Joon I. Jang\*, Yumin Sim, Maeng-Je Seong, Koo. Hyun Chung, Yong Soo Kim\*, ACS Photonics 4, 38-44 (2017).
- [3] Pulsed laser deposition assisted grown continuous monolayer MoSe<sub>2</sub>, **Farman Ullah**, Tri Khoa Nguyen, Chinh Tam Le and Yong Soo Kim\*, CrystEngComm (Crystal Engineering Communications) 18, 6992-6996 (2016).
- [4] Continuous large area few layers MoSe<sub>2</sub> films by pulse laser deposition and effect of annealing in sulfur environment, **Farman Ullah**, Velusamy Senthilkumar, S.-H. Kim, Chinh Tam Le, Huh Rock, D. -Y. Lee, S. Park, Ahmed. I. Ali, and Yong Soo Kim\*, Journal of Nanoscience and Nanotechnology (J. Nanosci. Nanotech.) 16(10), 10284-10289 (2016).
- [5] Nonlinear optical characteristic of monolayer MoSe<sub>2</sub>, Chinh Tam Le, Daniel J. Clark, **Farman Ullah**, Velusamy Senthilkuma, Joon I. Jang\*, Yumin Sim, Maeng-Je Seong, Koo-Hyun Chung, Hyoyeol Park, and Yong Soo Kim\*, Annalen der Physik (Ann. Phys.) 528(7-8), 551-559 (2016).
- [6] Near bandgap second-order nonlinear optical characteristics for MoS<sub>2</sub> monolayer transferred on transparent substrate, Daniel. J. Clark, Chinh Tam Le, Velusamy Senthilkumar, **Farman Ullah**, Heung-Yeol Cho, Yumin Sim, Maeng-Je Seong, K. -H. Chung, Y. S. Kim\*, and J. I. Jang, Applied Physics Letters (Appl. Phys. Lett.) 107, 131113-5 (2015).
- [7] Tuning optical band gap by electrochemical reduction in TiO<sub>2</sub> nanorods for improving photocatalytic activities, Jong-Won Yun, Ki Yeon Ryu, Tri Khoa Nguyen, **Farman Ullah**, Yun

- 
- Chang Park and Yong Soo Kim, RSC Adv. 7, 6202. (2017).
- [8] Platinum/palladium bimetallic ultra-thin film decorated on a one-dimensional ZnO nanorods array for use as fast response flexible hydrogen sensor, Kamrul Hassan, A.S.M. Iftekhar Uddin, **Farman Ullah**, Yong Soo Kim and Gwi-Sang Chung, Materials Letters 176 232–236 (2016).
- [9] Salt-assisted clean transfer of continuous monolayer MoS<sub>2</sub> film for hydrogen evolution reaction, Yong Soo Kim Heung-Yeol Cho, Tri Khoa, Nguyena, Farman Ullah, Jong-Won Yun, Cao Khang Nguyen, Physica b (2017)
- [10] Temperature dependence of the dielectric function of monolayer MoSe<sub>2</sub>, Han Gyeol Park, Tae Jung Kim, **Farman Ullah**, Van Long Le, Hoang Tung Nguyen, Yong Soo Kim & Young Dong Kim, Scientific Reports (2018) DOI:10.1038/s41598-018-21508-5
- [11] Ultrasonic-Assisted Spin-Coating: Improved Junction by Enhanced Permeation of a Coating Material within Nanostructures, Jong-Won Yun, **Farman Ullah**, Se-Jeong Jang, Do Hui Kim, Tri Khoa Nguyen, Ki Yeon Ryu, Shinuk Cho, Joon I. Jang, Dooyong Lee, Sungkyun Park, and Yong Soo Kim, *ACS Appl. Mater. Interfaces* (2018) DOI: 10.1021/acsami.8b04516.